

TECHNISCHE UNIVERSITÄT MÜNCHEN

DEPARTMENT CHEMIE

LEHRSTUHL FÜR BIOCHEMIE

# **Structural and functional characterization of the immunoproteasome**

Eva Maria Huber

Vollständiger Abdruck der von der Fakultät für Chemie der Technischen Universität München zur Erlangung des akademischen Grades eines Doktors der Naturwissenschaften (Dr. rer. nat.) genehmigten Dissertation.

Vorsitzender:

Univ.-Prof. Dr. L. Hintermann

Prüfer der Dissertation:

1. Univ.-Prof. Dr. M. Groll
2. apl. Prof. Dr. Dr. h.c. R. Huber (i. R.)
3. Univ.-Prof. Dr. Dr. h.c. B. Rieger

Die Dissertation wurde am 06.02.2013 bei der Technischen Universität München eingereicht und durch die Fakultät für Chemie am 27.03.2013 angenommen.



*Meiner Familie*



---

## Table of Contents

<b>1</b>	<b>Summary</b> .....	<b>8</b>
<b>2</b>	<b>Zusammenfassung</b> .....	<b>10</b>
<b>3</b>	<b>Introduction</b> .....	<b>12</b>
3.1	Intracellular protein degradation and antigen presentation .....	12
3.2	The ubiquitin-proteasome system.....	13
3.2.1	Polyubiquitylation – a signal for degradation.....	13
3.2.2	Subunit composition and architecture of proteasomes .....	14
3.2.3	Proteolysis by 20S proteasomes .....	16
3.2.4	Immune functions of 20S proteasomes .....	18
3.3	20S proteasomes: validated and emerging drug targets .....	19
3.4	Types of proteasome inhibitors .....	20
3.5	Clinically relevant proteasome inhibitors.....	21
3.6	Subunit-specific proteasome inhibitors and their therapeutic potential .....	23
<b>4</b>	<b>Objective</b> .....	<b>25</b>
<b>5</b>	<b>Materials and Methods</b> .....	<b>26</b>
5.1	Materials .....	26
5.1.1	Chemicals .....	26
5.1.2	Antibiotics .....	26
5.1.3	Media .....	26
5.1.4	Enzymes .....	27
5.1.5	Primer .....	28
5.1.6	Strains .....	29
5.1.7	Plasmids.....	29
5.1.8	Fluorogenic substrates .....	30
5.1.9	DNA and protein standards .....	31
5.1.10	Instruments .....	31
5.1.11	Computer software and bioinformatics tools .....	33
5.2	Genetic methods .....	34

5.2.1	Cultivation and long-term storage of <i>Escherichia coli</i> .....	34
5.2.2	Cultivation and long-term storage of <i>Saccharomyces cerevisiae</i> .....	34
5.2.3	Polymerase chain reaction .....	34
5.2.4	Site-directed mutagenesis .....	36
5.2.5	Agarose gel electrophoresis .....	36
5.2.6	Isolation of plasmid DNA from <i>E. coli</i> .....	37
5.2.7	Purification of DNA.....	37
5.2.8	Restriction digest of DNA.....	37
5.2.9	Determination of DNA concentration.....	38
5.2.10	Ligation of DNA fragments .....	38
5.2.11	Transformation of <i>E. coli</i> by electroporation.....	38
5.2.12	Transformation of <i>S. cerevisiae</i> .....	39
5.2.13	Plasmid shuffling .....	39
5.2.14	DNA isolation from <i>S. cerevisiae</i> .....	40
5.2.15	DNA sequencing .....	40
5.3	Protein chemistry and analytics .....	41
5.3.1	Purification of the yeast 20S proteasome.....	41
5.3.2	Purification of the murine immuno- and constitutive 20S proteasome .....	41
5.3.3	SDS polyacrylamide gel electrophoresis .....	42
5.3.4	Determination of protein concentration .....	43
5.4	Proteasome activity tests.....	43
5.4.1	Overlay assay .....	43
5.4.2	Fluorescence activity test and determination of IC <sub>50</sub> values .....	44
5.5	Protein crystallography .....	44
5.5.1	Crystallization of the yeast 20S proteasome .....	44
5.5.2	Crystallization of the murine 20S proteasomes .....	45
5.5.3	Data collection, processing and structure determination .....	45
<b>6</b>	<b>Results .....</b>	<b>47</b>
6.1	Sequence alignments.....	47
6.2	X-ray structures of the mouse 20S immuno- and constitutive proteasome .....	49
6.2.1	Crystallization and structure determination .....	49
6.2.2	Subunit architecture of the cCP and iCP.....	52
6.2.3	Structural analysis of the substrate binding channels .....	53

---

6.3	Investigations on the $\beta$ 5i-selective proteasome inhibitor ONX 0914 .....	57
6.3.1	Inhibition of 20S proteasomes by ONX 0914 .....	57
6.3.2	Proteasome core particles in complex with ONX 0914 .....	57
6.3.3	Molecular basis for the subunit selectivity of ONX 0914.....	59
6.3.4	Structural analysis of the epoxyketone reaction mechanism.....	62
6.4	Yeast mutagenesis studies on the subunits $\beta$ 5c, $\beta$ 5i and $\beta$ 5t.....	66
6.4.1	Mimicking the $\beta$ 5c active site.....	67
6.4.2	Analysis of the $\beta$ 5i substrate binding channel.....	69
6.4.3	Probing subunit $\beta$ 5t.....	73
<b>7</b>	<b>Discussion.....</b>	<b>76</b>
7.1	Structural and functional differences between the three types of CPs .....	76
7.2	Guidelines for the rational design of CP-selective inhibitors.....	78
<b>8</b>	<b>Bibliography .....</b>	<b>81</b>
<b>9</b>	<b>Appendix .....</b>	<b>90</b>
<b>10</b>	<b>Abbreviations .....</b>	<b>96</b>
<b>11</b>	<b>Publications.....</b>	<b>99</b>
<b>12</b>	<b>Acknowledgement .....</b>	<b>100</b>

# 1 Summary

20S proteasomes are destructive molecular machines that break down proteins into small peptides. Based on their task to regulate intracellular protein homeostasis and to eliminate aberrant polypeptides, proteasomes are essential for cell division and differentiation. Hence, inhibition of the main proteasome types, the constitutive proteasome and the immunoproteasome, represents a successful therapeutic strategy against cancers. Moreover, selective inhibition of the immunoproteasome, playing also a crucial role in antigen processing, is currently emerging as a medicinal rationale for autoimmune disorders and chronic inflammations. However, so far the development of selective compounds was hampered by the lack of structural data on the immunoproteasome.

The present thesis describes the structural and functional characterization of the constitutive proteasome and the immunoproteasome from mouse, which will facilitate structure-based development of novel drugs. Using X-ray crystallography, the 3D-structures of both murine proteasome types have been determined at atomic resolution and the differences between the proteolytically active subunits of the immunoproteasome ( $\beta 1i$ ,  $\beta 2i$  and  $\beta 5i$ ) and its constitutive counterpart ( $\beta 1c$ ,  $\beta 2c$  and  $\beta 5c$ ) could be revealed. As the substrate specificity pockets of the active sites differ in their size and polarity, they give rise to distinct cleavage and inhibitor preferences. In this regard the  $\beta 1i$  and  $\beta 5i$  subunits of the immunoproteasome evolved to generate antigens with hydrophobic C-terminal anchor residues that bind with high affinity to major histocompatibility class I receptors to control immune responses.

In addition, ligand complex structures of both proteasome types with the first  $\beta 5i$ -specific compound, the tripeptide  $\alpha',\beta'$ -epoxyketone ONX 0914 (PR-957) provide explanation for its subunit selectivity. While the accessibility of ONX 0914 to the active sites of  $\beta 1c$  and  $\beta 1i$  is either electrostatically or sterically hampered, the  $\beta 2c$  and  $\beta 2i$  substrate binding channels cannot provide enough stabilization for the ligand. Furthermore, binding of ONX 0914 significantly enlarges the S1 pocket of the  $\beta 5c$  active site and shifts the adjacent peptide backbone by up to 1.7 Å. In contrast, these structural changes do not occur in subunit  $\beta 5i$  of the immunoproteasome. Different side chain conformations of Met45 create a spacious S1 site in subunit  $\beta 5i$  and a significantly smaller one in  $\beta 5c$ , thereby facilitating binding of ONX 0914 to the  $\beta 5i$  active site compared to  $\beta 5c$ . In addition, the ligand complex structures disclose that the binding mechanism of peptidic compounds is identical in all proteasome subunits, including the formation of an antiparallel  $\beta$  sheet. The selectivity of peptidomimetics therefore solely depends on the interactions of the ligand's side chains with the substrate

binding channel. Time-resolved examination of the mode of action of ONX 0914 using the yeast 20S proteasome elucidated that apart from the electrophilic warhead particularly the P1 site determines the affinity of compounds for the active sites of the protease.

Sequence differences between the  $\beta 5$  subunits of the constitutive proteasome and the immunoproteasome were investigated by mutagenesis of the yeast 20S proteasome. Furthermore, the structurally uncharacterized substrate binding channel of subunit  $\beta 5t$  that assembles into the vertebrate-specific thymoproteasome was mimicked in yeast. These mutant proteasomes elucidate the impact of single amino acid exchanges on the S1 pocket architecture and the affinity of proteasome inhibitors.

The structural and functional characterization of the murine 20S proteasomes described herein now supports the development of novel selective drugs for the distinct proteasome types and their active sites, which are of considerable therapeutic potential against cancers and autoimmune diseases.

## 2 Zusammenfassung

Das 20S Proteasom ist eine molekulare Maschine, die Proteine in Peptide zerlegt. Aufgrund seiner Aufgabe das intrazelluläre Proteingleichgewicht zu kontrollieren und nicht mehr funktionsfähige Proteine zu recyceln, ist das Proteasom unabdingbar für die Zellteilung und Zelldifferenzierung. Inhibition der beiden Haupttypen des Proteasoms, des konstitutiven Proteasoms und des Immunoproteasoms, stellt deshalb eine wirksame Therapiemöglichkeit von Krebserkrankungen dar. Zudem deuten neuere Studien darauf hin, dass eine selektive Hemmung des Immunoproteasoms, das eine zentrale Rolle für die Prozessierung von Antigenen spielt, von therapeutischem Nutzen für die Behandlung von chronischen Entzündungen und Autoimmunerkrankungen sein könnte. Jedoch war bisher eine gezielte Entwicklung von selektiven Hemmstoffen aufgrund fehlender Strukturinformation über das Immunoproteasom erschwert.

Die vorliegende Arbeit beschreibt die strukturelle und funktionelle Charakterisierung des konstitutiven Proteasoms und des Immunoproteasoms der Maus und erleichtert nun die struktur-basierte Entwicklung von neuen Medikamenten. Mit Hilfe der Röntgenkristallographie konnten die atomaren Strukturen der beiden murinen Proteasomtypen bestimmt werden und die Unterschiede zwischen den proteolytisch aktiven Untereinheiten des Immunoproteasoms ( $\beta 1i$ ,  $\beta 2i$  und  $\beta 5i$ ) sowie des konstitutiven Proteasoms ( $\beta 1c$ ,  $\beta 2c$  und  $\beta 5c$ ) herausgearbeitet werden. Da sich die Substratbindetaschen der einzelnen aktiven Zentren sowohl in ihrer Größe als auch Polarität unterscheiden, ermöglichen sie verschiedene Substrat- und Inhibitorspezifitäten. Mit den  $\beta 1i$  und  $\beta 5i$  Untereinheiten ist das Immunoproteasom dafür optimiert Epitope mit apolaren C-terminalen Enden zu generieren. Diese binden mit hoher Affinität an die Haupthistokompatibilitäts-Rezeptoren der Klasse I und kontrollieren somit Immunantworten. Zudem erklären Ligandenkomplexstrukturen beider Proteasomtypen mit dem ersten  $\beta 5i$ -spezifischen Inhibitor, dem tripeptidischen  $\alpha',\beta'$ Epoxyketon ONX 0914 (PR-957), dessen Untereinheiten-Selektivität. Der Zugang von ONX 0914 zu den aktiven Zentren der  $\beta 1c$  und  $\beta 1i$  Untereinheiten ist elektrostatisch beziehungsweise sterisch behindert und in den Untereinheiten  $\beta 2c$  und  $\beta 2i$  kann der Ligand nur unzureichend stabilisiert werden. Darüber hinaus verursacht die Bindung von ONX 0914 an das aktive Zentrum der  $\beta 5c$  Untereinheit eine starke Vergrößerung der S1 Spezifitätstasche sowie eine Verschiebung des angrenzenden Peptidkettenverlaufs um bis zu 1.7 Å. Im Gegensatz dazu bewirkt ONX 0914 keinerlei Veränderungen im Substratbindekanal der  $\beta 5i$  Untereinheit des Immunoproteasoms. Unterschiedliche Seitenkettenkonformationen von

Met45 in der  $\beta 5i$  und  $\beta 5c$  Untereinheit machen die S1 Tasche der  $\beta 5i$  Untereinheit im Vergleich zu  $\beta 5c$  geräumiger, sodass die Bindung von ONX 0914 in den  $\beta 5i$  Substratbindekanal leichter als an das  $\beta 5c$  aktive Zentrum erfolgen kann. Weiterhin zeigen die Ligandenkomplexstrukturen auf, dass der Bindemechanismus des peptidischen Inhibitors für alle Proteasomuntereinheiten des Immuno- und des konstitutiven Proteasoms identisch über die Formierung eines anti-parallelen  $\beta$  Faltblattes verläuft. Somit wird die Selektivität von Peptidomimetika einzig von den Interaktionen der Liganden-Seitenketten mit dem Substratbindekanal bestimmt. Zeitaufgelöste Untersuchungen zum Reaktionsmechanismus von ONX 0914 am 20S Proteasom von *Saccharomyces cerevisiae* zeigen auf, dass abgesehen von der elektrophilen Kopfgruppe, insbesondere die P1 Seitenkette von Inhibitoren deren Affinität für die proteolytisch aktiven Zentren bestimmt.

Die Sequenzunterschiede in den Proteolysezentren der  $\beta 5$  Untereinheiten des konstitutiven Proteasoms und des Immunoproteasoms wurden mittels Mutagenese des 20S Proteasoms aus *S. cerevisiae* untersucht. Darüber hinaus wurde der Substratbindekanal der  $\beta 5t$  Untereinheit, die in das sogenannte Thymusproteasom von Vertebraten eingebaut wird und strukturell nicht charakterisierte ist, in Hefe rekonstituiert. Diese Mutanten klären die Bedeutung einzelner Aminosäureaustausche für die Architektur der S1 Taschen sowie für die Affinität von Proteasominhibitoren.

Die hier erläuterte strukturelle und funktionelle Charakterisierung der 20S Proteasome aus der Maus unterstützt die Entwicklung neuer selektiver Hemmstoffe für die einzelnen Proteasomtypen und -untereinheiten, welche gegenwärtig von hohem therapeutischen Potential für die Behandlung von Krebs- und Autoimmunerkrankungen sind.

## 3 Introduction

### 3.1 Intracellular protein degradation and antigen presentation

All proteins undergo a life cycle, starting from their synthesis at ribosomes and ending with their degradation to peptides and single amino acids. Thereby, the building blocks for the *de novo* synthesis of polypeptides are recycled and in addition important cellular functions are controlled. These include protein homeostasis, cell proliferation, signal transduction and antigen production<sup>[1]</sup>. The lysosomal and the non-lysosomal protein degradation pathways process the majority of intracellular self and nonself proteins. In lysosomes proteases termed cathepsins unselectively degrade proteins. The resulting peptide fragments can be loaded on major histocompatibility complex class (MHC) II receptors and presented on the cell surface to immune cells<sup>[2]</sup>. In contrast, hydrolysis of more than 90 % of all cytosolic proteins is carried out by the 26S proteasome – the central player of the non-lysosomal protein degradation pathway. The 26S proteasome, a multicatalytic ATP-dependent protease located in the cytosol and the nucleus, selectively cuts polyubiquitylated proteins to peptides of diverse lengths<sup>[3]</sup>. While most of these peptides are further decomposed to single amino acids, a fraction escapes this fate and serves as antigens for the immune system in vertebrates. Prior or after N-terminal trimming to 8-11 amino acids by aminopeptidases<sup>[4]</sup> putative epitopes transit into the endoplasmic reticulum (ER) by the transporter associated with antigen processing (TAP), a member of the ATP-binding cassette transporter family<sup>[5]</sup>. In the ER peptides can associate with the binding cleft of nascent MHC I receptors. The peptide's affinity for the MHC I complex largely depends on its C-terminal anchor residue<sup>[6]</sup>, which is determined by the cleavage specificities of the proteasome. Only stable receptor:ligand complexes adopt a mature structure and are transported in vesicles to the cell membrane for their exposure to the extracellular environment. Surveying effector cells of the immune system scan the peptide cargos of both MHC I and II receptor proteins for their origin and cells that carry bacterial or viral peptides on their cell surface are identified and eliminated by cytotoxic T lymphocytes to prevent an infection<sup>[7]</sup>. Hence, by shaping the antigenic pool of peptides the proteasome constitutes a key component of the adaptive immune system of vertebrates.

## 3.2 The ubiquitin-proteasome system

### 3.2.1 Polyubiquitylation – a signal for degradation

Posttranslational modifications such as ubiquitylation control the subcellular localization, signal transduction, enzymatic activity and stability of eukaryotic proteins. Ubiquitin itself is a highly conserved polypeptide of 8.5 kDa and 76 amino acids and its covalent linkage to proteins is catalysed by the sequential action of three classes of enzymes, termed ubiquitin-activating enzyme (E1), ubiquitin-conjugating enzyme (E2) and ubiquitin ligase (E3)<sup>[3b]</sup>. The E1 enzyme activates the C-terminal glycine residue of ubiquitin in an ATP-dependent manner under the release of pyrophosphate. Subsequent attachment of the adenylated ubiquitin to the active site Cys residue of the E1 enzyme yields a thioester and an AMP molecule. Next, ubiquitin is conjugated to the catalytic Cys of an ubiquitin-conjugating enzyme (E2) and finally, an E3 ligase creates an isopeptide bond between the ubiquitin's C-terminus and the  $\epsilon$ -amino group of a lysine side chain in the substrate protein (Figure 1)<sup>[3b]</sup>. Selectivity of the ubiquitylation reaction is ensured by a myriad of E3 ligases that binds to recognition sites in their target proteins either directly or via adaptor proteins. Commonly, proteins that carry a chain of at least four ubiquitin molecules connected via Lys48 are targeted for degradation by the 26S proteasome<sup>[8]</sup>.

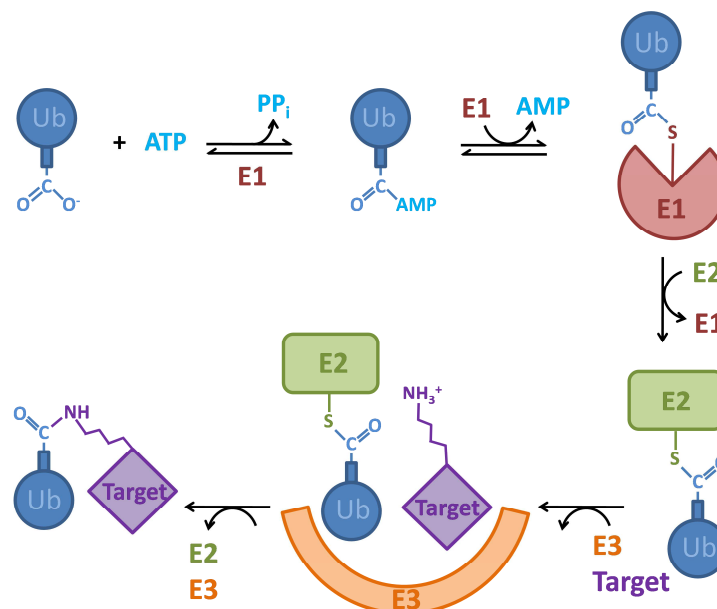


**Figure 1 Ubiquitin activation and linkage to substrate proteins.** Adenylation of ubiquitin by an E1 enzyme is followed by its transfer to an E2 ubiquitin-conjugating enzyme. An E3 ligase covalently attaches ubiquitin to a lysine residue in the target protein.

Adapted from Berg and Stryer, 2002<sup>[9]</sup>.

### 3.2.2 Subunit composition and architecture of proteasomes

The 26S proteasome is a molecular machine of approximately 2.5 MDa, consisting of a cylindrical 20S core particle (CP) and two 19S regulatory complexes associated on both ends. The 19S cap binds polyubiquitylated substrates, cleaves off their ubiquitin molecules, unfolds and finally translocates client proteins into the proteolytic 20S chamber<sup>[10]</sup>. In contrast to the 19S complex whose atomic structure has not yet been resolved, the core of the proteasome has been extensively characterized at the molecular level, leading to the following current understanding of its evolution and functioning.

The barrel-shaped CP is present in all three kingdoms of life, bacteria, archaea and eukaryotes. Bacteria except for actinomycetes harbour CP-like complexes termed heat-shock locus (Hsl) V that consist of two homohexameric rings of a proteolytically active subunit<sup>[11]</sup>. The CP of actinomycetes, archaea and eukaryotes adopts a more complex quaternary structure. The X-ray structures of the CP from the archaeon *Thermoplasma acidophilum*<sup>[12]</sup> and the eukaryote *S. cerevisiae*<sup>[13]</sup> proved that the protease is a cylinder of 148 Å in length and 113 Å in width with a molecular mass of approximately 720 kDa and that it consists of two different types of subunits termed  $\alpha$  and  $\beta$ . Both monomers are assembled in four homoheptameric rings that are stacked in an  $\alpha\beta\beta\alpha$  stoichiometry around a central pore. Due to its two-fold rotational symmetry the CP comprises two identical halves (Figure 2)<sup>[12-13]</sup>. Archaeal 20S proteasomes incorporate only one type of  $\alpha$  and one type of  $\beta$  subunit<sup>[12]</sup>. By contrast, eukaryotic proteasomes contain seven different  $\alpha$  (1-7) and seven different  $\beta$  (1-7) subunits (Figure 2)<sup>[13]</sup>, which occupy unique positions within the CP. All known  $\alpha$  and  $\beta$  subunits share the same tertiary structure of two antiparallel five-stranded  $\beta$  sheets being flanked by  $\alpha$  helices and probably evolved from a common ancestor (Figure 2A)<sup>[12, 14]</sup>.

Several functions have been attributed to the  $\alpha$  subunits. Their intrinsic ability to form a heptameric ring is pivotal for the assembly of the  $\beta$  subunits and the formation of the CP. Furthermore, so-called shuttling sequences in the  $\alpha$  subunits enable the import of the CP into the nucleus and its re-export<sup>[15]</sup>. The  $\alpha$  subunits also form the entry gate to the interior of the CP<sup>[16]</sup>. In particular, the N-terminal extensions of the subunits  $\alpha 2$ ,  $\alpha 3$  and  $\alpha 4$  close the barrel-shaped CP on both ends and thereby abolish uncontrolled degradation of intracellular proteins<sup>[12-13]</sup>. Docking of regulatory and adapter complexes such as the 11S (PA28), 19S and PA200 (BIm10) particles onto the  $\alpha$  ring rearranges the N-termini of the  $\alpha$  subunits and enables access to the proteolytically active sites that are sequestered in the  $\beta$  rings<sup>[17]</sup>. The  $\beta$  subunits are synthesized as inactive precursor proteins with N-terminal propeptides of up to 75 amino acids. These propeptides are involved in CP assembly assisted by the proteasome

maturation factor Ump1 (ubiquitin-mediated proteolysis 1)<sup>[18]</sup> and protect the catalytic active sites from inactivating N $\alpha$  acetylation prior to proteasome maturation<sup>[19]</sup>. In the final step of proteasome assembly the propeptides are removed by intramolecular autolysis, thereby exposing the proteolytically active Thr1 residues and yielding a proteasome particle that can cut polypeptides down to size<sup>[12, 20]</sup>. Remarkably, in eukaryotes only three out of the seven different  $\beta$  subunits, namely  $\beta$ 1,  $\beta$ 2 and  $\beta$ 5, are proteolytically active as N-terminal nucleophile (Ntn) threonine hydrolases<sup>[13]</sup>.

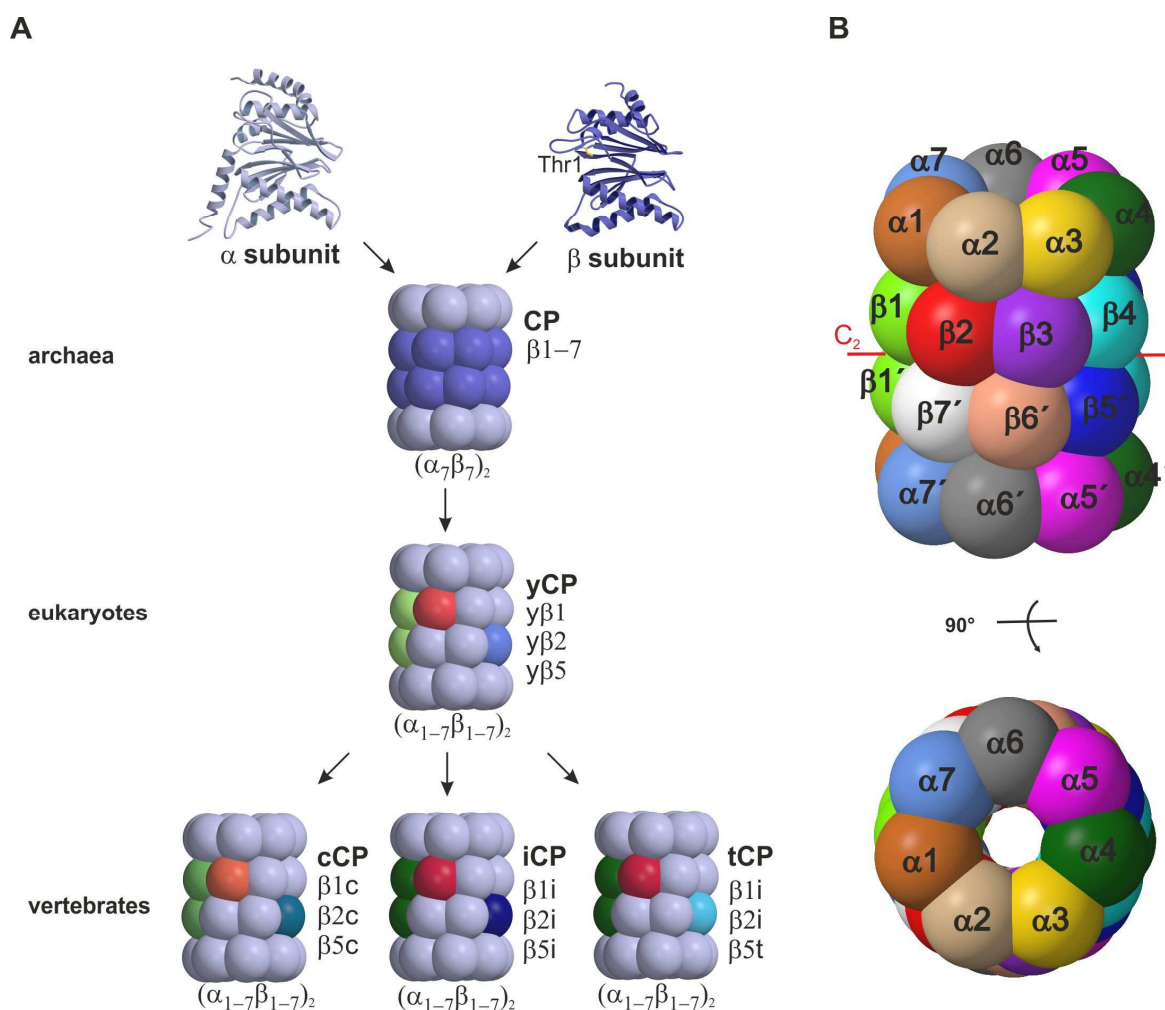


**Figure 2 Evolution of 20S proteasomes.** (A) Archaeal CPs are assembled of two different types of monomers, namely inactive  $\alpha$  (grey) and proteolytically active  $\beta$  subunits (blue). Both presumably originated from a common but unknown precursor protein<sup>[14]</sup>. Eukaryotes such as *S. cerevisiae* encode seven different  $\alpha$  and seven different  $\beta$  subunits, but only the  $\beta$  subunits  $\beta$ 1 (green),  $\beta$ 2 (red) and  $\beta$ 5 (blue) are enzymatically active<sup>[13]</sup>. Their inactive  $\alpha$  and  $\beta$  subunits are coloured in grey. In vertebrates three classes of 20S proteasomes evolved. The constitutive proteasome (cCP), the immunoproteasome (iCP) and the thymoproteasome (tCP) have distinct sets of catalytic  $\beta$  subunits and thus, are implemented in different biological pathways<sup>[13, 21]</sup>. (B) Side and top view of the eukaryotic CP. The  $C_2$  symmetry of the proteasome particle is indicated as a red rod. Adapted from Huber *et al.*, 2012<sup>[22]</sup>.

Whereas primitive eukaryotes like baker's yeast bear only one type of CP<sup>[13]</sup>, vertebrates express three classes of CPs<sup>[21c, 23]</sup>: the constitutive proteasome (cCP), the immunoproteasome (iCP) and the thymoproteasome (tCP). The cCP comprises the catalytic active constitutive (c) subunits  $\beta$ 1c (Y, *PSMB6*),  $\beta$ 2c (Z, *PSMB7*) and  $\beta$ 5c (X, *PSMB5*) and represents the prevailing proteasome species in cells of non-haematopoietic origin. In contrast, in immune cells such as lymphocytes and monocytes the iCP is predominant<sup>[23]</sup> (Figure 2A). Nonetheless, expression of the iCP can also be induced in non-immune tissues by proinflammatory cytokines such as interferon (IFN)- $\gamma$  and tumour necrosis factor (TNF)- $\alpha$ <sup>[21b, 24]</sup>. As the three proteolytically active immuno (i) subunits  $\beta$ 1i (LMP2, low molecular weight protein 2, *PSMB9*),  $\beta$ 2i (MECL1, multicatalytic endopeptidase complex-like-1, *PSMB10*) and  $\beta$ 5i (LMP7, *PSMB8*) are preferentially assembled into CPs, mainly iCPs are formed *de novo* upon cytokine release<sup>[21b, 25]</sup>. Apart from the i subunits IFN- $\gamma$  also triggers the expression of the 11S adaptor complex PA28 $\alpha\beta$ <sup>[26]</sup>. This particle stimulates proteasome activity and is essential for the generation of certain antigenic peptides<sup>[27]</sup>. Furthermore, PA28 $\alpha\beta$  has been suggested to target iCPs to the TAP in the ER membrane in order to directly translocate the generated peptides into the ER lumen<sup>[28]</sup>. Besides the cCP and iCP, mixed proteasomes bearing the subunit composition  $\beta$ 1c,  $\beta$ 2c and  $\beta$ 5i or  $\beta$ 1c,  $\beta$ 2i and  $\beta$ 5i were reported to account for 30-50 % of all cellular CPs<sup>[29]</sup> and even CPs with asymmetric composition of  $\beta$  subunits were described<sup>[30]</sup>. The third type of CP, the vertebrate-specific thymoproteasome (tCP), is exclusively expressed in cortical thymic epithelial cells (cTECs) and incorporates the i subunits  $\beta$ 1i and  $\beta$ 2i as well as the exceptional subunit  $\beta$ 5t (*PSMB11*)<sup>[21c]</sup> (Figure 2A). The unique expression profile and subunit composition of the tCP has been implicated to play a pivotal role for the development of CD8<sup>+</sup> cytotoxic T cells as part of the adaptive immune system.

### 3.2.3 Proteolysis by 20S proteasomes

Structural studies along with mutagenesis experiments proved that a sophisticated hydrogen bond network involving the amino acids Thr1, Asp17, Lys33, Ser129, Asp166 and Ser169 is responsible for the nucleophilicity of the  $\gamma$ -hydroxylgroup of the active site Thr1 and thus, for proteolytic activity<sup>[12-13]</sup>. A nucleophilic water molecule cluster in the active site induces the proton transfer from Thr1O <sup>$\gamma$</sup>  to Thr1N, which functions as proton acceptor. Peptide bond hydrolysis then starts with an attack of the N-terminal Thr1O <sup>$\gamma$</sup>  onto the electrophilic carbonyl carbon atom of the scissile peptide bond of substrate proteins (Figure 3). This reaction step creates an acyl-enzyme intermediate and frees the N-terminus of the C-terminal peptide

fragment. Addition of a pre-oriented nucleophilic water molecule restores the catalytic Thr1 and deliberates the C-terminus of the second cleavage product (Figure 3)<sup>[31]</sup>.

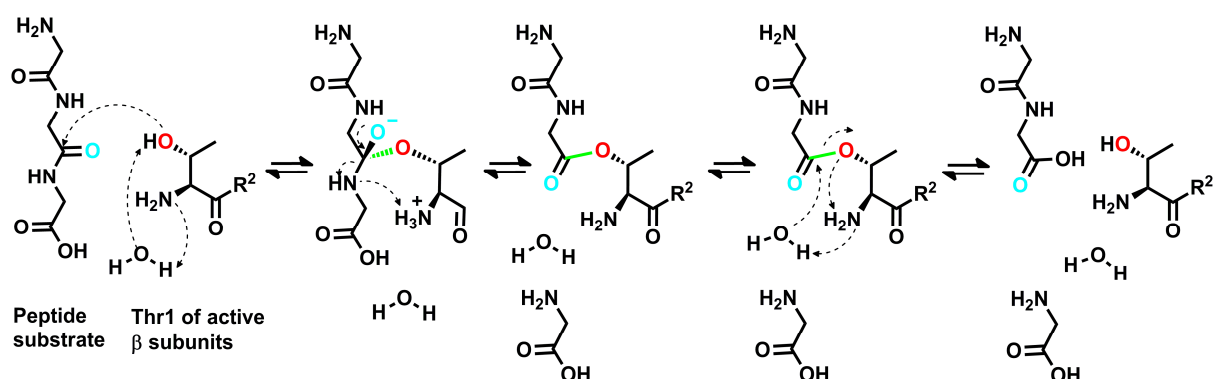


**Figure 3 Peptide bond hydrolysis by the proteasome.** The nucleophilic Thr1O<sup>γ</sup> (red) attacks the electrophilic carbonyl carbon atom of the peptide bond thereby releasing the first cleavage product. In a second step hydrolysis of the formed acyl-enzyme complex (green bond) frees the N-terminal cleavage product and restores the catalytic Thr1.

The proteasome is classified as an endoprotease, as it harbours primed (S1', S2', S3') and unprimed substrate binding pockets (S1, S2, S3) that are formed by two adjacent subunits<sup>[12]</sup>. The chemical nature of these sites, which accommodate the side chains (P residues) of client proteins (Figure 4), determines the mean residence time of ligands and thus, the cleavage preferences.

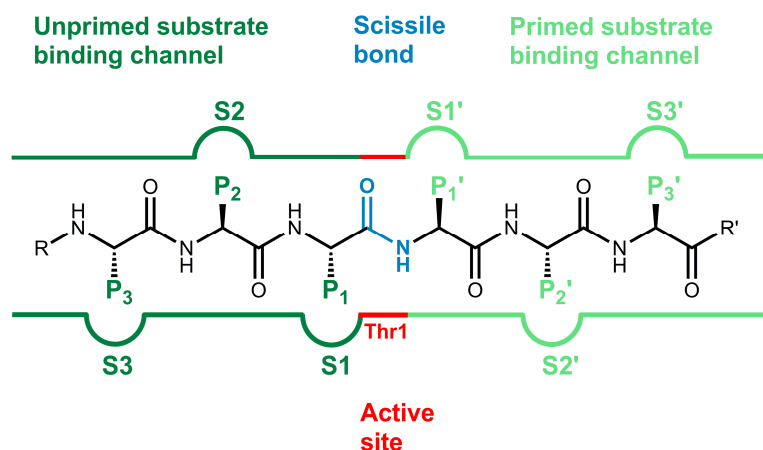


**Figure 4 Schematic representation of the substrate binding channel of the proteasomal active sites.** The primed pockets (S'; green) and unprimed specificity sites (S; dark green) bind the ligand's side chains (P' and P sites). Afterwards the active site Thr1 (red) cleaves the scissile peptide bond (blue). Adapted from Huber *et al.*, 2012<sup>[22, 32]</sup>.

In particular the chemical properties of amino acid 45, forming the bottom of the S1 pocket, decide on proteasomal substrate specificities. The positively charged Arg45 of subunit  $\beta$ 1/ $\beta$ 1c favours a caspase-like (CL) activity by accommodating acidic residues in the S1 pocket. However, subunit  $\beta$ 1 can also cleave after some hydrophobic amino acids and thereby

contributes to the branched chain amino acid preferring (Braap) activity of the proteasome<sup>[33]</sup>. Even though a trypsin-like (TL) activity has been attributed to subunit  $\gamma\beta 2/\beta 2c$ , it can virtually process after all kind of residues owing to Gly45. The chymotrypsin-like (ChTL) activity, residing in subunit  $\gamma\beta 5/\beta 5c$ , preferentially hydrolyses proteins C-terminally of hydrophobic amino acids, because its substrate binding channel is lined with apolar residues such as Met45<sup>[13, 33b]</sup>. In addition, a so-called small neutral amino acid preferring activity (Snaap) has been assigned to the proteasome. For the iCP, previous studies suggested a reduced CL activity, but an enhanced ChTL activity as compared with the cCP/yCP<sup>[13, 33a, 34]</sup>. In contrast, the vertebrate-specific tCP has been demonstrated to exert only minimal ChTL activity<sup>[21c]</sup>.

### 3.2.4 Immune functions of 20S proteasomes

CPs shape the pool of antigenic peptides that are presented by MHC I receptors on the cell surface to immune cells. Importantly, all three types of CPs, the cCP, iCP and tCP, are capable of generating antigens<sup>[35]</sup>. However, their distinct substrate specificities result in different epitope repertoires and physiological implications. Although certain cCP-dependent peptides can trigger immune reactions, the iCP is particularly decisive for this process. Cytokines released during viral infections induce the expression of the iCP in order to enhance antigen presentation and to support clearance of the pathogen. In agreement, mice lacking the iCP bear a significantly altered repertoire of antigens in terms of quantity and quality, implicating that the i subunits enlarge both the abundance and the diversity of MHC I epitopes<sup>[36]</sup>. Besides, the iCP plays a crucial role in T cell differentiation and the release of proinflammatory cytokines such as interleukin (IL)-23, IL-2 and IFN- $\gamma$  via a yet unknown nuclear factor- $\kappa$ B (NF- $\kappa$ B)-independent pathway<sup>[37]</sup>. In addition, proteins that are damaged by cytokine-induced oxidative stress were shown to be efficiently cleared by the iCP<sup>[38]</sup>.

In contrast to the cCP, the expression of the tCP is restricted to the cTECs of the thymus<sup>[35b]</sup>. This specialized organ of the immune system selects T lymphocytes for the optimal interaction strength of their T cell receptor (TCR) with MHC:self-peptide complexes. Immature thymocytes whose TCR tightly binds to MHC receptors loaded with self-antigens are auto-reactive and are eliminated by negative selection, while T cells with weak TCR:MHC interactions are considered as self-tolerant and thus survive (positive selection)<sup>[23, 39]</sup>. The markedly attenuated ChTL activity of the tCP-specific subunit  $\beta 5t$  is assumed to produce low-affinity self-epitopes for the presentation on MHC receptors<sup>[35b]</sup>. Moreover, the

peptide pool created by tCPs in cTECs is unique throughout the body and thus, might prevent autoimmunity, as positively selected T cells more seldom cross-react with self-peptides that have been generated by the cCP and iCP outside the cTECs<sup>[40]</sup>. Remarkably, in  $\beta 5t$ -depleted mice the number of CTLs is reduced by 75 %, stressing the importance of the tCP for the maturation of thymocytes<sup>[21c]</sup>. In conclusion, the tCP helps to establish a tolerant T cell repertoire, the prerequisite for a functional adaptive immune system and the iCP promotes immune surveillance and the elimination of pathogens. Hence, both the tCP and the iCP are key players of the adaptive immune system in vertebrates and their malfunctioning positively correlates with the onset of diverse diseases.

### 3.3 20S proteasomes: validated and emerging drug targets

20S proteasomes primarily serve to degrade regulatory or aberrant proteins, but during evolution this function has been exploited for the development of the vertebrate immune system. Thus, the multifaceted functions of CPs make them attractive drug targets for diseases as diverse as cancers and autoimmune disorders.

The CP levels of tumour cells are often upregulated, because their accelerated cell cycle and metabolism require increased turnover rates of proteins. This dependence on CP activity renders neoplastic cells highly susceptible to proteasome inhibition. Among cancers multiple myeloma cells are most sensitive to CP inhibitors<sup>[41]</sup>. Myeloma cells are derived from plasma cells and their excessive synthesis of immunoglobulins as well as their chromosomal instability leads to many aberrant and misfolded proteins that have to be removed by CPs. Hence, inhibition of the CP causes the accumulation of protein aggregates and finally triggers ER stress as well as the unfolded protein response<sup>[42]</sup>. Furthermore, CP inhibitors block proinflammatory signalling cascades such as NF- $\kappa$ B and the expression of anti-apoptotic target genes<sup>[41b]</sup>. Ultimately, tumour suppressor genes like the cyclin kinase inhibitor p27<sup>kip1</sup><sup>[43]</sup> induce apoptosis in transformed cells, while healthy cells remain unaffected<sup>[41a]</sup>. This difference in susceptibility creates a therapeutic window for proteasome inhibition in haematological cancers.

However, in certain malignancies, including lung, colon and prostate cancers as well as feline primary fibrosarcoma, tumour pathogenesis depends on elevated iCP and cytokine levels<sup>[44]</sup>. Additionally, Alzheimer's<sup>[45]</sup> and Huntington's<sup>[46]</sup> disease as well as amyotrophic lateral sclerosis<sup>[47]</sup> and inflammatory bowel disease<sup>[48]</sup> are characterized by increased expression rates of iCPs or single i subunits. Moreover, abnormal levels of i subunits were observed in

Sjogren's syndrome<sup>[49]</sup>, inclusion body myositis, myofibrillar myopathy<sup>[50]</sup>, Crohn's disease<sup>[51]</sup> and dextran sulfate sodium-induced colitis<sup>[52]</sup>. These findings suggest a therapeutic benefit from blocking solely the iCP, at least for the above mentioned diseases. So far, inhibition of the iCP has proven its effectiveness in a number of autoimmune disorders<sup>[37, 53]</sup>, but ambiguous results were obtained with respect to its anti-cancer activity. Although a few malignancies were reported to be sensitive to inhibition of the iCP<sup>[44b, 54]</sup>, other studies demonstrate that only simultaneous blockage of several active sites, for instance of  $\beta$ 5c and  $\beta$ 5i, efficiently causes cell death<sup>[55]</sup>.

In contrast to the cCP and iCP, the therapeutic potential of tCP blockage has not been investigated up to now.

### 3.4 Types of proteasome inhibitors

Drug discovery in the ubiquitin-proteasome system has been considerably facilitated by the crystallographic analysis of the CP from *T. acidophilum*<sup>[12]</sup>, *S. cerevisiae*<sup>[13]</sup> and *Bos taurus*<sup>[21a]</sup>. Most of the proteasome inhibitors known today harbour an electrophilic head group that reversibly or irreversibly inhibits the catalytic Thr1O <sup>$\gamma$</sup> . According to their type of pharmacophore covalently acting compounds can be subdivided into seven classes (Figure 5): aldehydes, vinyl sulfones, vinyl amides (syrbactins), boronic acids,  $\alpha'$ , $\beta'$ epoxyketones,  $\alpha$  ketoaldehydes (glyoxals) and  $\beta$  lactones. Aldehydes, such as the calpain inhibitors I (Ac-Leu-Leu-norleucinal) and II (Ac-Leu-Leu-methional) were the first inhibitors identified for the proteasome<sup>[12, 56]</sup>. However, their susceptibility to oxidation and their off-target activity towards serine and cysteine proteases restrict their medical potential. Vinyl sulfones<sup>[57]</sup> and the naturally occurring syrbactins<sup>[58]</sup> form an ether bond with Thr1O <sup>$\gamma$</sup>  in a Michael-type 1,4-addition, but also target cysteine proteases. Furthermore,  $\beta$  lactones are, depending on their R<sup>1</sup> substituent, either reversible or irreversible inhibitors of the CP<sup>[59]</sup> and its most prominent representative marizomib (salinosporamide A; NPI-0052; Nereus Pharmaceuticals, Inc.) is currently in clinical phase I trials for myeloma, lymphoma and leukaemia<sup>[60]</sup>. Despite their high reactivity and the associated adverse effects, boronic acids such as bortezomib are among the most potent inhibitors of the CP (see also section 3.5). The recently developed second-generation drugs for the proteasome are  $\alpha'$ , $\beta'$ epoxyketone-based compounds. Their pharmacophore is derived from the natural product epoxomicin that irreversibly inhibits the CP in a bivalent reaction involving both Thr1O <sup>$\gamma$</sup>  and Thr1N (see 6.3.4)<sup>[61]</sup>. Due to this mode of action  $\alpha'$ , $\beta'$ epoxyketones are highly selective for Ntn hydrolases such as the 20S proteasome.

Employing a reaction mechanism similar to  $\alpha',\beta'$ -epoxyketones,  $\alpha$  ketoaldehydes also selectively target CPs but their formation of a cyclic Schiffbase with Thr1O $^{\gamma}$  and Thr1N is reversible<sup>[62]</sup>.

Except for lactones and syrbactins, CP ligands consist of a peptidic backbone of two to four amino acids that is attached to one of the listed electrophilic head groups. These peptide-based compounds were shown to mimic natural protein substrates by forming an antiparallel  $\beta$  sheet in the substrate binding channels of the  $\gamma$ CP<sup>[63]</sup>.

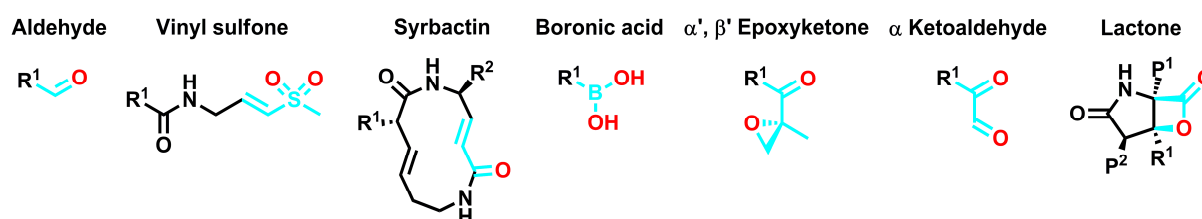


**Figure 5 Electrophilic headgroups of covalently acting proteasome inhibitors.** The functional groups are shown in cyan with their oxygens marked in red. R<sup>1</sup> and R<sup>2</sup> designate the variable parts of the compounds. For lactones the P<sup>1</sup> and P<sup>2</sup> side chains, targeting the corresponding S pockets of CPs, are depicted.

### 3.5 Clinically relevant proteasome inhibitors

After years of academic and pharmaceutical research, in 2003, bortezomib (Velcade<sup>®</sup>, Millenium Pharmaceuticals, Inc.; PS-341) has been granted full approval by the U. S. food and drug administration (FDA) for the treatment of multiple myeloma as well as relapsed or refractory mantle cell lymphoma (Figure 6)<sup>[64]</sup>. Furthermore, the therapeutic benefit of bortezomib for organ transplantation<sup>[65]</sup> and solid tumours like non-small cell lung cancer<sup>[66]</sup> is currently being investigated. With annual sale rates of more than 2 billion dollars bortezomib is a blockbuster drug that substantially elongates the life spans and survival rates of multiple myeloma patients. The dipeptide boronic acid inhibitor potently inhibits the  $\beta$ 5c,  $\beta$ 5i and  $\beta$ 1i active sites of the cCP and iCP with IC<sub>50</sub> values of 3-8 nM and only in higher concentrations also targets the  $\beta$ 1c,  $\beta$ 2c and  $\beta$ 2i subunits<sup>[42e]</sup>. Boronic acids such as bortezomib form a reversible tetrahedral transition state with Thr1O $^{\gamma}$  that is stabilized by hydrogen bonds with Thr1N and the oxyanion hole Gly47NH of active proteasome subunits<sup>[67]</sup>. Although these interactions promote a higher affinity of bortezomib for Ntn hydrolases, bortezomib was shown to also considerably inhibit serine proteases, including cathepsin G, cathepsin A, chymase, dipeptidyl peptidase II and HtrA2/omi, involved in neuronal survival<sup>[68]</sup>. These off-target activities cause severe neurotoxicity leading to tremor, reduced nerve conduction velocity and nerve degeneration, which affect about 30 % of all

patients treated with bortezomib<sup>[68]</sup>. Additional drawbacks of bortezomib include thrombocytopenia, neutropenia and gastrointestinal disorders as well as its poor bioavailability that necessitates intravenous administration<sup>[69]</sup>.

Moreover, a significant fraction of newly diagnosed patients does not respond to bortezomib and treated patients often relapse<sup>[70]</sup>. Whereas increased concentrations of the heat shock protein (Hsp) 27 were reported to confer primary resistance<sup>[71]</sup>, the molecular basis for acquired non-responsiveness to bortezomib is still in focus of scientific research efforts. So far, cell culture studies analysing the long-term effects of bortezomib treatment revealed several adaptive mutations in the  $\beta 5$  substrate binding channel that convey drug resistance. For instance, the mutations M45V, M45I, A49T, A49V, A50V, C52F and C63F are suggested to impair both the catalytic activity of subunit  $\beta 5$  and its affinity for bortezomib, hereby leading to the observed reduction in therapeutic efficacy<sup>[72]</sup>. These findings might also provide an explanation for the up-regulation of subunit  $\beta 5$  as a compensation for its decreased activity<sup>[72a]</sup>. However, evidence for the clinical relevance of these *in vitro* identified mutations and their biological impact still has to be adduced. Despite its overwhelming success in the first decade of its application, bortezomib's disadvantages encouraged the development of a second generation of CP inhibitors.

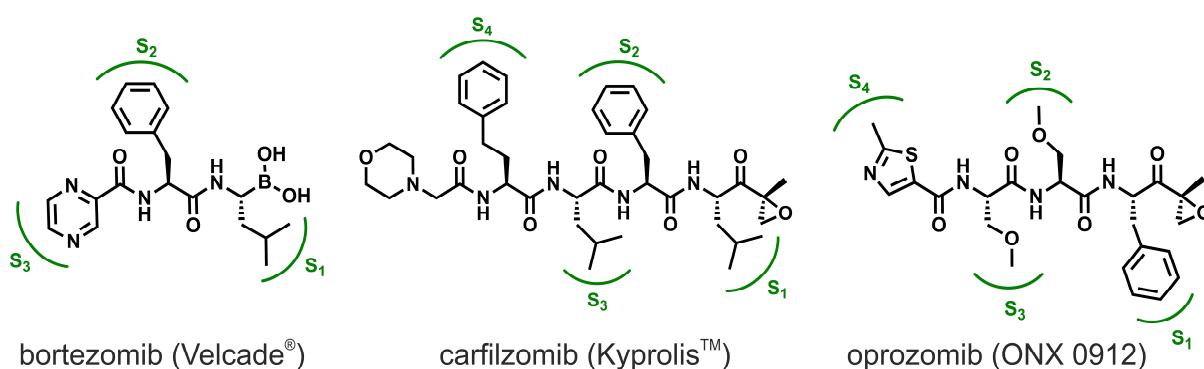


**Figure 6 Prominent proteasome inhibitors.** The chemical structures of the dipeptide boronic acid inhibitor bortezomib, the tetrapeptidic  $\alpha',\beta'$ -epoxyketone carfilzomib and the tripeptide oprozomib are shown. All three compounds target the  $\beta 5c$  and  $\beta 5i$  active sites of the proteasome. Bortezomib and carfilzomib are FDA approved for the treatment of multiple myeloma; oprozomib is in phase I clinical trials. The unprimed substrate specificity (S) pockets of the CP that are targeted by these compounds are indicated in green.

Just recently, in July 2012, one of these novel compounds, carfilzomib (Kyprolis®; Onyx Pharmaceuticals, Inc.; PR-171) has been approved by the FDA as a second-line drug for the treatment of patients that relapsed from bortezomib (Figure 6)<sup>[73]</sup>. Carfilzomib belongs to the class of  $\alpha',\beta'$ -epoxyketones derived from the microbial natural product epoxomicin. To date, due to their bivalent irreversible reaction mode,  $\alpha',\beta'$ -epoxyketones are the most specific

inhibitors known for the CP<sup>[61]</sup> (see 6.3.4). Similarly to bortezomib, carfilzomib potently blocks the  $\beta$ 5c and  $\beta$ 5i active sites of cCP and iCP with IC<sub>50</sub> values of 6 nM and 33 nM, respectively, but unlike bortezomib, carfilzomib does not affect  $\beta$ 1c<sup>[74]</sup>. Although carfilzomib also unintentionally induces neutropenia and thrombocytopenia, it does not cause peripheral neurotoxicity, as observed for the boronic acid bortezomib<sup>[68, 75]</sup>.

Oprozomib (Onyx Pharmaceuticals, Inc.; ONX 0912; PR-047), another epoxomicin derivative, is an orally available inhibitor of both the  $\beta$ 5c and the  $\beta$ 5i active sites (IC<sub>50</sub> ( $\beta$ 5c) 36 nM; IC<sub>50</sub> ( $\beta$ 5i) 82 nM)<sup>[76]</sup>. Owing to its high cytotoxicity and its superiority to bortezomib and carfilzomib with respect to its mode of administration, oprozomib is currently being explored in Phase I clinical trials as a monotherapy for solid tumours and haematological malignancies.

### 3.6 Subunit-specific proteasome inhibitors and their therapeutic potential

Subunit-specific inhibitory compounds are valuable tools for examining the impact of individual proteasome subunits on cell division and biological signalling pathways. However, the development of compounds with subunit specificities is often hindered by the strong inhibitory potency of most reactive functional head groups (see chapter 3.4). Hence, only ligands that undergo optimal enthalpic interactions with the surrounding protein residues exert pronounced subunit selectivity and for their design structural data are strongly demanded.

A long time drug design efforts solely concentrated on the ChTL activities of the proteasome, but current studies also take into account the CL and TL active sites. Recently, a series of  $\alpha'$ , $\beta'$  epoxyketone inhibitors that target the TL activities of the cCP and iCP was published<sup>[77]</sup>. These compounds were demonstrated to render malignant cells more susceptible to bortezomib and carfilzomib than  $\beta$ 1-selective inhibitors<sup>[77]</sup>. Nonetheless, compounds with selectivity for either  $\beta$ 2c or  $\beta$ 2i are still not available. For subunit  $\beta$ 1i two selective drugs have been reported so far: UK-101, a dihydroeponemycin based  $\alpha'$ , $\beta'$  epoxyketone and IPSI-001 (calpeptin), a peptide aldehyde inhibitor. The cytotoxicity of UK-101 towards  $\beta$ 1i overexpressing prostate cancer cells<sup>[44b]</sup> underlines the importance of the iCP for the onset and progression of at least certain malignancies. Likewise, anti-tumour activity has been described for IPSI-001<sup>[54a]</sup>, however, its apoptotic effects might result from co-inhibition of  $\beta$ 5 active sites. For the  $\beta$ 5 subunits several highly potent and selective ligands are known. The most potent compound is the  $\beta$ 5i-targeting  $\alpha'$ , $\beta'$  epoxyketone ONX 0914 (PR-957; OnyxPharmaceuticals, Inc.; Figure 7)<sup>[37]</sup>. Remarkably, ONX 0914 showed therapeutic effects

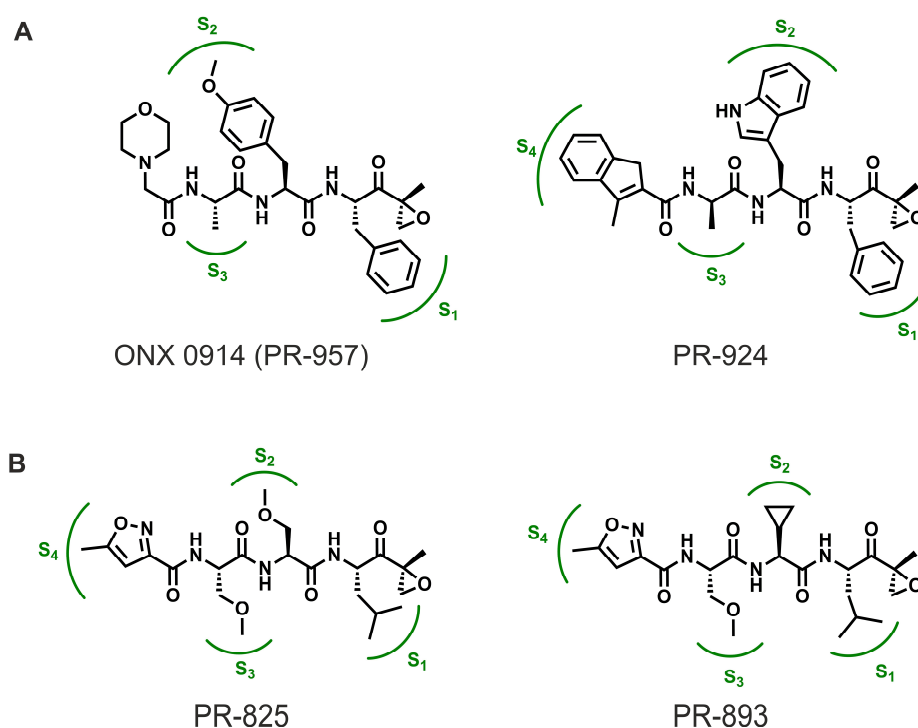


**Figure 7 Chemical structures of  $\beta 5i$ - and  $\beta 5c$ -selective compounds.** (A) ONX 0914 and PR-924 specifically target subunit  $\beta 5i$  of the iCP. (B) PR-825 and PR-893 are selective inhibitors of the  $\beta 5c$  active site of the cCP. The unprimed substrate specificity pockets of the proteasome that accommodate the side chains of the peptidic inhibitors are indicated in green.

in mouse models of rheumatoid arthritis<sup>[37]</sup>, experimental colitis<sup>[53a]</sup>, lupus erythematosus<sup>[53b]</sup> and Hashimoto's thyroiditis<sup>[53c]</sup>. These medicinal benefits are based on the reduction of the levels of proinflammatory cytokines such as IL-6, IL-23 and TNF<sup>[37]</sup> and the modulation of CTL responses. More specifically, ONX 0914 harms the differentiation and proliferation of T<sub>H1</sub> and T<sub>H17</sub> cells but not of regulatory T lymphocytes<sup>[78]</sup>. In addition, administration of ONX 0914 depresses the expression of MHC I receptors to 50 % and abolishes the production of  $\beta 5i$ -restricted antigens. Compared to etanercept, a scavenger of the proinflammatory cytokine TNF- $\alpha$  currently used as an immunosuppressant, ONX 0914 exerts higher potency<sup>[37]</sup>. Based on its promising pharmacological properties and effects in model systems, ONX 0914 is further investigated in preclinical studies for autoimmune diseases. The medicinal potential of the second  $\beta 5i$ -selective compound PR-924 (Onyx Pharmaceuticals, Inc.), a structural analogue of ONX 0914, has not yet been evaluated in immunological disorders, but conflicting data have been described with respect to its anti-myeloma activity<sup>[54b, 55]</sup>. Notably, the two epoxomicin derivatives PR-825 and PR-893 (Onyx Pharmaceuticals, Inc.), that selectively target subunit  $\beta 5c$ , were attributed neither anti-inflammatory nor anti-cancer activity<sup>[37, 55]</sup>. Hence, cCP and tCP selective drugs remain to be examined for any medicinal use.

## 4 Objective

Structural information on the yCP alone and in complex with ligands strongly supported the development of the currently known potent CP inhibitors bortezomib and carfilzomib. Both compounds do not discriminate between the three mammalian CP types and, thereby, exert anti-cancer activity. However, recent studies demonstrate that iCP-specific inhibitors might qualify as therapeutics in autoimmune diseases. So far, only a few iCP-specific inhibitors were identified, mostly because structural data on the iCP were lacking.

The aim of this thesis was to elucidate the atomic structures of the murine iCP and cCP by X-ray crystallography. The crystal structures of both CP types from one organism enable the direct comparison of the structural features of the iCP and the cCP from *Mus musculus*, the cCP from *B. taurus* and the CP of *S. cerevisiae*. The structural data were expected to explain observed differences in the substrate specificities of the iCP and cCP. Moreover the structural characterization aimed at providing insights into the generation of the distinct MHC I peptide patterns by the cCP and iCP and into the pivotal role of the iCP in the adaptive immune system of vertebrates. Besides the examination of the cleavage preferences, it was intended to elucidate the molecular basis for the (non-) selectivity of known CP inhibitors. In particular, cCP and iCP structures in complex with the iCP-specific epoxyketone inhibitor ONX 0914 were supposed to unravel the reason for its  $\beta 5i$  selectivity.

Amino acid substitutions in the substrate binding channel are known to affect cleavage and inhibitor specificities. To evaluate the impact of amino acid differences between  $\beta 5$  subunits on the proteolytic activity mutagenesis experiments with the model organism *S. cerevisiae* were envisioned. These aimed at imitating the active site surroundings of subunit  $\beta 5c$ ,  $\beta 5i$  and  $\beta 5t$ . Structural data on these mutant yCPs and analysis of their affinity towards ONX 0914 and bortezomib were expected to reveal the effect of the amino acid substitutions on substrate and inhibitor specificities.

In summary, a multidisciplinary approach combining X-ray crystallography, yeast mutagenesis and inhibition assays was intended to provide detailed information on the architecture of all active sites of murine CP types for the development of potential lead structures for diverse medicinal applications.

## 5 Materials and Methods

### 5.1 Materials

#### 5.1.1 Chemicals

All chemicals were obtained from the following companies:

AppliChem (Darmstadt, DE), Biomol (Hamburg, DE), Fluka (Neu-Ulm, DE), Merck (Darmstadt, DE), Sigma-Aldrich (Steinheim, DE), Serva (Heidelberg, DE), Roth (Karlsruhe, DE) and VWR (Darmstadt, DE).

#### 5.1.2 Antibiotics

Ampicillin was used in a final concentration of 180 mg/l for the selection of transformed *Escherichia coli* (*E. coli*).

#### 5.1.3 Media

<u>LB<sub>0</sub> medium</u>	Peptone	1 % (w/v)
	Yeast extract	0.5 % (w/v)
	NaCl	0.5 % (w/v)
	(Agar	2 % (w/v))
<u>SOC medium</u>	Peptone	2 % (w/v)
	Yeast extract	0.5 % (w/v)
	Glucose	20 mM
	MgSO <sub>4</sub>	10 mM
	NaCl	10 mM
	MgCl <sub>2</sub>	10 mM
	KCl	2.5 mM
<u>YPD medium</u>	Yeast extract	1 % (w/v)
	Peptone	2 % (w/v)
	Glucose	2 % (w/v)
	(Agar	2 % (w/v))

<u>Synthetic complete medium (CM)</u>	Dropout Powder	0.13 % (w/v)
	Yeast Nitrogen Base w/o aa	0.67 % (w/v)
	Glucose	2 % (w/v)
	pH 5.6	
<u>CM medium ura<sup>-</sup> leu<sup>-</sup> his<sup>-</sup></u>	2x CM medium	300 ml
	4 % (w/v) Agar	300 ml
	40 % (w/v) Glucose	30 ml
	Adenine (30 mM)	6 ml
	Tryptophane (40 mM)	6 ml
	Lysine (100 mM)	6 ml
<u>CM medium leu<sup>-</sup> his<sup>-</sup> 5-FOA</u>	2x CM medium	300 ml
	4 % (w/v) Agar	300 ml
	40 % (w/v) Glucose	30 ml
	Adenine (30 mM)	6 ml
	Tryptophane (40 mM)	6 ml
	Lysine (100 mM)	6 ml
	Uracil (20 mM)	15 ml
	5-fluoroorotic acid (5-FOA)	0.6 g

#### 5.1.4 Enzymes

Phusion DNA Polymerase (2 U/μl)	Finnzymes (Vantaa, FI)
Pfu Turbo DNA Polymerase <sup>®</sup>	Agilent (Santa Clara, US)
Restriction endonuclease <i>Bam</i> HI (20 U/μl)	New England Biolabs (Ipswich, US)
Restriction endonuclease <i>Hind</i> III (20 U/μl)	New England Biolabs (Ipswich, US)
Restriction endonuclease <i>Dpn</i> I (20 U/μl)	New England Biolabs (Ipswich, US)
T4 DNA Ligase (1 U/μl)	Invitrogen (Carlsbad, US)
DNase I	Sigma-Aldrich (St. Louis, US)

### 5.1.5 Primer

All oligonucleotides were either HPSF or HPLC purified and dissolved in ddH<sub>2</sub>O to a final concentration of 100 pmol/μl. The working concentration of the primer was 10 pmol/μl. All primer were synthesized by Eurofins MWG Operon, Ebersberg.

<i>Primer</i>	<i>Sequence 5' → 3'</i>
5/6F	GAAACAGCTATGACCATGAT
5/6R	GACGGCCAGTGAATTGTAAT
20S_22C_for	AGATTCTCGTT/GCCACTTGTGGCAATTG
20S_22C_rev	CAATTGCCACAAGTGGG/CACGAGAATCT
27S_31M_rev	CTTCAC/TAGTTTGAGAAGC/AAACCCAATTGC
31M_for	CTTCTCAAACCTG/ATGAAGAAAGTTATTG
31M_for2	CTTCTCAAACCTATGAAGAAAGTTATTGAG
31S_for	TCTCAAACCTTCTAAGAAAGTTATTG
31S_rev	CAATAACTTTCTTAGAAGTTTGAGA
45T_48T_for	TGGGTACAACCTCCGGTACTGCGGCAG
45T_48T_rev	CTGCCGCAGTACCGGAAGTTGTACCCA
57R_for	TTTTGGGAACGTTGGCTAGGT
57R_rev	ACCTAGCCAACGTTCCCAAAA
32N_for	CTCAAACCTG/ATGAATAAAGTTATTG
32N_rev	CAATAACTTTATTTCAT/CAGTTTGAG
53S_for	GGCAGATTGTTTCATTTTGGG
53S_rev	CCCAAAATGAACAATCTGCC
53S_57R-for	GTTTCATTTTGGGAACGTTGGCTAGGTTCT
53S_57R-rev	CAACGTTCCCAAAATGAACAATCTGCCCG
SCSTRNG-M45A_for	CATTTTTATTGGGTACCGCGTCTGGTTGTGCGGCAG
SCSTRNG-M45A_rev	CTGCCGCACAACCAGACGCGGTACCCAATAAAAATG
SCSTRNG-M45V_for	CATTTTTATTGGGTACCGTTTCTGGTTGTGCGGCAG
SCSTRNG-M45V_rev	CTGCCGCACAACCAGAAACGGTACCCAATAAAAATG
71G_for	CGAGCTGAGGGAAGGTGAACGTATATCGC
71G_rev	GCGATATACGTTCCACCTCCCTCAGCTCG
127T_for	GACATATTCTGCACCTGGTTCAGGTCAA
127T_rev	TTGACCTGAACCAAGTGCAGAATATGTC

**Table 1** Oligonucleotides used in this work. Underlined nucleotides encode mutations.

### 5.1.6 Strains

<i>Organism</i>	<i>Strain</i>	<i>Genotype</i>	<i>Source</i>
<i>E. coli</i>	XL1-Blue	<i>recA1, endA1, gyrA96, thi-1, hsdR17, supE44, relA1, lac, [F', proAB, lacI<sup>q</sup>ZΔM15, Tn10 (Tet<sup>r</sup>)]</i>	Bullock <i>et al.</i> , 1987 <sup>[79]</sup>
<i>E. coli</i>	DH5α	<i>fhuA2 Δ(argF-lacZ)U169 phoA glnV44 Φ80 Δ(lacZ)M15 gyrA96 recA1 relA1 endA1 thi-1 hsdR17</i>	Hanahan, 1983 <sup>[80]</sup>
<i>S. cerevisiae</i>	WCG4a	<i>MATa leu2-3,112 ura3 his3-11,15 Can<sup>S</sup> GAL2</i>	Heinemeyer <i>et al.</i> , 1993 <sup>[81]</sup>
<i>S. cerevisiae</i>	WCG4a <i>pre1-1</i>	<i>MATa leu2-3,112 ura3 his3-11,15 rad5-535 Can<sup>S</sup> GAL2 pre1-1 (S142F)</i>	Heinemeyer <i>et al.</i> , 1991 <sup>[82]</sup>
<i>S. cerevisiae</i>	YWH20a	<i>MATa leu2-3,112 ura3 his3-11,15 Can<sup>S</sup> GAL2 pre2Δ::HIS3 [pRS316-E2]</i>	Heinemeyer <i>et al.</i> , 1997 <sup>[83]</sup>

**Table 2** *E. coli* and yeast strains used in this work.

The *E. coli* strains XL1-Blue and DH5α were used for cloning of mutant *pre2* genes in the vector pRS315. The created plasmids were introduced in *S. cerevisiae* YWH20a. *S. cerevisiae* WCG4a and WCG4a *pre1-1* served as control strains in proteasome activity tests (see section 5.4.1).

### 5.1.7 Plasmids

#### pRS315

The plasmid pRS315 is a pBluescript-based centromere vector composed of 6 kbp. The plasmid encodes the enzyme β lactamase, thereby conferring resistance to ampicillin and enabling selection in *E. coli*. The yeast selectable marker gene is *LEU2*. *Pre2* mutant genes of 1.5 kbp were inserted via the restriction sites *Bam*HI and *Hind*III into the multiple cloning site. Expression of the *pre2* mutants was controlled by the endogenic *PRE2* promoter.

#### pRS316-E2

The plasmid pRS316 is pBluescript-based centromere vector composed of 4.9 kbp encoding the ampicillin resistance gene and the *URA3* selection marker, suitable for replication in both

*E. coli* and yeast. Expression of the wildtype (wt) *PRE2* gene, inserted via the restriction sites *Bam*HI and *Hind*III, was under the control of the endogenic *PRE2* promoter.

<i>Plasmid</i>	<i>Mutations</i>	<i>Mimic</i>	<i>Source</i>
pRS315- <i>PRE2</i>	-	wt	W. Heinemeyer
pRS315- <i>pre2 Q53S</i>	Q53S	β5c	This work
pRS315- <i>pre2 S</i>	A46S	β5i	This work
pRS315- <i>pre2 C</i>	G48C	β5i	This work
pRS315- <i>pre2 SC</i>	A46S, G48C	β5i	This work
pRS315- <i>pre2 MSC</i>	V31M, A46S, G48C	β5i	This work
pRS315- <i>pre2 SSC</i>	A27S, A46S, G48C	β5i	This work
pRS315- <i>pre2 SMSC</i>	A27S, V31M, A46S, G48C	β5i	This work
pRS315- <i>pre2 SCT</i>	A46S, G48C, V127T	β5i	This work
pRS315- <i>pre2 SSCT</i>	A27S, A46S, G48C, V127T	β5i	This work
pRS315- <i>pre2 MSCT</i>	V31M, A46S, G48C, V127T	β5i	This work
pRS315- <i>pre2 SMSCT</i>	A27S, V31M, A46S, G48C, V127T	β5i	This work
pRS315- <i>pre2 SMSCRT</i>	A27S, V31M, A46S, G48C, T57R, V127T	β5i	This work
pRS315- <i>pre2 SNSCRT</i>	A27S, K32N, A46S, G48C, T57R, V127T	β5i	This work
pRS315- <i>pre2 SNSCRGT</i>	A27S, K32N, A46S, G48C, T57R, K71G, V127T	β5i	This work
pRS315- <i>pre2 SNASCRGT</i>	A27S, K32N, M45A, A46S, G48C, T57R, K71G, V127T	β5i	This work
pRS315- <i>pre2 SNVSCRGT</i>	A27S, K32N, M45V, A46S, G48C, T57R, K71G, V127T	β5i	This work
pRS315- <i>pre2 R</i>	M45R	β5i	W. Heinemeyer <sup>[84]</sup>
pRS315- <i>pre2 TR</i>	I35T, M45R	β5i	W. Heinemeyer <sup>[84]</sup>
pRS315- <i>pre2 SCS</i>	A20S, A22C, A46S	β5t	This work
pRS315- <i>pre2 SS</i>	V31S, A46S	β5t	This work
pRS315- <i>pre2 SCSS</i>	A20S, A22C, V31S, A46S	β5t	This work
pRS315- <i>pre2 TST</i>	M45T, A46S, G48T	β5t	This work
pRS315- <i>pre2 STST</i>	V31S, M45T, A46S, G48T	β5t	This work
pRS315- <i>pre2 SCTST</i>	A20S, A22C, M45T, A46S, G48T	β5t	This work
pRS315- <i>pre2 SCSTST</i>	A20S, A22C, V31S, M45T, A46S, G48T	β5t	This work

**Table 3** Plasmids used or created in this work.

### 5.1.8 Fluorogenic substrates

Cbz-Gly-Gly-Leu-pNA	Bachem (Bubendorf, Switzerland)
Suc-Leu-Leu-Val-Tyr-AMC	Bachem (Bubendorf, Switzerland)
Cbz-Leu-Leu-Glu-AMC	Bachem (Bubendorf, Switzerland)

All fluorogenic substrates were dissolved in DMSO and stored at -20 °C.

### 5.1.9 DNA and protein standards

peqGOLD DNA Ladder Mix (100 -10 000 bp)	Peqlab (Erlangen, DE)
Roti <sup>®</sup> -Mark STANDARD (14-200 kDa)	Carl Roth (Karlsruhe, DE)

### 5.1.10 Instruments

#### Balances

Analytical Balance TE124S	Sartorius (Göttingen, DE)
Precision Balance BP3100 P	Sartorius (Göttingen, DE)

#### Centrifuges

Biofuge Pico	Heraeus Instruments (Hanau, DE)
SIGMA 4K15 rotor 11150/13220	SIGMA Laborzentrifugen
rotor 11150/13350	(Osterode am Harz, DE)
SIGMA 6-16K rotor 12500	SIGMA Laborzentrifugen
	(Osterode am Harz, DE)
SIGMA 8K rotor 11805	SIGMA Laborzentrifugen
	(Osterode am Harz, DE)

#### Crystallography

Art Robbins Instruments Intelli-Plates (96 well)	Dunn Labortechnik (Asbach, DE)
Art Robbins Instruments Phoenix	Dunn Labortechnik (Asbach, DE)
Cooled Incubator Series 3000	RUMED <sup>®</sup> Rubarth Apparate (Laatzen, DE)
CrystalCap HT <sup>™</sup> für CryoLoop <sup>™</sup>	Hampton (Aliso Viejo, US)
CrystalCap HT <sup>™</sup> Vial	Hampton (Aliso Viejo, US)
CrystalWand Magnetic <sup>™</sup>	Hampton (Aliso Viejo, US)
Foam dewar	Spearlab (San Francisco, US)
Magnetic Caps, Pins and Vials	Molecular Dimensions (Newmarket, UK)
MICORLAB <sup>®</sup> STARlet	Hamilton (Reno, US)
Micro Tool Box	Molecular Dimensions (Newmarket, UK)
Mounted CryoLoop <sup>™</sup>	Hampton (Aliso Viejo, US)
Protein Crystallization Screening Suites	QIAGEN (Hilden, DE)
Quick Combi Sealer Plus	HJ-Bioanalytik (Mönchengladbach, DE)

Siliconized Glass Cover Slides	Hampton (Aliso Viejo, US)
SuperClear Pregreased 24 Well Plate	Crystalgen (New York, US)
Vial clamp	Molecular Dimensions (Newmarket, UK)
Zoom stereo microscope SZX10/KL1500LCD	Olympus (Tokio, JP)

### Electrophoresis

Chamber and tray	Appligene (Watford, UK)
Digital Graphic Printer UP-D897	Sony (Minato, JP)
Electrophoresis Power Supply EPS 600	Pharmacia Biotech (Uppsala, SE)
Gel documentation system G:BOX	Syngene (Cambridge, US)
Mini PROTEAN <sup>®</sup> Cell	BioRad (Hercules, US)
PowerPac Basic Power Supply	BioRad (Hercules, US)

### Liquid chromatography

ÄKTAprime <sup>™</sup> plus	GE Healthcare (Chalfont St. Giles, UK)
ÄKTApurifier <sup>™</sup>	GE Healthcare (Chalfont St. Giles, UK)
CHT <sup>™</sup> Ceramic Hydroxyapatite	BioRad (Hercules, US)
Phenyl Sepharose 6 Fast Flow	GE Healthcare (Chalfont St. Giles, UK)
RESOURCE <sup>™</sup> Q, 6 ml	GE Healthcare (Chalfont St. Giles, UK)
HiPrep <sup>™</sup> 26/10 desalting column	GE Healthcare (Chalfont St. Giles, UK)

### Additional equipments and materials

Cary Eclipse Fluorescence spectrometer	Varian (Darmstadt, DE)
NanoPhotometer <sup>™</sup> Pearl	IMPLEN (München, DE)
Ultraspec10 Cell Density Meter	Amersham Bioscience (Uppsala, SE)
Constant Cell Disruption System E1061	Constant Systems (Northants, UK)
Electroporation cuvette, 2 mm	PeqLab (Erlangen, DE)
Gene Pulser mit Pulse Controller	BioRad (Hercules, US)
Incubator	Binder (Tuttlingen, DE)
Infors HT Multitron 2 Cell Shaker	INFORS HT (Bottmingen/Basel, CH)
inoLab <sup>®</sup> pH 720 pH-Meter	WTW (Weilheim, DE)
Laboklav 25/195	SHP Steriltechnik (Magdeburg, DE)
MR Hei-Standard Magentic stirrer	Heidolph (Schwabach, DE)
Techne Dri-Block DB 2A	Bibby Scientific (Stone, UK)

Thermomixer comfort	Eppendorf (Hamburg, DE)
Thermocycler MyCycler™	BioRad (Hercules, US)
Vortex Genie 2	Scientific Industries (New York, US)
White 96 well plate NUNC	Thermo scientific (München, DE)

### 5.1.11 Computer software and bioinformatics tools

ApE – A plasmid Editor	Wayne Davis, M.
BOBSCRIPT	Esnouf, R. M. <sup>[85]</sup>
CCP4 Software Suite	www.ccp4.ac.uk <sup>[86]</sup>
ChemDraw	Perkin Elmer (Cambridge, US)
Coot	Emsley, P. <sup>[87]</sup>
CorelDRAW X5	Corel (Ottawa, CA)
DNAMAN	Lynnon Corporation (Quebec, CA)
EndNote X4	Adept Scientific (Frankfurt, DE)
GraphPad Prism 5	GraphPad Software Inc. (La Jolla, USA)
MAIN	Turk, D. <sup>[88]</sup>
Microsoft Office	Microsoft (Redmond, US)
MOLSCRIPT	Kraulis P. J. <sup>[89]</sup>
PyMOL Molecular Graphics System	Schrödinger, LLC <sup>[90]</sup>
QuikChange® Primer Design Tool	Agilent Technologies
Sybyl	Tripos (St. Louis, US) <sup>[91]</sup>
UNICORN™ control software	GE Healthcare (Chalfont St. Giles, UK)
XDS Program Package	Kabsch, W. (Heidelberg, DE) <sup>[92]</sup>

DNA and protein sequences were obtained from the “Universal protein resource” ([www.uniprot.org](http://www.uniprot.org)). The ProtParam tool (<http://www.expasy.ch/tools/protparam.html>) was used to calculate physical and chemical parameters such as molecular mass, pI and the extinction coefficient of protein sequences. Multiple DNA or protein sequences were aligned with the T-Coffee tool (<http://www.ebi.ac.uk/Tools/t-coffee/index.html>). For the calculation of protein surface areas the online tool PISA (Protein interfaces, surfaces and assemblies service PISA at European Bioinformatics Institute ([http://www.ebi.ac.uk/pdbe/prot\\_int/pistart.html](http://www.ebi.ac.uk/pdbe/prot_int/pistart.html))<sup>[93]</sup>) was used.

## 5.2 Genetic methods

### 5.2.1 Cultivation and long-term storage of *Escherichia coli*

*E. coli* were cultivated either in liquid LB<sub>Amp</sub> medium or on LB<sub>Amp</sub> agar plates. Liquid cultures were inoculated from single colonies and incubated at 37 °C and 130 rpm in a shaker. Streaks on agar plates were grown overnight at 37 °C and later on stored at 4 °C in the fridge. For long-term preservation of *E. coli* clones glycerol stocks were prepared: an overnight culture was pelleted for 5 min at 3 000 rpm, cells were resuspended in LB<sub>0</sub> medium containing 30 % (v/v) glycerol, transferred into a cryo tube and frozen in liquid nitrogen.

### 5.2.2 Cultivation and long-term storage of *Saccharomyces cerevisiae*

Baker's yeast was cultivated at 30 °C either on agar plates or in liquid medium. Wt and mutant yeast strains were streaked on YPD plates or on CM plates containing the appropriate selection marker composition. Agar plates were stored for 2 to 3 days at 30 °C and later on kept at 4 °C in the fridge. For the large scale cultivation of yeast in liquid medium 50-300 ml YPD medium were inoculated with a single colony grown on a YPD agar plate. After incubation for 12-24 h at 130 rpm this preculture was used to inoculate the main culture of 3-18 l of YPD medium in a ratio of 1:50. The main culture was grown up to 48 h at 30 °C and 130 rpm to an OD<sub>600nm</sub> of approximately 7 and subsequently harvested for 20 min at 5 000 rpm. The cells were washed in ddH<sub>2</sub>O, transferred into 50 ml falcons, centrifuged again and finally frozen at -20 °C. For long-term storage of *S. cerevisiae* clones glycerol stocks were prepared: With a sterile toothpick cells were scraped off from an agar plate, resuspended in 1 ml of 15 % (v/v) glycerol, transferred into a cryo tube and frozen at – 80 °C.

### 5.2.3 Polymerase chain reaction

The polymerase chain reaction (PCR) served to amplify target genes encoded on genomic DNA or plasmids<sup>[94]</sup>. Annealing temperatures were chosen 5 °C below the melting temperatures (T<sub>m</sub>) of the used primers. The T<sub>m</sub> was calculated according to formula 1 or by the QuikChange<sup>®</sup> Primer Design Tool from Agilent Technologies.

$$T_m = 2^{\circ}\text{C} \cdot (B_{\text{Adenin}} + B_{\text{Thymin}}) + 4^{\circ}\text{C} \cdot (B_{\text{Guanin}} + B_{\text{Cytosin}})$$

**Formula 1: Calculation of the melting temperature of oligonucleotides.**

In general, PCR reactions were performed according to the following pipetting and temperature schemes:

<i>Compound</i>	<i>Final concentration</i>	<i>Volume [<math>\mu</math>l]</i>
Template	0.001-0.01 ng/ $\mu$ l	1-5
dNTP-Mix (10 mM)	0.2 mM	2
Forward Primer (10 pmol/ $\mu$ l)	0.5 $\mu$ M	5
Reverse Primer (10 pmol/ $\mu$ l)	0.5 $\mu$ M	5
Phusion <sup>®</sup> HF buffer (5x)	1x	20
Phusion <sup>®</sup> DNA polymerase (2 U/ $\mu$ l)	0.02 U/ $\mu$ l	1
ddH <sub>2</sub> O		Fill up to 100

**Table 4** Components of a PCR reaction using the Phusion<sup>®</sup> DNA polymerase.

<i>PCR step</i>	<i>Temperature</i>	<i>Time</i>	
Initial denaturing	95 °C	3 min	
Denaturing	95 °C	30 sec	} 35 cycles
Annealing	55 °C	30 sec	
Elongation	72 °C	variable	
Final elongation	72 °C	10 min	
Cooling	4 °C	$\infty$	

**Table 5** Temperature program for PCR reactions using the Phusion<sup>®</sup> DNA polymerase.

For site-directed mutagenesis alternatively the QuikChange<sup>®</sup> PCR was used (see also section 5.2.4):

<i>Compound</i>	<i>Final concentration</i>	<i>Volume [<math>\mu</math>l]</i>
Template	0.2-1 ng/ $\mu$ l	x
dNTP-Mix (10 mM)	0.2 mM	1
Forward Primer (10 pmol/ $\mu$ l)	2.5 ng/ $\mu$ l	y
Reverse Primer (10 pmol/ $\mu$ l)	2.5 ng/ $\mu$ l	z
Pfu buffer (10x)	1x	5
Pfu Turbo DNA polymerase <sup>®</sup>		1
ddH <sub>2</sub> O		Fill up to 50

**Table 6** Components of a PCR reaction using the Pfu Turbo DNA polymerase<sup>®</sup>.

<i>PCR step</i>	<i>Temperature</i>	<i>Time</i>	
Initial denaturing	95 °C	30 sec	
Denaturing	95 °C	30 sec	} 16 cycles
Annealing	55 °C	1 min	
Elongation	68 °C	7.5 min	
Cooling	4 °C	$\infty$	

**Table 7** Temperature program for QuikChange<sup>®</sup> PCR reactions.

### 5.2.4 Site-directed mutagenesis

Mutations in the yeast proteasome gene *PRE2* encoding the subunit  $\gamma\beta 5$  were introduced either via recombinant PCR techniques or QuikChange<sup>®</sup> mutagenesis.

The first method required three PCR reactions and four oligonucleotides two of which encoding the desired mutation:

**PCR 1a:** Primer 5/6F and Mutation\_rev Primer; elongation time 45 s

**PCR 1b:** Primer 5/6R and Mutation\_for Primer; elongation time 45 s

**PCR 2:** Primer 5/6F and 5/6R with the PCR products 1a and 1b as template; elongation time 90 s.

The PCR product 2 was digested, inserted into the vector pRS315 and subsequently transformed into *E. coli*.

The QuikChange<sup>®</sup> mutagenesis<sup>[95]</sup> required two HPLC purified primers, containing the desired mutation. Usually, different amounts of template DNA were tested. After the PCR reaction 1  $\mu$ l of the restriction endonuclease *DpnI* was added and the sample was incubated for 1.5 h at 37 °C. *DpnI* selectively degraded only the methylated template DNA. Finally, 3  $\mu$ l DNA were transformed into *E. coli* and all cells were streaked on an LB<sub>Amp</sub> agar plate.

### 5.2.5 Agarose gel electrophoresis

For analytical and preparative separations of DNA 1 % (w/v) agarose gels in 1x Tris-Acetate-EDTA buffer (TAE) were used. Samples were supplemented with DNA loading dye (final concentration: 1x) and loaded on the gel. Electrophoresis was carried out for 40 min in 1x TAE buffer at 120 V. Staining of the gel in a solution of 1 mg/l ethidium bromide for 20 min enabled visualization of DNA bands under UV light of 365 nm.

<u>DNA loading dye (10x)</u>	Tris-HCl, pH 8.2	10 mM
	EDTA	1 mM
	Glycerol	50 % (v/v)
	Xylene cyanole	0.25 % (w/v)
	Bromphenol blue	0.25 % (w/v)

<u>TAE buffer (50x)</u>	Tris-Ac, pH 8.2	2 M
	EDTA	100 mM

### 5.2.6 Isolation of plasmid DNA from *E. coli*

Isolation of plasmid DNA from *E. coli* was carried out with the peqGOLD Plasmid Miniprep Kit I or II according to the instruction manual. Purified plasmids were stored at -20 °C.

### 5.2.7 Purification of DNA

DNA was purified by the peqGOLD Gel extraction or the peqGOLD Cycle-Pure Kit according to the manufacturer's instruction. Purified DNA samples were stored at -20 °C.

### 5.2.8 Restriction digest of DNA

Preparative restriction digests of a total volume of 70 µl contained 40 U per restriction endonuclease in the recommended buffer and were incubated for 2 to 5 h at 37 °C. Analytical cleavages were performed in a total volume of 10 µl containing the appropriate buffer and 5 U per restriction endonuclease. Analytical digests were stored for 1.5 h at 37 °C.

<i>Compound</i>	<i>Final concentration</i>	<i>Volume [µl]</i>
DNA		Up to 52
NEB buffer 2 (10x)	1x	7
BSA (10x)	1x	7
<i>Bam</i> HI (20 U/µl)	0.6 U/µl	2
<i>Hind</i> III (20 U/µl)	0.6 U/µl	2
H <sub>2</sub> O		Add to 70

**Table 8 Pipetting scheme for preparative restriction digests.**

<i>Compound</i>	<i>Final concentration</i>	<i>Volume [µl]</i>
Plasmid		2
NEB buffer 2 (10x)	1x	1
BSA (10x)	1x	1
<i>Bam</i> HI (20 U/µl)	0.5 U/µl	0.25
<i>Hind</i> III (20 U/µl)	0.5 U/µl	0.25
H <sub>2</sub> O		5.5

**Table 9 Pipetting scheme for analytical restriction digests.**

### 5.2.9 Determination of DNA concentration

DNA concentrations were determined by measuring the absorption at 260 nm with the nanophotometer (IMPLEN); an OD<sub>260nm</sub> of 1 corresponds to a concentration of 50 ng/μl DNA.

### 5.2.10 Ligation of DNA fragments

Vector and insert amounts were calculated according to formula 2.

$$m_{insert} = \frac{m_{vector} \cdot bp_{insert}}{bp_{vector}} \cdot x$$

**Formula 2: Calculation of vector and insert amounts for the ligation of DNA fragments.** For standard reactions  $m_{vector}$  was 50-100 ng and  $x = 3-5$ .

<i>Compound</i>	<i>Final concentration</i>	<i>Volume [μl]</i>
Plasmid	5-10 ng/μl	x
Insert		y
H <sub>2</sub> O		7.5-(x+y)
T4 DNA ligation buffer (5x)	1x	2
T4 DNA ligase (1 U/μl)	0.05 U/μl	0.5

**Table 10: Pipetting scheme for the ligation of DNA fragments.**

To unwind DNA fragments both plasmid and insert were incubated for 10 min at 55 °C and for 5 min on ice. Afterwards ligation buffer and T4 ligase were added. The sample was either kept at 4 °C overnight or at room temperature for one hour.

### 5.2.11 Transformation of *E. coli* by electroporation

40 μl of electrocompetent *E. coli* cells and 1 μl of plasmid DNA were mixed and transferred into a 2 mm electroporation cuvette. Transformation of *E. coli* was achieved by applying a high voltage pulse of approximately 5.7 ms and 2500 V<sup>[96]</sup>. Subsequently, cells were resuspended in 1 ml of SOC medium and incubated for 1 h at 37 °C and 500 rpm shaking to recover. Different dilutions of cells were plated on agar plates containing ampicillin.

### 5.2.12 Transformation of *S. cerevisiae*

*S. cerevisiae* was transformed according to the LiAc method by Gietz and Woods<sup>[97]</sup>. Yeast cells were picked with a sterile toothpick and resuspended in 1 ml of sterile water. After a short spin down at 13 000 rpm for 30 sec the supernatant was discarded and the pelleted cells were taken up in 1xTE/LiAc buffer. An additional step of centrifugation followed. Then, yeast cells were resuspended in x times 50 µl 1x TE/LiAc and x times 4 µl boiled single stranded salmon carrier DNA from salmon testes (Sigma-Aldrich (St. Louis, US)). The resulting cell suspension was split into x tubes and each was supplemented with 5 µl of plasmid DNA to be transformed and 300 µl of PEG3350/TE/LiAc (8:1:1). The samples were gently mixed and incubated for 30 min at 30 °C. After cells have been heated to 42 °C for 20 min, they were centrifuged for 2 min at 2 000 rpm, resuspended in 100 µl 1xTE buffer and streaked on CM ura<sup>-</sup> leu<sup>-</sup> his<sup>-</sup> plates.

<u>TE buffer (10x)</u>	Tris-HCl, pH 7.4	100 mM
	EDTA	10 mM
<u>LiAc (10x)</u>	LiAc, pH 7.5	1 M
<u>PEG3350 (10x)</u>	PEG3350	50 % (w/v)

### 5.2.13 Plasmid shuffling

Yeast proteasome mutants were created by the plasmid shuffling procedure<sup>[98]</sup>. The haploid yeast strain YWH20a, which is chromosomally deleted in its wildtype *PRE2* gene and instead carries a wt gene copy on an *URA3* episome (pRS316), was transformed by *pre2* gene variants, encoded on the plasmid pRS315 carrying the *LEU2* selection marker (see Table 3). 2 to 3 days after the transformation single colonies were picked, streaked either on an YPD or CM leu<sup>-</sup> his<sup>-</sup> plate as patches and grown for additional 2 days at 30 °C. To select for clones that have lost the wt *PRE2* gene copy, transformants were grown on CM leu<sup>-</sup> his<sup>-</sup> medium containing 5-FOA. Optionally, after 2 to 3 days of incubation at 30 °C a second round of 5-FOA selection can be made. Finally, single colonies were picked from the 5-FOA containing plates and transferred onto YPD agar. Due to the indispensable need for a functional *PRE2* gene for yeast survival no further selection was required.

### 5.2.14 DNA isolation from *S. cerevisiae*

Yeast cells were scraped off from an agar plate with a toothpick and resuspended in 500 µl of ddH<sub>2</sub>O. Cells were centrifuged for 30 sec at 14 000 rpm. The cell pellet was taken up in 200 µl of breaking buffer. After the addition of 200 µl of glass beads (0.5 mm) and 200 µl of phenol/chloroform/isoamyl alcohol (25:24:1) solution, the samples were vortexed for 2 min. Cell debris was pelleted by centrifugation for 5 min at 14 000 rpm. 100 µl supernatant were mixed with 10 µl 3 M sodium acetate, pH 6.0 and 280 µl 100 % ethanol and subsequently stored at -80 °C for 5 min to precipitate nucleic acids. After a centrifugation step for 5 min at 14 000 rpm the supernatant was discarded and the pellet containing the nucleic acids was washed with 300 µl 70 % ethanol. Following an additional centrifugation step (5 min; 14 000 rpm) the pellet was dried at room temperature and finally dissolved in 50-100 µl TE-buffer and 0.5-1 µl RNase (10 µg/µl). 1 µl of this solution was used as a template for further PCR analysis.

<u>Breaking buffer</u>	Tris-HCl, pH 8.0	10 mM
	NaCl	100 mM
	EDTA	1 mM
	SDS	1 % (w/v)
	Triton X-100	2 % (v/v)

### 5.2.15 DNA sequencing

DNA sequence analysis was performed according to Sanger *et al.*<sup>[99]</sup> by GATC Biotech AG, Konstanz. The results obtained by sequencing were compared to the corresponding entries in the Uniprot database.

### 5.3 Protein chemistry and analytics

#### 5.3.1 Purification of the yeast 20S proteasome

Purification of wt and mutant yCPs was carried out together with the technician Richard Feicht according to published procedures<sup>[100]</sup>. 120 g yeast cells were solubilized in approximately 150 ml of 50 mM KH<sub>2</sub>PO<sub>4</sub>/K<sub>2</sub>HPO<sub>4</sub> buffer pH 7.5. DNase I was added and the cells were disrupted with a French press. The cell lysate was centrifuged for 30 min at 21 000 rpm at 4 °C. The resulting supernatant was filtered and 30 % of saturated ammonium sulfate was added. Subsequently, the cell lysate was loaded on a Phenyl Sepharose<sup>TM</sup> 6 Fast Flow column pre-equilibrated with 1 M ammonium sulfate in 20 mM KH<sub>2</sub>PO<sub>4</sub>/K<sub>2</sub>HPO<sub>4</sub> buffer pH 7.5. The yCP was eluted by applying a linear gradient from 1 M to 0 M ammonium sulfate in 4 column volumes. Collected fractions were tested for proteolytic activity using the fluorogenic substrates Suc-Leu-Leu-Val-Tyr-AMC (for wt yCP) and Cbz-Leu-Leu-Glu-AMC (for β5 mutant yCPs): 30 μl of each fraction were incubated for 1 h with 1 μl of 10 mM substrate and the resulting fluorescence was measured ( $\lambda_{exc}$ =360 nm and  $\lambda_{em}$ =460 nm). Active fractions were pooled and applied to a hydroxyapatite column, which has been equilibrated with 20 mM KH<sub>2</sub>PO<sub>4</sub>/K<sub>2</sub>HPO<sub>4</sub> pH 7.5. Using a linear gradient from 20 mM to 500 mM KH<sub>2</sub>PO<sub>4</sub>/K<sub>2</sub>HPO<sub>4</sub> in 20 column volumes, the yCP was eluted. Proteolytically active fractions were loaded on a Resource Q column and a sodium chloride gradient from 0 mM to 500 mM in 20 mM Tris-HCl pH 7.5 was run over 10 column volumes. For crystallization the buffer was exchanged for 10 mM 2-(*N*-morpholino)ethanesulfonic acid (Mes) pH 6.8 using a HiPrep<sup>TM</sup> 26/10 desalting column.

#### 5.3.2 Purification of the murine immuno- and constitutive 20S proteasome

Immuno- and constitutive proteasome samples were kindly provided by Dr. Michael Basler and Ricarda Schwab from the group of Prof. Dr. Marcus Groettrup, University of Constance, Department of Biology/Immunology, Universitätsstr. 10, Constance, DE. The cCP was purified from livers of C57BL/6 *PSMB8* (β5i) and *PSMB10* (β2i) knockout mice according to published protocols<sup>[101]</sup>. iCP samples were prepared from livers of BALB/c mice eight days after their intravenous infection with 200 plaque-forming units of lymphocytic choriomeningitis virus strain WE (LCMV-WE)<sup>[101]</sup>. LCMV-WE selectively infects liver cells and leads to an almost complete conversion of the cCP to the iCP within eight days, when mice were sacrificed and livers removed. Purification of the iCP was carried out according to

established procedures<sup>[101]</sup>. For short-term storage and subsequent crystallisation trials samples were kept at 4 °C (in 10 mM Hepes pH 7.2, 300 mM KCl, 5 mM MgCl<sub>2</sub>), otherwise the protein was frozen at - 80 °C.

### 5.3.3 SDS polyacrylamide gel electrophoresis

Discontinuous SDS-PAGE was performed according to Laemmli<sup>[102]</sup>. Gels were run in 1x running buffer at 25 mA per gel until the front line has passed the bottom of the gel. SDS polyacrylamide gels were stained for 30 min with Coomassie solution and afterwards destained.

<i>Compound</i>	<i>Separating gel (12 %)</i>	<i>Stacking gel (4 %)</i>
Acrylamide	6 ml	1 ml
Separating gel buffer	5 ml	-
Stacking gel buffer	-	5 ml
H <sub>2</sub> O	9 ml	4 ml
APS (10 % (v/v))	100 µl	100 µl
TEMED (1 % (v/v))	10 µl	10 µl

**Table 11 Pipetting scheme for four SDS gels.**

<u>Acrylamide solution</u>	Acrylamide	39 % (w/v)
	Bisacrylamide	1.2 % (w/v)
<u>SDS-PAGE loading dye</u>	Tris-HCl, pH 6.8	60 mM
	Glycerol	30 % (v/v)
	Saccharose	10 % (w/v)
	SDS	5 % (w/v)
	Bromphenol blue	0.02 % (w/v)
	β Mercaptoethanol	3 % (v/v)
<u>Separating gel buffer</u>	Tris-HCl, pH 8.8	1.5 M
	SDS	0.4 % (w/v)
<u>Stacking gel buffer</u>	Tris-HCl, pH 6.8	0.5 M
	SDS	0.4 % (w/v)

<u>Running buffer</u>	Tris-HCl, pH 8.2-8.3	25 mM
	Glycine	192 mM
	SDS	0.1 % (w/v)
<u>Staining solution</u>	Coomassie Brilliant Blue R250	0.05 % (w/v)
	Isopropanol	25 % (v/v)
	Glacial acetic acid	10 % (v/v)
<u>Destaining solution</u>	Glacial acetic acid	10 % (v/v)

### 5.3.4 Determination of protein concentration

UV/VIS spectra of protein solutions were recorded with the nanophotometer of IMPLEN. The absorption at a wavelength of 280 nm was used to calculate protein concentrations via the Lambert-Beer law. The required theoretical molar extinction coefficient was computed with the ProtParam tool (yCP: 727.3 cm<sup>2</sup>/mmol, cCP: 685.0 cm<sup>2</sup>/mmol, iCP: 678.8 cm<sup>2</sup>/mmol).

## 5.4 Proteasome activity tests

### 5.4.1 Overlay assay

Yeast strains were streaked as patches on YPD plates and incubated for two days at 30 °C. Next, cells were replica plated on a steril filter paper lying on an YPD plate and grown for 48 h at 30 °C. The filter was placed in a glass Petri dish and the cells were lysed with 10 ml of chloroform for 15 min. After having dried the filter in a plastic petri dish 10 ml of hand warm overlay solution (1 % (w/v) agar, 50 mM Tris-HCl pH 8.0, 300 µl of 10 mM Cbz-Gly-Gly-Leu-pNA substrate in DMSO) were added. Incubation for 3 h at 30 °C was followed by exposure to 10 ml of 0.1 % (w/v) sodium nitrite solution in 1 M HCl for 5 min. Next, this solution was exchanged for 10 ml of 0.5 % (w/v) ammonium sulfamate solution in 1 M HCl and after 5 min again discarded. Finally, the filter was stored in 10 ml of 0.05 % (w/v) *N*-(1-naphthyl)ethylenediamine solution in 47 % (v/v) EtOH for 10 - 30 min. Cells with normal ChTL activity became pink, while those with defects were less coloured.

## 5.4.2 Fluorescence activity test and determination of IC<sub>50</sub> values

Proteasome activity and the inhibitory potency of ligands are routinely determined by fluorescence spectroscopy using AMC-peptides as substrates. CPs were mixed with a series of different inhibitor concentrations or DMSO as a control in 100 mM Tris-HCl, pH 7.4 and samples were stored for 45 min at room temperature to allow inhibitor binding. Next, the  $\beta$ 5-specific substrate Suc-Leu-Leu-Val-Tyr-AMC was added to a final concentration of 200  $\mu$ M. During the subsequent 60 min incubation at room temperature residual proteasome activity hydrolysed the substrate and released the AMC-fluorophor. After dilution (1:10) of the samples with 20 mM Tris-HCl, pH 7.4, which strongly slowed down the reaction, the relative fluorescence units (RFU) were measured with a Varian Cary Eclipse Fluorescence Spectrophotometer (Agilent Technologies) at  $\lambda_{exc}$ =360 nm and  $\lambda_{em}$ =460 nm. RFU values were normalized to the DMSO treated control, which should have retained nearly 100 % activity. The calculated residual activities were plotted against the logarithm of the applied inhibitor concentration and fitted to the equation  $Y = \text{Bottom} + (\text{Top} - \text{Bottom}) / (1 + 10^{((\text{LogIC}_{50} - X) * \text{HillSlope}))}$  (X: logarithm of inhibitor concentration; Y: Residual enzymatic activity; log(inhibitor) vs response – variable slope (four parameters), GraphPad Prism 5). The IC<sub>50</sub> value, the ligand concentration that leads to 50 % inhibition of the enzymatic activity, was deduced from the fitted data.

## 5.5 Protein crystallography

### 5.5.1 Crystallization of the yeast 20S proteasome

Purified yCP was concentrated to approximately 40 mg/ml at 5 000 rpm using an Amicon<sup>®</sup> Ultra-15 Centrifugal Filter device of 100 kDa cutoff. Crystals of the yCP were grown at 20 °C by the hanging drop vapour diffusion method in drops containing a 1:1 mixture of reservoir and protein solution. The reservoir solution (300  $\mu$ l) was composed of 25 mM magnesium acetate, 100 mM Mes pH 6.8 and 9-13 % (v/v) 2-methyl-2,4-pentanediol (MPD). Crystals were cryoprotected by the addition of 5  $\mu$ l of 20 mM magnesium acetate, 100 mM Mes, pH 6.8 and 30 % (v/v) MPD and immediately frozen in liquid nitrogen. Crystal soaking experiments were performed by supplementing crystal drops with 5  $\mu$ l cryoprotection solution and 0.3-3 mM of inhibitor for 2 to 24 hours. Afterwards crystals were super-cooled in liquid nitrogen.

### 5.5.2 Crystallization of the murine 20S proteasomes

Protein samples were concentrated to approximately 30 mg/ml at 5 000 rpm using Millipore centrifugal devices with a Cut-off of 30 kDa. Initial crystallization trials with the murine cCP and iCP were set up in 96-well sitting drop plates with a final drop size of 0.2  $\mu$ l containing a protein:reservoir ratio of 1:1. Hanging drop plates were set up with final drop volumes of 1  $\mu$ l. All plates were stored at 20 °C and crystals grew from MPD conditions within a few days. The iCP crystallized from a reservoir solution containing 0.2 M sodium iodide and 40 % MPD, whereas cCP crystals preferentially grew from 0.2 M sodium formate or 0.2 M potassium acetate and 40 % MPD. After addition of 1 to 5  $\mu$ l of reservoir solution cCP and iCP crystals were frozen in liquid nitrogen. cCP and iCP complex structures with ONX 0914 were obtained by soaking crystals with 3 mM ONX 0914 (dissolved in DMSO) in 1-5  $\mu$ l of reservoir solution for at least 8 h prior to freezing.

### 5.5.3 Data collection, processing and structure determination

Diffraction data were collected at the Swiss Light Source, Villigen, Switzerland at the beamlines X06SA (Pilatus 6M detector) and X06DA (MAR CCD detector) at a wavelength of 1.0 Å. For all data sets cryoprotection (100 K) was used. Indexing, integration and scaling of the obtained data was performed with the program package XDS<sup>[103]</sup>. All proteasome structures were solved by Patterson search calculations with PHASER using the maximum likelihood method<sup>[104]</sup>. For yCP:ONX 0914 complex structures the yCP apo crystal structure (PDB ID 1RYP<sup>[13]</sup>) served as a starting model and structure determination was performed as previously published<sup>[105]</sup>. Structure elucidation of the cCP and iCP was carried out by molecular replacement with the coordinates of the bovine cCP (PDB ID 1IRU<sup>[21a]</sup>). For rigid body, TLS (Translation/Libration/Screw) and positional refinements REFMAC5<sup>[106]</sup> was used. 4-Fold and 2-fold non-crystallographic symmetry averaging was applied for the cCP and iCP in refinement and model building, respectively. Model building was performed with the interactive three-dimensional graphic programs MAIN<sup>[88]</sup> and COOT<sup>[87]</sup>. Waters were placed with Arp/Warp<sup>[86]</sup>. Ligands were built with Sybyl<sup>[91]</sup> and their topology and parameter files were created by Sketcher<sup>[86]</sup>. Graphical illustration of crystal structures was performed with the programs MOLSCRIPT<sup>[89]</sup>, BOBSCRIPT<sup>[85]</sup> and PyMOL<sup>[90]</sup>. Conolly surfaces were calculated and depicted with GRASP<sup>[107]</sup>. The final coordinates were proven to have good stereochemistry according to the Ramachandran plot by using Procheck<sup>[86]</sup> as well as

reasonable  $R_{\text{work}}$ ,  $R_{\text{free}}$ , r.m.s.d. bond and angle values (see Table 12 and Table 13). The coordinates of published structures were deposited in the PDB under the following accession codes: 3UNH (iCP), 3UNE (cCP), 3UNF (iCP:ONX 0914), 3UNB (cCP:ONX 0914), 3UN8 (yCP:ONX 0914\_ep), 3UN4 (yCP:ONX 0914\_mo).

## 6 Results

### 6.1 Sequence alignments

The quaternary and tertiary structure of the 20S proteasome is strictly conserved from archaea to mammals and it is assumed that its two types of subunits, termed  $\alpha$  and  $\beta$ , evolved from a common ancestor protein<sup>[12-14, 21a, 32]</sup>. In this regard the catalytically active proteasome subunits of murine 20S proteasome types display high sequence identities to each other:  $\beta 1c/\beta 1i$ : 63.3 %,  $\beta 2c/\beta 2i$ : 58.9 %,  $\beta 5c/\beta 5i$ : 72.4.0 %,  $\beta 5c/\beta 5t$ : 54.4 %  $\beta 5i/\beta 5t$ : 50.5 % (Figure 8). Although sequence alignments are indicative of an overall conserved fold for all proteolytically active subunits, defined differences in their substrate binding channels give rise to different cleavage preferences in the cCP, iCP and tCP<sup>[13, 21c]</sup>. In particular, hydrophobic amino acids in the unprimed substrate binding pockets of subunit  $\beta 1i$  have been predicted to attenuate the CL activity and to increase the ChTL activity<sup>[13]</sup>. In contrast, the sequence analysis of the subunits  $\beta 2c/i$  and  $\beta 5c/i$  provided no hints on changes in the chemical properties of their substrate binding channels and on profound differences in their substrate specificities (Figure 8). However, for the vertebrate-specific subunit  $\beta 5t$ , which is exclusively expressed in cTECs<sup>[35b]</sup>, the primary sequence of its substrate binding channel is strongly altered. In particular, the polarity of the binding pockets appears to be dramatically increased, thereby leading to a markedly reduced ChTL activity and to a different peptide product pattern of the tCP (Figure 8C; see also chapter 6.4.3).

## Results

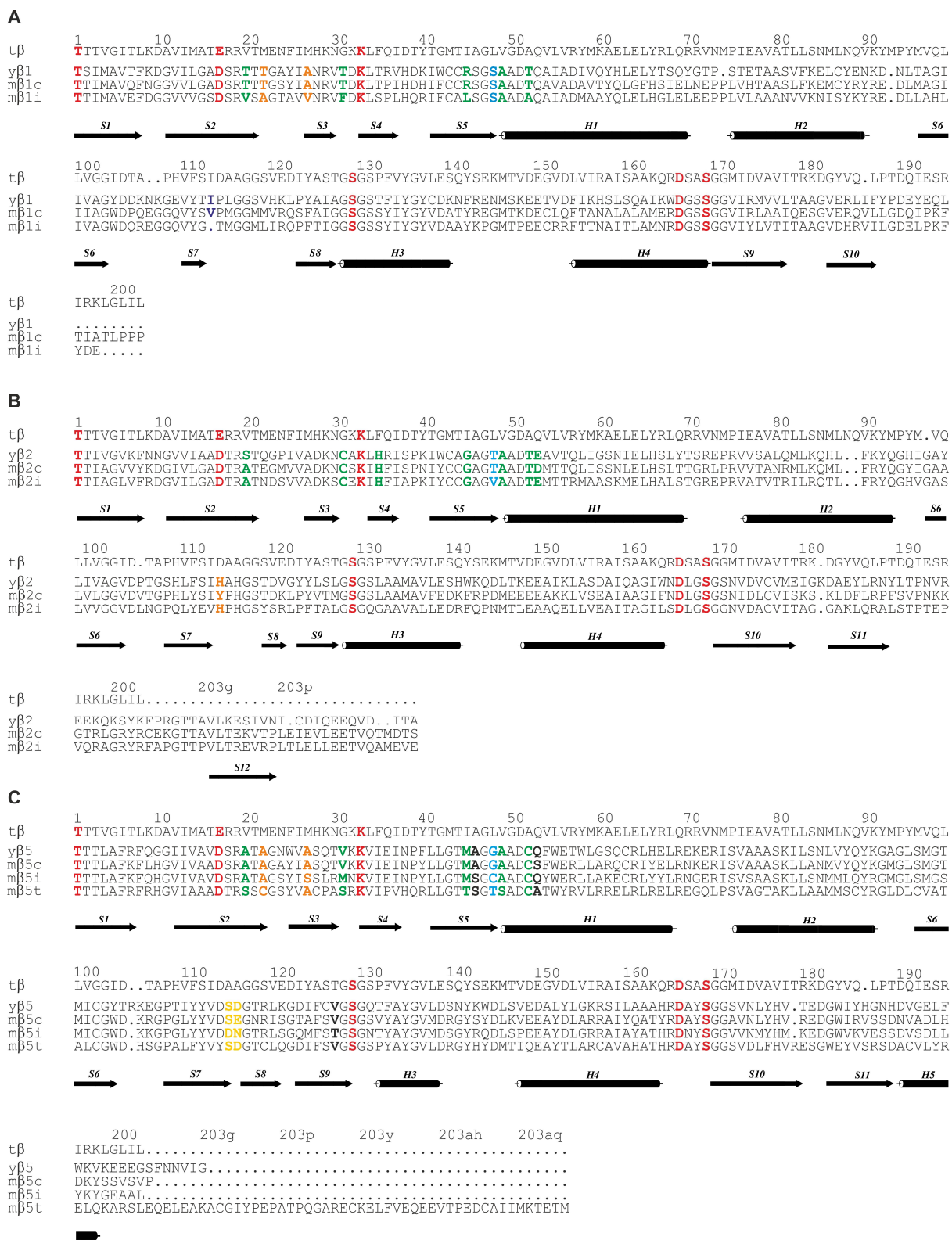


**Figure 8 Sequence alignments of active  $\beta$  subunits from archaeal (t), yeast (y) and murine (m) 20S proteasomes.** Protein sequences for (A)  $\beta$ 1, (B)  $\beta$ 2 and (C)  $\beta$ 5 subunits are given in the one-letter code. Amino acids are numbered according to the  $\beta$  subunit of the 20S proteasomes from the archaeon *T. acidophilum* (t); insertions are indicated by lower-case letters. Helices and sheets are depicted for the i subunits. Residues that are crucial for the catalytic activity are marked in red. The substrate specificity pocket forming amino acids are coloured in green (S1), blue (S2), orange (S3) and yellow (S'), respectively. Residue 113 is absent in all  $\beta$ 1i subunits (purple). Amino acids that are suggested to influence the active site architecture and proteolytic activity of subunit  $\beta$ 5 are highlighted in black.

Adapted from Huber *et al.*, 2012<sup>[32]</sup>.

## 6.2 X-ray structures of the mouse 20S immuno- and constitutive proteasome

### 6.2.1 Crystallization and structure determination

Infection of BALB/c mice with LCMV-WE leads to an efficient (95 %) conversion of cCPs to iCPs in the murine livers within eight days. The synthesized iCPs were purified according to published procedures<sup>[101]</sup>. The same purification procedure was applied to livers of uninfected gene targeted  $\beta 2i^{-/-}$  and  $\beta 5i^{-/-}$  C57BL/6 mice and yielded pure cCP samples (Figure 9).

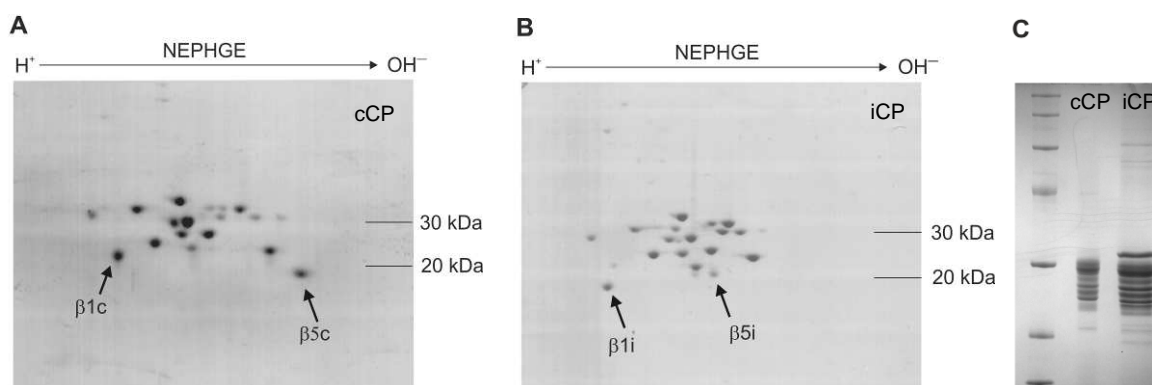


**Figure 9** Coomassie-stained gels of purified murine cCP and iCP samples used for crystallization trials. 2D non-equilibrium pH gradient gel electrophoresis (NEPHGE)/SDS-PAGE gels of (A) 80  $\mu$ g of purified cCP isolated from livers of  $\beta 2i^{-/-} \beta 5i^{-/-}$  gene targeted mice and (B) 80  $\mu$ g of iCP from livers of LCMV-WE infected BALB/c mice. Proteasome subunits were assigned according to Groettrup *et al.*, 1996<sup>[21b]</sup>. (C) One-dimensional SDS-PAGE analysis of cCP and iCP samples. Adapted from Huber *et al.*, 2012<sup>[32]</sup>.

In a joint collaboration with the group of Prof. Dr. Marcus Groettrup of the University of Constance, Dr. Michael Basler and Ricarda Schwab prepared appropriate amounts of murine iCP and cCP for crystallographic analysis. Samples were proven for their purity by 2D-PAGE (Figure 9), concentrated to approximately 30 mg/ml and subsequently subjected to initial sitting drop vapour diffusion crystallization trials. A sparse matrix screen of about 400 conditions was tested with a protein:reservoir ratio of 1:1 and a final drop volume of 0.2  $\mu$ l. Both CPs crystallized within a few days from various reservoir solutions containing 40 % MPD and different salts (Figure 10A). The obtained crystals were exposed to synchrotron X-ray radiation and their diffraction patterns were analysed (Figure 10B). Albeit their small size, crystals diffracted to a resolution of approximately 6  $\text{\AA}$ . However, due to disordered crystal lattices most diffractions patterns were not suitable for structure analysis. Crystal quality was improved by avoiding freezing of the protein samples, by filtering samples upon concentration and by extensive screening of crystallization conditions. Finally, high-quality crystals of the cCP and iCP with resolution limits of 3.2  $\text{\AA}$  were obtained (Table 12). After the successful collection of diffraction data for the cCP and iCP apo-structures, inhibitor soaking

## Results

experiments with the iCP-selective compound ONX 0914 were undertaken. Crystals of the cCP and iCP were exposed to ONX 0914 in a final concentration of 3 mM for at least 8 h. Diffraction data of both cCP:ONX 0914 and iCP:ONX 0914 crystals were collected to a resolution limit of 2.9 Å (Table 12) and data processing was performed according to section 5.5.3.

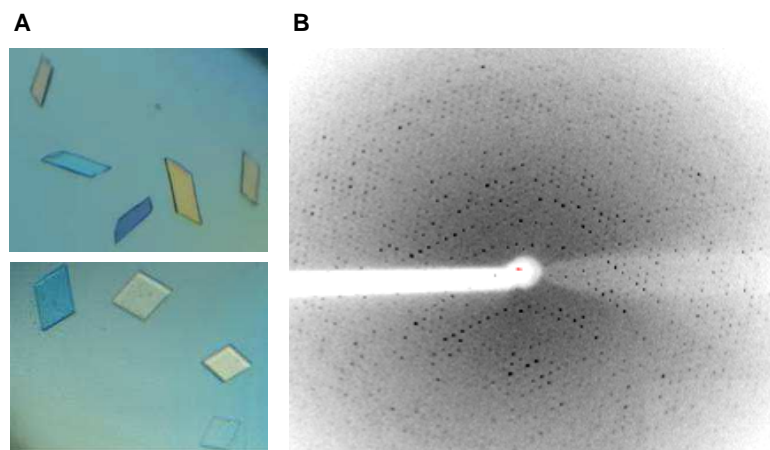


**Figure 10 Analysis of murine cCP and iCP crystals for X-ray diffraction.** (A) Birefringent murine cCP and iCP crystals; (B) Diffraction pattern of an iCP crystal.

The X-ray data revealed for both cCP and iCP crystals space group  $P2_1$ , but different unit cell parameters. Calculation of the Matthews coefficient indicated a solvent content of about 50 %, assuming that the asymmetric unit of iCP crystals contained only one CP, whereas the asymmetric unit of cCP crystals was built up of two 20S proteasomes. The same applied to both ligand complex structures (Table 12). All four crystal structures could be finalized with  $R_{\text{free}}$  values below 27.5 % and root-mean-square deviations for bond lengths and bond angles of less than 0.005 Å and 0.93 °.

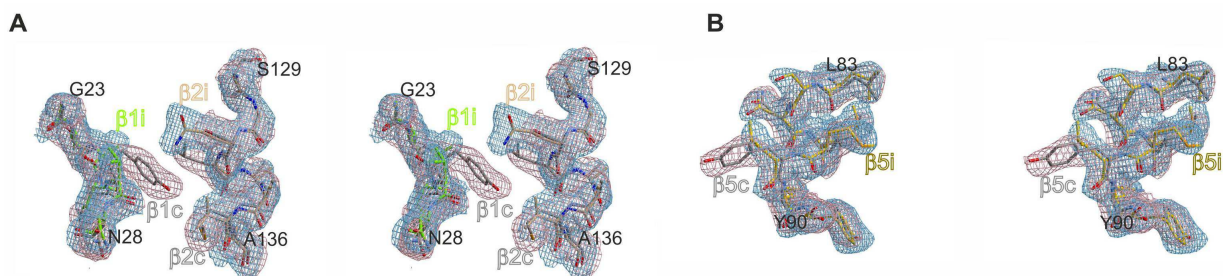


**Figure 11 Stereo representation of the electron density maps of the murine cCP and iCP.** For the calculation of the  $2F_o - F_c$  electron density maps (iCP: blue mesh; cCP: red mesh), which are contoured to  $0.8 \sigma$ , the phases of the displayed amino acids have been omitted. The electron density sections clearly depict explicit differences in the amino acid sequences of c and i subunits: (A) Tyr25 of subunit  $\beta 1c$  corresponds to Ala25 in subunit  $\beta 1i$ ; and Ser131, Leu132 as well as Met135 of subunit  $\beta 2c$  are substituted by Gln, Gly and Val in subunit  $\beta 2i$ , respectively. (B) Tyr88 of subunit  $\beta 5c$  is exchanged for Leu in subunit  $\beta 5i$ .

Adapted from Huber *et al.*, 2012<sup>[32]</sup>.

All proteasome subunits were well defined in the  $2F_o-F_c$  electron density maps and differences in the primary sequences of catalytically active c and i subunits were unambiguously depicted by positive and negative  $F_o-F_c$  maps (Figure 11), indicating that pure iCPs and cCPs have been crystallized. Amino acid residue numbers were allocated according to the sequence alignment to the proteasomal  $\beta$  subunit from *T. acidophilum* (Figure 8).

	<i>m_iCP</i>	<i>m_iCP:ONX 0914</i>	<i>m_cCP</i>	<i>m_cCP:ONX 0914</i>
<b>Crystal parameters</b>				
Space group	P2 <sub>1</sub>	P2 <sub>1</sub>	P2 <sub>1</sub>	P2 <sub>1</sub>
Cell constants	a=118.3 Å b=205.2 Å c=161.9 Å $\beta$ =105.7 °	a=117.3 Å b=194.6 Å c=157.7 Å $\beta$ =107.1 °	a=171.0 Å b=201.3 Å c=226.0 Å $\beta$ =108.1 °	a=171.7 Å b=198.6 Å c=226.8 Å $\beta$ =106.6 °
CPs / AU <sup>a</sup>	1	1	2	2
<b>Data collection</b>				
Beam line	X06DA, SLS	X06DA, SLS	X06SA, SLS	X06SA, SLS
Wavelength (Å)	1.0	1.0	1.0	1.0
Resolution range (Å) <sup>b</sup>	30-3.2 (3.3-3.2)	30-2.9 (3.0-2.9)	30-3.2 (3.3-3.2)	30-2.9 (3.0-2.9)
No. observations	356417	392915	807596	723529
No. unique reflections <sup>c</sup>	121329	145087	235050	308934
Completeness (%) <sup>b</sup>	99.2 (99.4)	97.1 (89.8)	99.5 (99.7)	96.0 (96.7)
R <sub>merge</sub> (%) <sup>b, d</sup>	10.4 (51.5)	11.6 (54.7)	7.6 (59.7)	8.1 (48.1)
I/σ (I) <sup>b</sup>	10.4 (2.3)	8.0 (2.0)	13.9 (2.4)	9.4 (2.0)
<b>Refinement</b>				
<b>(REFMAC5)</b>				
Resolution range (Å)	15-3.2	15-2.9	15-3.2	15-2.9
No. refl. working set	115261	137832	223279	293487
No. refl. test set	5763	6892	11163	14674
No. non hydrogen	48502	48760	97320	97172
No. of ligand atoms	-	294	-	588
Solvent (H <sub>2</sub> O, K <sup>+</sup> , Cl <sup>-</sup> , J)	583	1045	640	1480
R <sub>work</sub> /R <sub>free</sub> (%) <sup>e</sup>	23.9 / 25.4	23.5 / 27.5	22.2 / 24.6	22.9 / 27.2
r.m.s.d. bond (Å) / (°) <sup>f</sup>	0.004 / 0.851	0.005 / 0.926	0.004 / 0.753	0.005 / 0.885
Average B-factor (Å <sup>2</sup> )	79.2	61.7	78.7	67.8
Ramachandran Plot (%) <sup>g</sup>	97.2 / 2.6 / 0.2	96.7 / 3.0 / 0.3	95.4 / 4.1 / 0.5	95.9 / 3.6 / 0.5

**Table 12 X-ray data collection and refinement statistics of murine iCP and cCP structures.**

<sup>a</sup> Asymmetric unit.

<sup>b</sup> The values in parentheses of resolution range, completeness, R<sub>merge</sub> and I/σ (I) correspond to the last resolution shell.

<sup>c</sup> Friedel pairs were treated as identical reflections.

<sup>d</sup>  $R_{\text{merge}}(I) = \frac{\sum_{\text{hkl}} \sum_j |I(\text{hkl})_j - \langle I(\text{hkl}) \rangle|}{\sum_{\text{hkl}} I_{\text{hkl}}}$ , where  $I(\text{hkl})_j$  is the  $j^{\text{th}}$  measurement of the intensity of reflection hkl and  $\langle I(\text{hkl}) \rangle$  is the average intensity.

<sup>e</sup>  $R = \frac{\sum_{\text{hkl}} (|F_{\text{obs}}| - |F_{\text{calc}}|)}{\sum_{\text{hkl}} |F_{\text{obs}}|}$ , where R<sub>free</sub> is calculated for a randomly chosen 5 % of reflections, which were not used for structure refinement, and R<sub>work</sub> is calculated for the remaining reflections.

<sup>f</sup> Deviations from ideal bond lengths/angles.

<sup>g</sup> Number of residues in favoured, allowed or outlier region.

## 6.2.2 Subunit architecture of the cCP and iCP

The overall topologies of the cCP and iCP are identical except for the exchange of the catalytically active c subunits  $\beta 1c$ ,  $\beta 2c$  and  $\beta 5c$  by their i homologues  $\beta 1i$ ,  $\beta 2i$  and  $\beta 5i$ . Likewise the yCP crystal structure, the N-termini of the inactive  $\alpha$  subunits of the cCP and iCP close the entrance to the interior of the CPs. Superposition of the  $\alpha$  rings from cCP, iCP and yCP illustrates their high structural similarity (r.m.s.d.  $C_{\alpha}$  atoms  $\alpha$  ring  $< 0.59$  Å; Figure 12) and suggests that the gate opening mechanism<sup>[16]</sup> is identical for all kind of CPs.

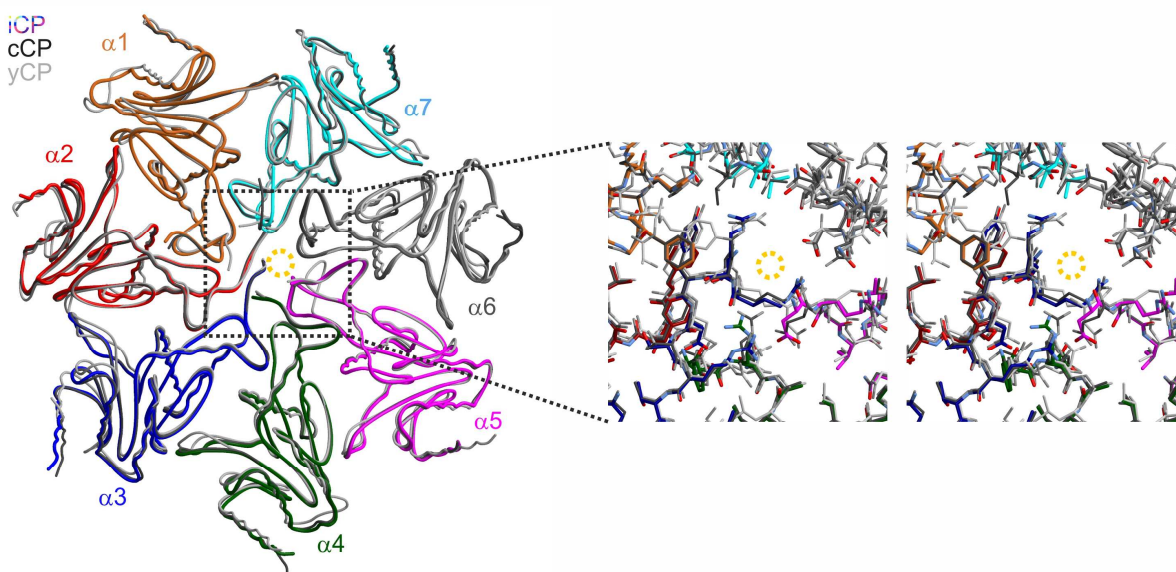


**Figure 12 Structural superposition of the  $\alpha$  ring of yCP, cCP and iCP.** The N-termini of the  $\alpha$  subunits, in particular of  $\alpha 2$ ,  $\alpha 3$  and  $\alpha 4$ , from yCP (grey), cCP (black) and iCP (multi-coloured) prevent access into the proteolytic chamber. A stereoscopic view of the centre of the  $\alpha$  ring (marked by a yellow circle) is provided. Adapted from Huber *et al.*, 2012<sup>[32]</sup>.

Subunits incorporated into both the cCP and iCP, i.e.  $\alpha$  subunits and inactive  $\beta$  subunits are unchanged as proven by an r.m.s.d.  $C_{\alpha}$  atoms of  $< 0.35$  Å for their main chain tracings. Despite differences in their amino acid sequence (Figure 8) the exchangeable  $\beta$  subunits adopt identical folds (r.m.s.d.  $C_{\alpha}$  atoms  $< 0.72$  Å) (Figure 13). Remarkably, also the C-terminal loop of the subunits  $y\beta 2$  and  $\beta 2c$ , which embraces its neighbouring subunit  $\beta 3$  and which is essential for CP assembly<sup>[108]</sup>, is structurally conserved in subunit  $\beta 2i$ .

The majority of the amino acid exchanges between the proteolytically active c and i subunits are located on the subunit surfaces and only a minority is conserved among species ( $\beta 1i$ : 13.6 %,  $\beta 2i$ : 5.1 %,  $\beta 5i$ : 9.8 %). As revealed by PISA analysis, the number of interaction sites between adjacent subunits of the cCP and the iCP differ (Table 15), but the impact on the stability or half-life of the CPs cannot be predicted from the structural data. However, the

subunit interaction surfaces of the proteolytically active subunits and their adjacent neighbours enable the formation of mixed proteasome species, which were previously suggested to be physiologically relevant<sup>[29-30]</sup>.

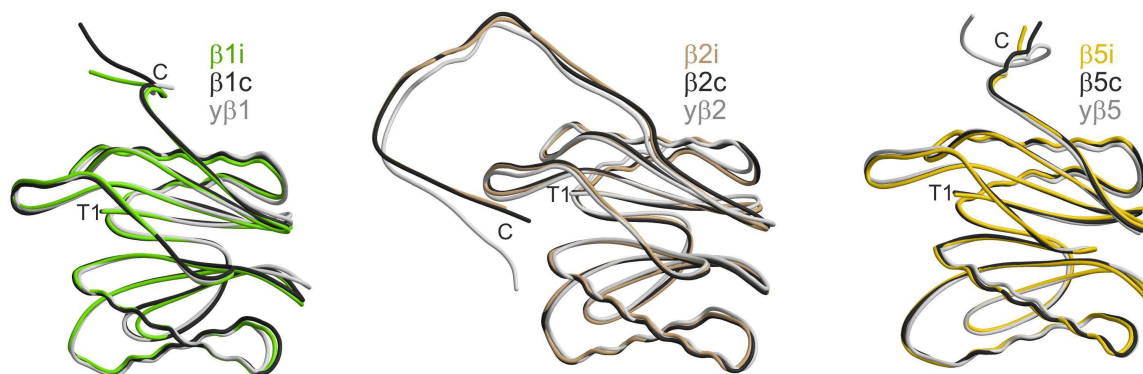


**Figure 13 Main chain tracings of the proteolytically active proteasome subunits.** The C<sub>α</sub> backbones of the subunits β1i (green), β2i (brown) and β5i (yellow) are superimposed to their constitutive counterparts from mouse (black) and yeast (grey). The nucleophilic N-terminal Thr1 and the C-terminus are indicated. Adapted from Huber *et al.*, 2012<sup>[32]</sup>.

### 6.2.3 Structural analysis of the substrate binding channels

The substrate and inhibitor specificities of the proteasomal active sites are predominantly determined by the enthalpic interactions of ligands with defined pockets of the primed and unprimed substrate binding channels surrounding the nucleophilic Thr1. The following section summarizes the similarities and alterations in the primed and unprimed sites of proteolytically active c and i subunits.

The primed substrate binding pockets (S') of the subunits β2i and β2c differ by several amino acid exchanges. However, their impact on protein hydrolysis remains enigmatic. In the primed site of subunit β1i one amino acid is deleted in the loop segment 113 to 124 compared to subunit β1c. This loop shortening is a hallmark of all β1i subunit sequences known to date and might affect substrate preferences. Comparison of the primed pockets in the subunits β5c and β5i depicts the amino acid substitutions S115D and E116N. Although these changes might influence substrate affinities, they are not conserved between species. Using X-ray crystallography most inhibitory compounds have been shown to target the unprimed substrate binding channels<sup>[22, 109]</sup> and thus, the S1, S2 and S3 pockets are far better examined than the primed ones. The unprimed sites of the subunits β2c and β2i display high similarity to each other, except for the conserved substitutions T48V and D53E. While T48V might alter the specificity for P2 residues, D53E is assumed to change neither the chemical environment nor

substrate preference (Figure 14). Interestingly, Glu53 and Thr48 are also characteristic of the yeast subunit  $\beta 2$  (Figure 8).

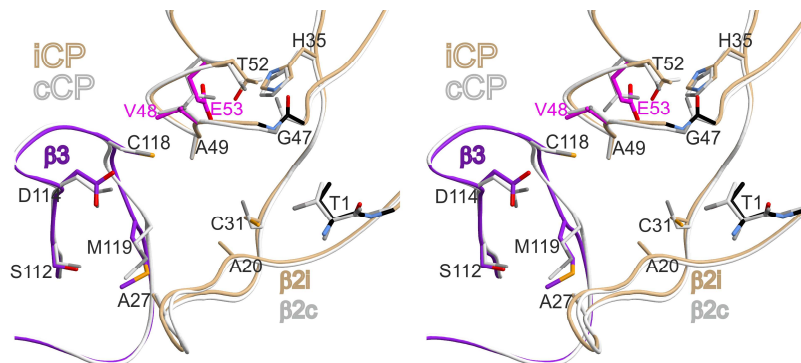


**Figure 14 Superposition of the unprimed  $\beta 2c$  and  $\beta 2i$  substrate binding channels (Stereo view).** Amino acid numbers are given for subunit  $\beta 2i$  and residues characteristic of  $\beta 2i$  are highlighted in magenta. Adapted from Huber *et al.*, 2012<sup>[32]</sup>.

By contrast, the  $\beta 1c$  and  $\beta 1i$  subunits strongly differ in their amino acid lining in the unprimed substrate binding channel. The polar active site surrounding of subunit  $\beta 1c$  is replaced by a more hydrophobic one in subunit  $\beta 1i$ . In particular the amino acid substitutions T20V, T31F, R45L and T52A decrease the polarity and the size of the  $\beta 1i$  S1 pocket (Figure 15). Hence, the  $\beta 1i$  active site preferentially cleaves proteins C-terminally of small hydrophobic and branched amino acids such as Leu, Ile or Val and significantly enhances the production of high-affinity MHC I ligands. The structural features of subunit  $\beta 1i$  are in full agreement with the reported  $\beta 1i$ -selective fluorogenic substrate Ac-Pro-Ala-Leu-AMC<sup>[110]</sup>. In addition to the changes in the S1 pocket, the S3 pocket is characterized by the amino acid substitutions T22A ( $\beta 1i$ ) and A27V ( $\beta 1i$ ) as well as Y114H in the neighbouring subunit  $\beta 2i$ . These differences lead to a more size-restricted and more polar S3 pocket in the iCP (Figure 15).

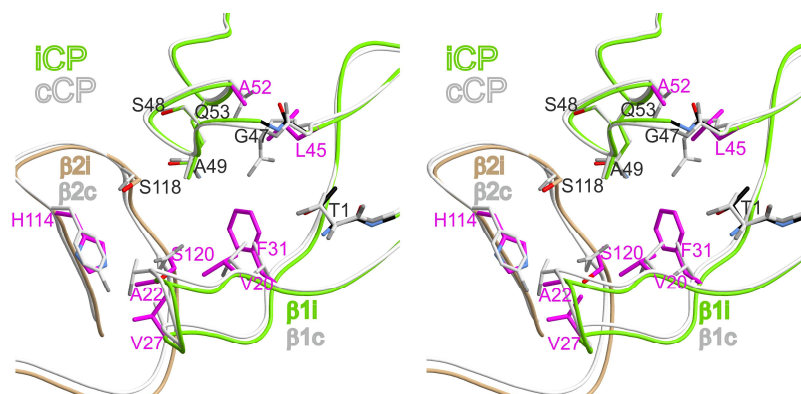


**Figure 15 Superposition of the unprimed  $\beta 1c$  and  $\beta 1i$  substrate binding channels (Stereo view).** Amino acid numbers are given for subunit  $\beta 1i$  and residues characteristic of  $\beta 1i$  are highlighted in magenta. Adapted from Huber *et al.*, 2012<sup>[32]</sup>.

The hydrophobic amino acid lining of the S1 pocket in subunit  $\beta 5c$  is preserved in subunit  $\beta 5i$  with respect to the amino acids Ala20, Met45, Ala49 and Cys52 (Figure 16). The amino acid side chain 31 is also hydrophobic but variable in length (e.g. Met in mice and Val in humans). Thus, both subunits exert overlapping substrate specificities and hydrolyse proteins after apolar residues. Interestingly, all known  $\beta 5i$  subunits possess a shallow S2 pocket formed by either Cys48 or Ser48 (Figure 16). The incorporation of Ser27 in the S3 pockets of murine and human  $\beta 5i$  subunits reduces their size but concomitantly increases their polarity.

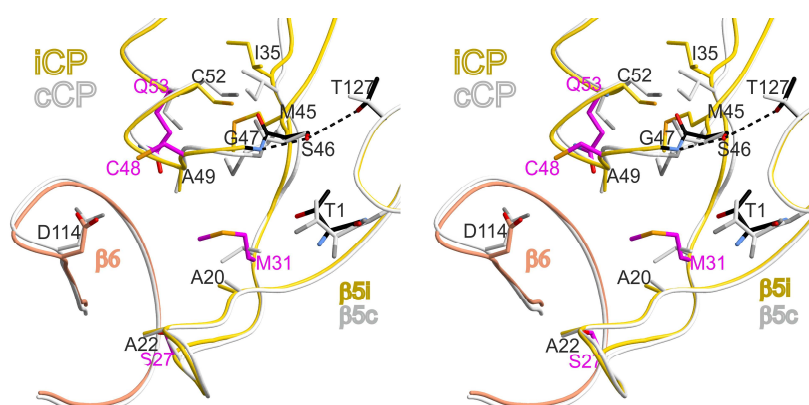


**Figure 16 Superposition of the unprimed  $\beta 5c$  and  $\beta 5i$  substrate binding channels (Stereo view).** Amino acid numbers are given for subunit  $\beta 5i$  and residues characteristic of the  $\beta 5i$  substrate binding pockets are highlighted in magenta. Being hydrogen-bridged to the oxyanion hole Gly47NH and to Thr127 (black dashed lines), Ser46 is supposed to influence the catalytic activity of subunit  $\beta 5i$ . Note that the side chain conformations of Ile35 and Met45 vary in the subunits  $\beta 5c$  and  $\beta 5i$ . Adapted from Huber *et al.*, 2012<sup>[32]</sup>.

A striking feature of the  $\beta 5i$  subunit is the increased size of its S1 pocket compared to subunit  $\beta 5c$ . This is mostly due to distinct conformations of Met45 and Ile35 in subunit  $\beta 5i$  as well as a shift of the protein backbone including the residues 36 to 76 compared to subunit  $\beta 5c$  (Figure 16). In this regard, the amino acid exchange S53Q between subunit  $\beta 5c$  and  $\beta 5i$  might have a pivotal function. In subunit  $\beta 5i$  the aliphatic part of the Gln53 side chain can stabilize Met45, while in subunit  $\beta 5c$  Ser53 cannot provide these favourable interactions and thus, the S1 pocket is significantly smaller than that of its *i* counterpart (see also section 6.4.1). The differently-sized S1 pockets are supposed to give rise to varying substrate specificities. Although both subunits  $\beta 5c$  and  $\beta 5i$  accommodate hydrophobic amino acids in their S1 pockets, the  $\beta 5i$  subunit prefers more spacious ones than subunit  $\beta 5c$ <sup>[110]</sup> (see also chapter 6.3.3).

Moreover, the active site Thr1 of subunit  $\beta 5i$  is surrounded by a unique hydrophilicity that results from the amino acid exchanges A46S and V127T and that is not observed in any other proteasome subunit. Ser46O<sup>γ</sup> is in hydrogen bonding distance to T127O<sup>γ</sup> and the oxyanion

hole Gly47NH (distances 2.9-3.4 Å; Figure 16). This unique hydrogen bond network might stabilize the tetrahedral transition state during catalysis. Additionally, it could kinetically favour the  $\beta 5i$  active site, as the increased polar environment is supposed to attract water molecules and thereby to enhance peptide bond hydrolysis<sup>[32]</sup>.

### 6.3 Investigations on the $\beta 5i$ -selective proteasome inhibitor ONX 0914

#### 6.3.1 Inhibition of 20S proteasomes by ONX 0914

The  $\alpha',\beta'$ -epoxyketone inhibitor ONX 0914 has been shown to selectively inhibit the  $\beta 5i$  subunit of the murine and human iCP and to be therapeutically active in inflammatory disorders and autoimmune diseases<sup>[37, 53]</sup>. To verify these results and to further assess the purities of the murine cCP and iCP preparations,  $IC_{50}$  values of ONX 0914 were determined for the ChTL activity of the yCP, the murine cCP and iCP as well as the human cCP and iCP (Figure 17). The activities of CPs were measured in the presence of varying concentrations of ONX 0914, using the fluorogenic substrate Suc-Leu-Leu-Val-Tyr-AMC. In agreement with previous studies, the  $\beta 5c$  subunits from mouse and human cCPs were far less inhibited than their i counterparts (Figure 17). Interestingly, however, ONX 0914 slightly favoured subunit y $\beta 5$  over  $\beta 5c$ .

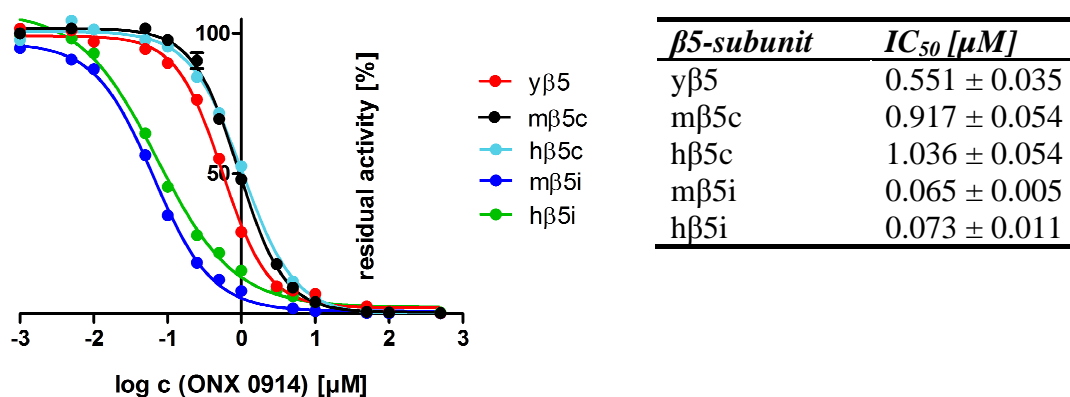


**Figure 17 Selectivity of ONX 0914 for the  $\beta 5i$  subunit of the iCP.** After the exposure of yCP, cCP and iCP to varying concentrations of ONX 0914 (0.001-500  $\mu M$ ) the residual ChTL activity was determined. Data from three experiments were normalized to DMSO treated controls and averaged. Standard deviations are indicated.  $IC_{50}$  values were deduced from fitted data. Adapted from Huber *et al.*, 2012<sup>[32]</sup>.

#### 6.3.2 Proteasome core particles in complex with ONX 0914

Structural explanations for the  $\beta 5i$  selectivity of ONX 0914 could only be unravelled by analysing and comparing ligand binding to each active site of the cCP/yCP and iCP. Inhibitor soaking experiments with a final concentration of ONX 0914 of 3 mM blocked all proteolytic centres – not only the preferred subunit  $\beta 5i$ .  $2F_O-F_C$  electron density maps depicted that ONX 0914 was covalently bound to all active sites of cCP, iCP and yCP (Figure 18) and additionally proved that these were catalytically active in the crystals. Despite suggestions

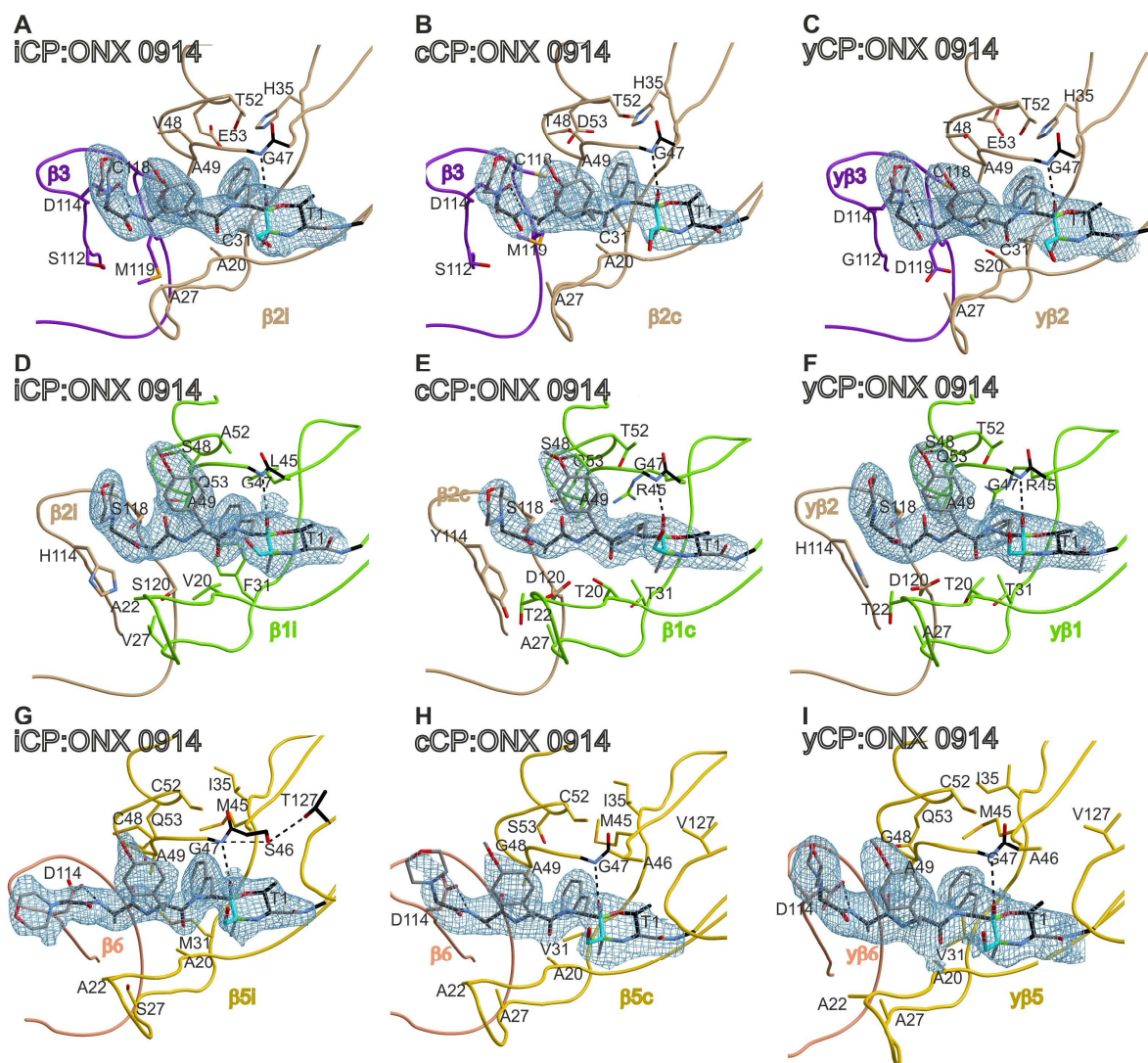


**Figure 18** ONX 0914 bound to the proteolytically active sites of yCP, cCP and iCP. The  $2F_o - F_c$  electron density maps, contoured to  $1\sigma$ , show full occupancy for ONX 0914 at all active centres of yCP, cCP and iCP. ONX 0914 and residue Thr1 have been omitted for phasing. Hydrogen bonds are marked by black dashed lines. Adapted from Huber *et al.*, 2012<sup>[32]</sup>.

that subunit  $\beta 7$  might also exert hydrolytic activity in the ligand-free bovine cCP crystal structure<sup>[21a]</sup>, ONX 0914 was not bound to this subunit.

Likewise other peptidic CP inhibitors, the C-terminal dipeptide of ONX 0914 forms an antiparallel  $\beta$  sheet in the unprimed substrate binding channels of all active sites and is well stabilized by favourable interactions with the surrounding protein residues. In contrast, the N-terminal morpholine moiety of ONX 0914 is not engaged in any contact with the substrate binding channels and thus, can adopt different conformations. Unique to all  $\beta 2$  and  $\beta 5$  subunits is the additional stabilization of ONX 0914 via a hydrogen bond between its N-terminal peptide bond and Asp114 from the neighbouring subunits  $\beta 3$  and  $\beta 6$ , respectively. Furthermore, structural comparison of all ONX 0914 molecules bound to the yCP, cCP and iCP proves a similar mechanism of inhibitor binding for all active sites (Figure 19).

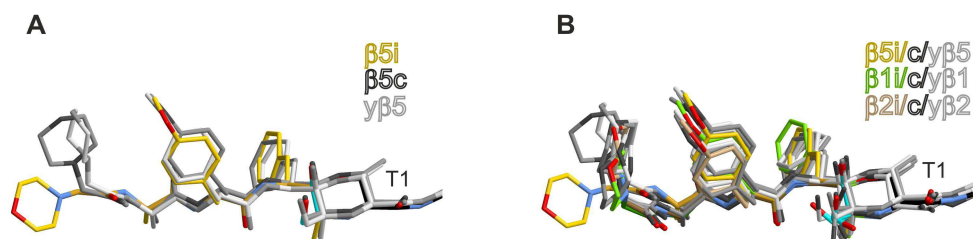


**Figure 19 Superposition of ONX 0914 molecules bound to the yCP, cCP and iCP.** (A) The binding mechanism of ONX 0914 to Thr1 is identical for all  $\beta 5$  active sites and (B) for all proteasome subunits. The peptidic ligand adopts an anti-parallel  $\beta$  sheet in each substrate binding channel, thereby mimicking natural protein substrates.

### 6.3.3 Molecular basis for the subunit selectivity of ONX 0914

Comparison of active proteasome subunits in the presence and absence of ONX 0914 visualized the structural features that cause the observed  $\beta 5i$  selectivity of this compound. Owing to Ala20, Ala27, Cys31 and Gly45 the  $\beta 2$  subunits possess large S1 pockets that can easily accommodate ONX 0914 without any structural changes (Figure 20A-C).

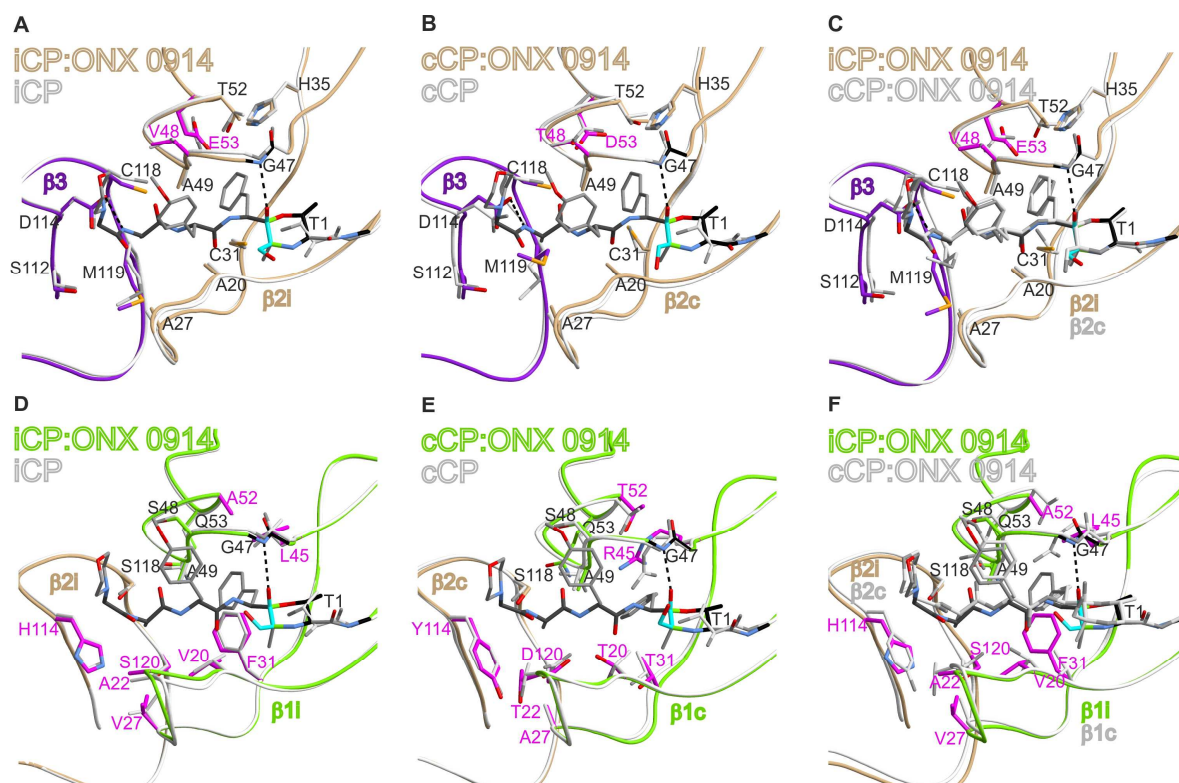


**Figure 20 Superposition of ligand-free and ligand-bound active sites of the proteasome.** The unliganded subunits  $\beta 2i$  (A),  $\beta 2c$  (B),  $\beta 1i$  (D) and  $\beta 1c$  (E) are superimposed to their ONX 0914 bound states. The panels (C) and (F) illustrate the differences for the ligand-bound  $\beta 2c/i$  and  $\beta 1c/i$  subunits, respectively; amino acid numbers are given for the i subunit. Residues characteristic of the i or c subunits are highlighted in magenta. Hydrogen bonds are indicated by black dashed lines. Adapted from Huber *et al.*, 2012<sup>[32]</sup>.

However, as the protein surrounding provides only few stabilizing interactions, ligand binding to the  $\beta 2c$  and  $\beta 2i$  active sites is energetically disadvantaged compared to subunit  $\beta 5i$ .

By contrast, binding of ONX 0914 triggers structural rearrangements in subunit  $\beta 1c$ . Due to steric hindrance with the ligand's phenylgroup in P1, Arg45 has to change its conformation (Figure 20E). Moreover, the polarity of the S1 pocket disfavours the binding of the hydrophobic P1 side chain of ONX 0914 to subunit  $\beta 1c$  and causes electrostatic repulsion.

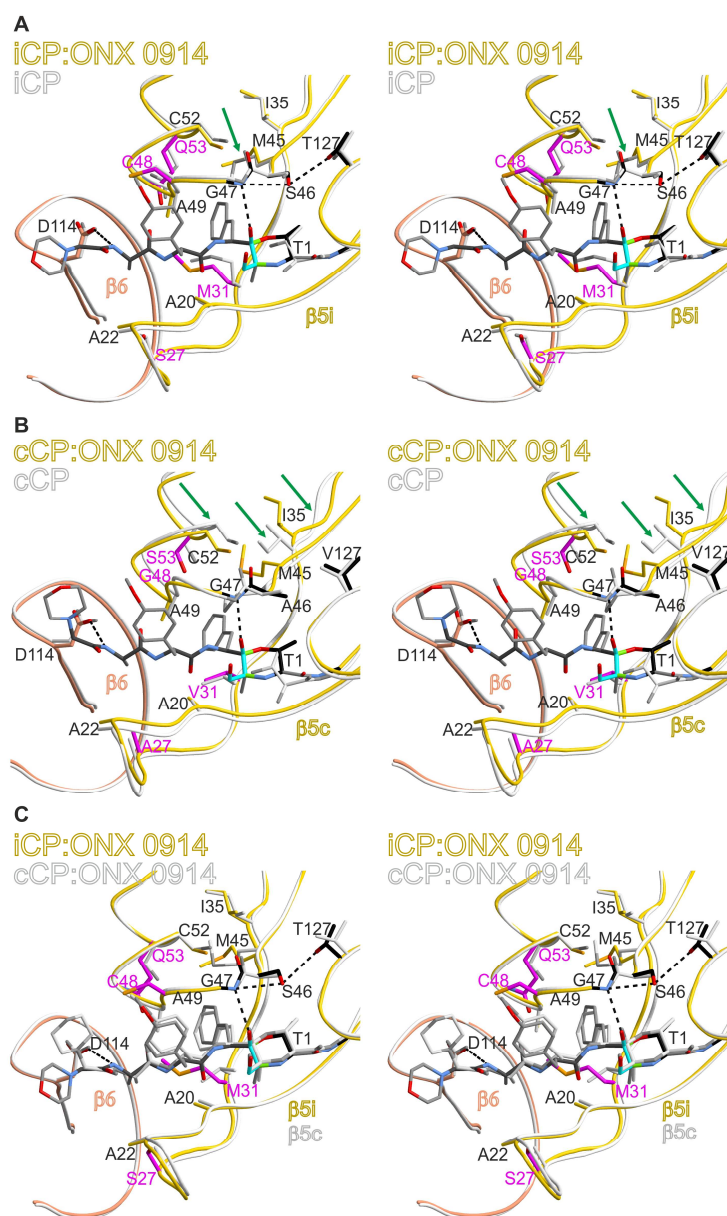


**Figure 21 Binding of ONX 0914 to the  $\beta 5c$  and  $\beta 5i$  subunits of the cCP and iCP (Stereo view).** (A) The unprimed substrate binding channel of subunit  $\beta 5i$  is ideally suited to accommodate ligands with bulky P1 side chains such as ONX 0914. Upon binding neighbouring protein residues only slightly rearrange (green arrow). (B) Docking of ONX 0914 to subunit  $\beta 5c$  triggers major structural changes around the active site as marked by green arrows. (C) The  $\beta 5c$  and  $\beta 5i$  subunits in their ligand bound states are structurally similar to each other. Adapted from Huber *et al.*, 2012<sup>[32]</sup>.

Therefore the hydrophobic substrate binding channel of the  $\beta 1i$  active site should be ideally suited for docking of ONX 0914. Yet, the ligand complex structure indicates that Phe31 sterically hinders binding of ONX 0914 to Thr1 (Figure 20D, F). The distance between the phenyl group of Phe31 and the P1 phenylalanine of ONX 0914 is only 3.4-3.5 Å and Phe31 adopts an energetically disfavoured orientation towards the carbonyl oxygen of Asp32 (distance 3.2 Å). Thus, the atomic distances reflect the repelling forces that prevent high-affinity binding of ONX 0914 to subunit  $\beta 1i$ .

Ligand binding to the  $\beta 5i$  subunit triggers slight conformational adaptations of Met31 and the CH<sub>3</sub>-S-group of Met45 (r.m.s.d. C <sub>$\alpha$</sub>   $\beta 5i/\beta 5i$ :ONX 0914: 0.28 Å; Figure 21A). By contrast, the comparison of the unprimed substrate binding channel of subunit  $\beta 5c$  in the presence and absence of ONX 0914 reveals profound differences. Binding of the bulky P1 phenylalanine of the  $\alpha',\beta'$  epoxyketone to the S1 pocket displaces Met45 from its normal position. Furthermore, the side chain of Ile35 is flipped and the  $\beta$  sheets S4 and S5 as well as  $\alpha$  helix H1 are offset by

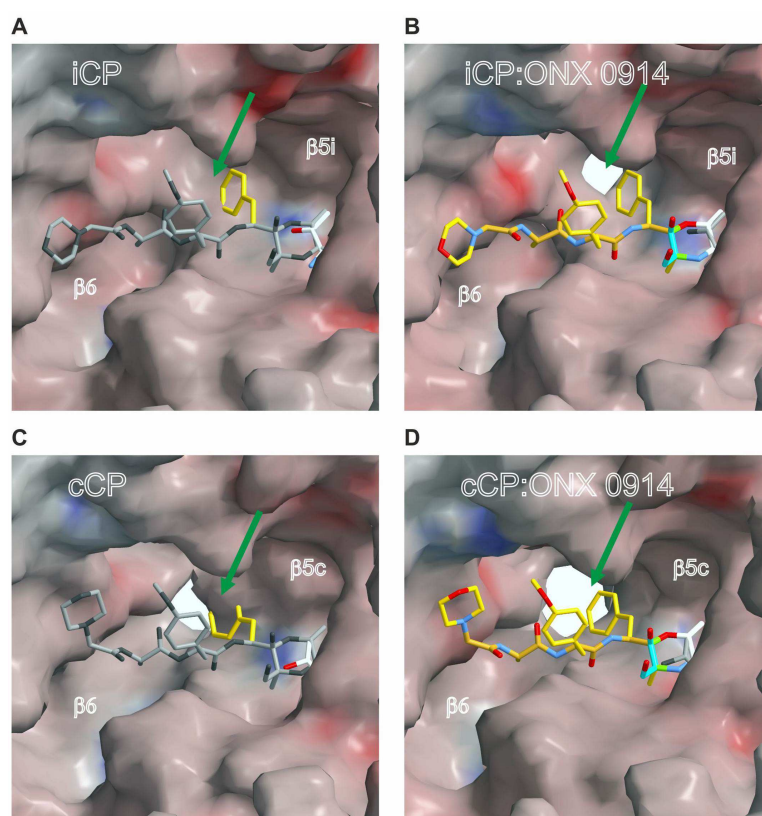


**Figure 22 Conolly surface representations of the unprimed  $\beta 5c$  and  $\beta 5i$  substrate binding channels in the presence and absence of ONX 0914.** Surface charge distributions are shown for the subunits  $\beta 5i$  (A),  $\beta 5i$ :ONX 0914 (B),  $\beta 5c$  (C) and  $\beta 5c$ :ONX 0914 (D) with positive and negative electrostatic potentials contoured from 50 kT/e (intense blue) to -50 kT/e (intense red). In the panels (A) and (C) ONX 0914 has been modelled into the active site by superposition with the panels (B) and (D), respectively. The catalytic Thr1 is coloured in white. ONX 0914 is shown in yellow, modelled molecules of ONX 0914 in grey – except for the P1 site. To depict ligand-protein clashes and resulting structural changes (green arrows) the amino acids 46-50 of the subunits  $\beta 5c$  and  $\beta 5i$  were removed. Adapted from Huber *et al.*, 2012<sup>[32]</sup>.

up to 1.7 Å (r.m.s.d.  $C_{\alpha}$   $\beta 5c/\beta 5c:ONX\ 0914$ : 0.64 Å; Figure 21B). Remarkably, the ligand bound states of the subunits  $\beta 5c$  and  $\beta 5i$  are similar to each other (r.m.s.d  $C_{\alpha}$   $\beta 5c:ONX\ 0914/\beta 5i:ONX\ 0914$ : 0.55 Å; Figure 21C) and the  $\beta 5c:ONX\ 0914$  structure highly resembles the apostructure of subunit  $\beta 5i$ . These results indicate that inhibition of  $\beta 5c$  by ONX 0914 is sterically impaired by Met45. The enthalpic energy required to achieve the observed structural changes is mirrored in the high  $IC_{50}$  value of ONX 0914 towards  $\beta 5c$  compared to  $\beta 5i$  and its lower affinity. Conolly surface representations of the subunits  $\beta 5c$  and  $\beta 5i$  clearly depict the structural differences in their S1 pocket architecture. Whereas subunit  $\beta 5i$  possesses a spacious S1 site, which enables the binding of bulky P1 residues (Figure 22A) with only minor side chain rearrangements (Figure 22B), the S1 pocket forming residues of subunit  $\beta 5c$  severely clash with bulky P1 groups (Figure 22C) and thereby cause enormous structural reorientations (Figure 22D). Hence, the substrate specificity of subunit  $\beta 5i$  can be described as a ChTL activity, whereas the  $\beta 5c$  active site preferentially exerts elastase-like or Snaap activity<sup>[33b]</sup>.

### 6.3.4 Structural analysis of the epoxyketone reaction mechanism

Whereas boronic acid inhibitors are known to inhibit serine and threonine proteases<sup>[68]</sup>,  $\alpha',\beta'$  epoxyketones exclusively react with the small family of Ntn hydrolases to which the proteasome belongs. This high degree of specificity for the CP results from the unique bivalent reaction mechanism of  $\alpha',\beta'$  epoxyketones, which has been elucidated for the natural product epoxomicin isolated from actinomycetes<sup>[61a]</sup>: The nucleophilic Thr1O <sup>$\gamma$</sup>  of the active proteasome subunit attacks the carbonyl carbon atom of the  $\alpha',\beta'$  epoxyketone, thereby

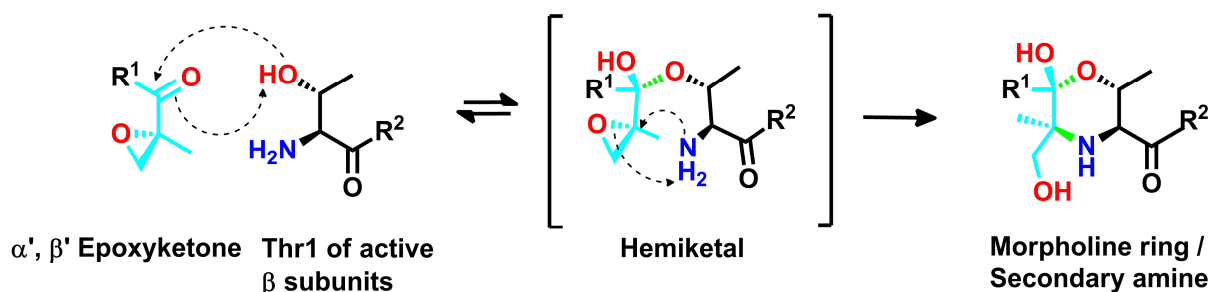


**Figure 23 Schematic illustration of the reaction mechanism of epoxyketone inhibitors.** Thr1O <sup>$\gamma$</sup>  nucleophilically attacks the carbonyl carbon atom of the epoxyketone inhibitor. The formed hemiketal intermediate can either dissociate to deliberate Thr1O <sup>$\gamma$</sup>  or irreversibly cycle under the formation of a secondary amine (morpholine ring system) involving Thr1N. Bonds created by this reaction are coloured in green,  $R_1$  corresponds to the peptide moiety of the compound,  $R_2$  to the proteolytically active  $\beta$  subunit, whose Thr1 is covalently modified by the displayed reaction mechanism.

	<i>yCP:ONX 0914_ep</i>	<i>yCP:ONX 0914_mo</i>
<b>Crystal parameters</b>		
Space group	P2 <sub>1</sub>	P2 <sub>1</sub>
Cell constants	a=135.4 Å b=300.4 Å c=143.9 Å β=112.8 °	a=134.4 Å b=300.8 Å c=143.8 Å β=112.8 °
CPs / AU <sup>a</sup>	1	1
<b>Data collection</b>		
Beam line	X06SA, SLS	X06SA, SLS
Wavelength (Å)	1.0	1.0
Resolution range (Å) <sup>b</sup>	30-2.7 (2.8-2.7)	30-3.4 (3.5-3.4)
No. observations	1211656	443424
No. unique reflections <sup>c</sup>	286910	141633
Completeness (%) <sup>b</sup>	99.1 (98.7)	98.1 (98.3)
R <sub>merge</sub> (%) <sup>b, d</sup>	9.8 (59.6)	14.3 (59.6)
I/σ (I) <sup>b</sup>	11.3 (2.7)	8.2 (2.2)
<b>Refinement (REFMAC5)</b>		
Resolution range (Å)	15-2.7	15-3.4
No. refl. working set	272564	134550
No. refl. test set	13628	6727
No. non hydrogen	50924	51122
No. of ligand atoms	36	294
Water molecules	1340	1322
R <sub>work</sub> /R <sub>free</sub> (%) <sup>e</sup>	22.3 / 24.3	17.9 / 22.0
r.m.s.d. bond (Å) / (°) <sup>f</sup>	0.005 / 0.834	0.005 / 0.899
Average B-factor (Å <sup>2</sup> )	54.6	80.5
Ramachandran Plot (%) <sup>g</sup>	97.3 / 2.4 / 0.3	96.3 / 3.2 / 0.5

**Table 13 X-ray data collection and refinement statistics of yCP structures in complex with ONX 0914.**

<sup>a</sup> Asymmetric unit.

<sup>b</sup> The values in parentheses of resolution range, completeness, R<sub>merge</sub> and I/σ (I) correspond to the last resolution shell.

<sup>c</sup> Friedel pairs were treated as identical reflections.

<sup>d</sup>  $R_{\text{merge}}(I) = \frac{\sum_{\text{hkl}} \sum_j | [I(\text{hkl})_j - \langle I(\text{hkl}) \rangle] |}{\sum_{\text{hkl}} I_{\text{hkl}}}$ , where  $I(\text{hkl})_j$  is the  $j^{\text{th}}$  measurement of the intensity of reflection hkl and  $\langle I(\text{hkl}) \rangle$  is the average intensity.

<sup>e</sup>  $R = \frac{\sum_{\text{hkl}} | |F_{\text{obs}}| - |F_{\text{calc}}| |}{\sum_{\text{hkl}} |F_{\text{obs}}|}$ , where R<sub>free</sub> is calculated for a randomly chosen 5 % of reflections, which were not used for structure refinement, and R<sub>work</sub> is calculated for the remaining reflections.

<sup>f</sup> Deviations from ideal bond lengths/angles.

<sup>g</sup> Number of residues in favoured, allowed or outlier region.

forming a reversible hemiketal. Subsequently, the free N-terminus of Thr1 opens the epoxide ring and, by an irreversible cyclisation, creates a morpholine ring system (Figure 23). This mode of action and the docking mechanism of ONX 0914 was investigated in detail by ONX 0914:yCP complex structures. The yCP can be used as a model system due to its structural similarity to the cCP, including the orientation of Met45 (Figure 26A). yCP crystals were therefore soaked with ONX 0914 in different concentrations for varying time periods. Hereby, the reaction intermediate – the hemiketal with an intact epoxide (ep) – and the reaction product – the morpholine ring (mo) – could be trapped in a crystal structure (Table

13). These data clarified that indeed Thr1N attacks the epoxide once the hemiketal is formed, and proved the formerly proposed mode of action of epoxyketone inhibitors<sup>[61a]</sup>.

Whereas all three proteolytically active sites were covalently modified in the yCP:ONX 0914\_mo structure, only subunit y $\beta$ 5 visualized the hemiketal formation of ONX 0914 (Figure 24A). In agreement with data on the murine and human cCP<sup>[37]</sup>, ONX 0914 favours subunit y $\beta$ 5 over y $\beta$ 1 and y $\beta$ 2.

Notably, the 2F<sub>O</sub>-F<sub>C</sub> electron density map for the yCP:ONX 0914\_mo structure displayed the whole inhibitor with its P1, P2 and P3 residues as well as the N-terminal morpholine ring and the covalent linkage to Thr1 (Figure 24B). In contrast, the electron density map for the hemiketal intermediate (yCP:ONX 0914\_ep) surprisingly depicted solely the intact epoxide ring and the ligand's P1 site (Figure 24A). As the N-terminal P3 and P2 sites of ONX 0914\_ep were not defined, they were not yet bound to their respective substrate specificity pockets and thus, flexible. This finding provides evidence that first the electrophilic warhead and the P1 residue of covalently acting inhibitors contact the active site

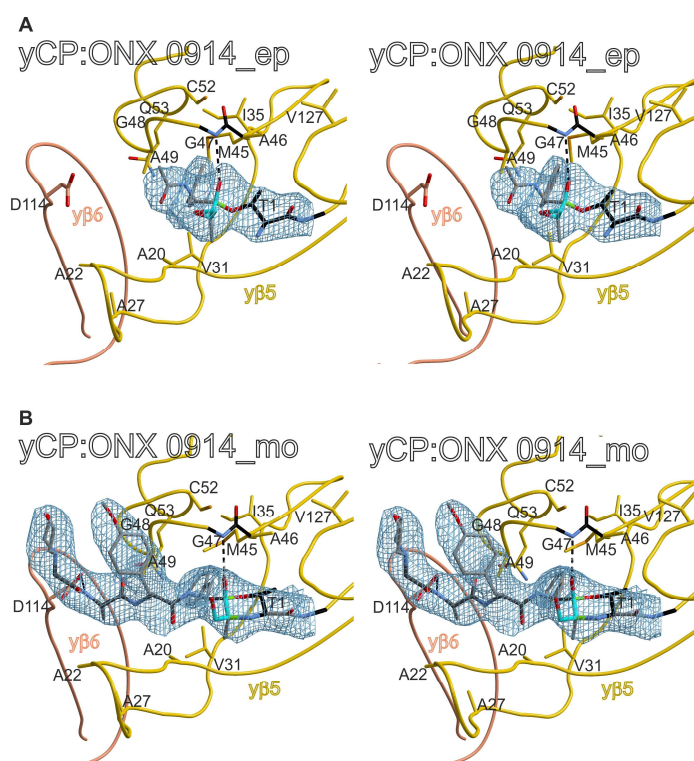


**Figure 24 Stereo view of the yeast 20S proteasome subunit  $\beta$ 5 (y $\beta$ 5) in complex with ONX 0914.** Subunit y $\beta$ 5 is coloured in yellow and the neighbouring subunit y $\beta$ 6 in orange. Thr1 and the oxyanion hole Gly47NH are marked in black; and hydrogen bonds are indicated by black dashed lines. ONX 0914 is shown in grey with its reactive head group highlighted in cyan. The experimental 2F<sub>O</sub>-F<sub>C</sub> omit electron density map (blue mask) is contoured to 1 $\sigma$ . (A) Hemiketal formation of ONX 0914 with Thr1 of subunit y $\beta$ 5. Note, only the epoxide and the P1 site of ONX 914 are well-defined in the electron density map. (B) Subunit y $\beta$ 5 in complex with the completely reacted ONX 0914. All inhibitor side chains (P1, P2 and P3) are visualized in the electron density. Adapted from Huber *et al.*, 2012<sup>[32]</sup>.

Thr1 and the S1 pocket and that only upon completing the reaction mechanism interactions with the S2 and S3 sites form the antiparallel  $\beta$  sheet in the substrate binding channel. In conclusion, even though all substrate binding pockets contribute to the  $IC_{50}$  value of a compound, the P1 side chain of a compound, apart from its electrophilic pharmacophore, is mostly responsible for its affinity for the active site. In this regard the depicted size differences of the  $\beta 5c$  and  $\beta 5i$  S1 pockets provoke the enhanced affinity of ONX 0914 for subunit  $\beta 5i$ .

Structural comparison of the hemiketal intermediate and the final reaction product reveals that although the P1 residue of the ONX 0914\_ep is defined in the electron density map, it initially does not fully occupy the S1 pocket of subunit  $y\beta 5$  (Figure 25). Hence, during the reversible hemiketal formation no sterical clashes with Met45 occur and in agreement with the X-ray structure of the intermediate state no displacement of Met45 is observed (Figure 24A). Only the formation of the morpholine ring system with Thr1 properly positions the P1 side chain of ONX 0914 in the S1 specificity site and triggers the reorientation of Met45 as well as further structural changes (Figure 24B). With respect to the distinct affinities of ONX 0914 for the subunits  $\beta 5c$  and  $\beta 5i$ , the following model for ONX 0914 binding to cCP and iCP  $\beta 5$  subunits is proposed: In both active sites  $\beta 5i$  and  $\beta 5c$  hemiketal formation of ONX 0914 with Thr1O<sup>y</sup> is possible without any sterical hindrance. However, whereas the P1 side chain of ONX 0914 can immediately adopt its final position in the S1 pocket of subunit  $\beta 5i$  and thereby form the morpholine ring system as well as the antiparallel  $\beta$  sheet, this is not possible in subunit  $\beta 5c$ . Met45 of subunit  $\beta 5c$  sterically hampers full binding of the P1 residue to the S1 pocket and has to be dislocated to enable covalent modification of Thr1. Consequently, the energy barrier for the morpholine ring formation in subunit  $\beta 5c$  is higher and the back-reaction leading to a restored and catalytically active Thr1 in subunit  $\beta 5c$  is more likely than in  $\beta 5i$ . Thus, the increased probability of ONX 0914 to modify the Thr1 of subunit  $\beta 5i$  compared to  $\beta 5c$  provides the explanation for its lower  $IC_{50}$  value and its selectivity for subunit  $\beta 5i$ .

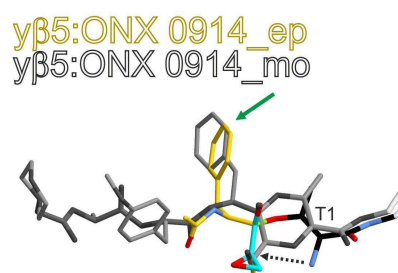


**Figure 25 Docking of ONX 0914 to the active site Thr1.** Structural superposition of ONX 0914 in its epoxide (ep; yellow) and morpholine (mo; grey) state bound to Thr1 of subunit  $y\beta 5$ . The green arrow indicates that the positions of the P1 side chain differ in the reaction intermediate and the reaction product; the black dashed arrow marks the position where the free N-terminus of  $y\beta 5$  attacks the epoxide to form a morpholine ring system. Adapted from Huber *et al.*, 2012<sup>[32]</sup>.

## 6.4 Yeast mutagenesis studies on the subunits $\beta 5c$ , $\beta 5i$ and $\beta 5t$

The crystal structures of the murine cCP and iCP demonstrated that the proteasomal  $\beta$  subunits are structurally conserved from archaea to mammals. Based on the overall identical folds and similar main chain tracings of  $\beta 5$  subunits (Figure 26), the yCP can be used as a model system for analysing the functional impact of single amino acid exchanges between the cCP, iCP as well as tCP by mutagenesis.

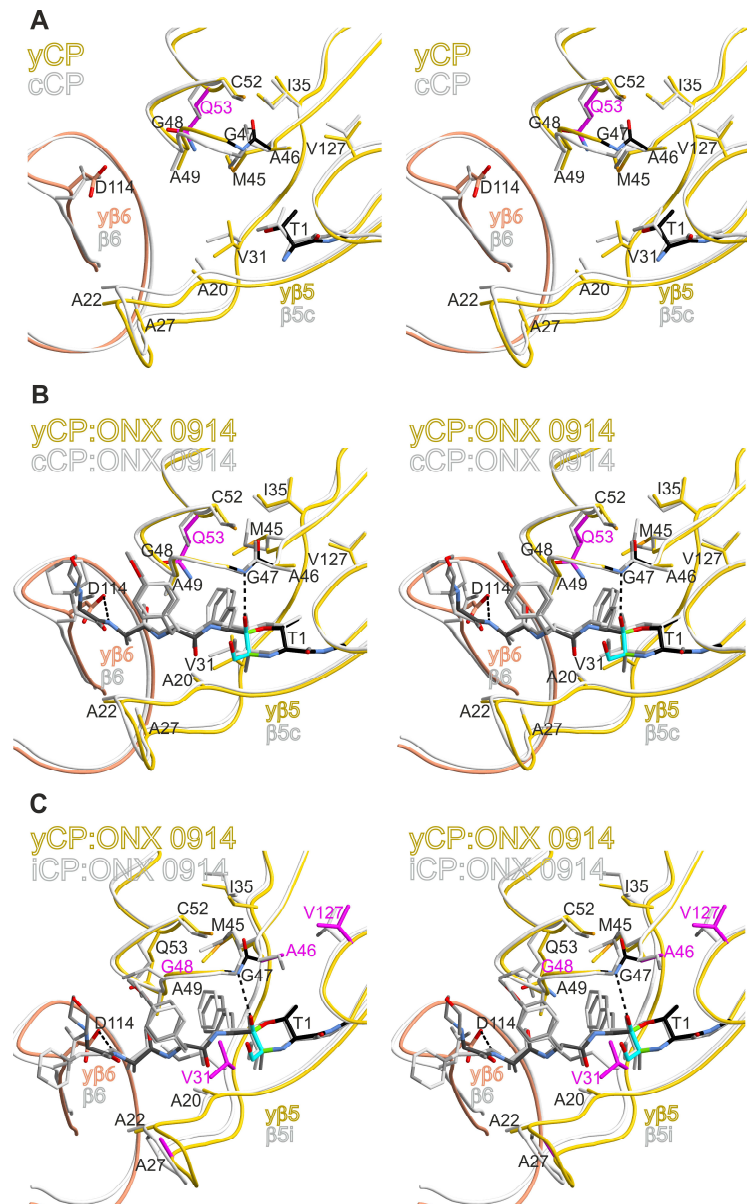


**Figure 26 Structural comparison of the yeast subunit  $y\beta 5$  and the murine active sites  $\beta 5c$  and  $\beta 5i$  of cCP and iCP, respectively (stereo view).** (A) Superposition of the subunits  $y\beta 5$  and  $\beta 5c$  in their ligand-free states and (B) their ligand-bound states depict the structural similarity of both. Panel (C) additionally illustrates the comparison of the ONX 0914 bound active sites  $y\beta 5$  and  $\beta 5i$ . Amino acids are numbered for the yCP. Residues that are characteristic of the yCP subunit  $y\beta 5$  are coloured in magenta. Gly47 and Thr1 are shown in black. The ligand is highlighted in grey. Hydrogen bonds are indicated by black dashed lines. Adapted from Huber *et al.*, 2012<sup>[32]</sup>.

### 6.4.1 Mimicking the $\beta 5c$ active site

The cCP and iCP crystal structures depicted that the orientation of Met45 is crucial for the size of the S1 specificity pocket in  $\beta 5$  subunits (Figure 16; Figure 21). While favourable van der Waals interactions of Met45 with Gln53 contribute to the formation of a large S1 site in subunit  $\beta 5i$ , Ser53 cannot stabilize Met45 in subunit  $\beta 5c$  (Figure 16) and causes a diminished S1 pocket in subunit  $\beta 5c$ . This model is supported by the strong conservation of Ser53 in  $\beta 5c$  subunits, Gln53 in  $\beta 5i$  entities and Ala53 in  $\beta 5t$  active sites<sup>[32]</sup>. Notably, the yeast  $y\beta 5$  subunit incorporates Lys32, a hallmark of  $\beta 5c$  entities, as well as the  $\beta 5i$  characteristic residue Gln53, leading to a similar S1 pocket architecture like in  $\beta 5c$ . Hence, subunit  $y\beta 5$  appears to represent a chimera of the  $\beta 5c$  and  $\beta 5i$  active sites at least with respect to the amino acids 32 and 53. Indeed, the  $IC_{50}$  value of ONX 0914 for subunit  $y\beta 5$  was determined to  $\sim 0.5 \mu M$ , while it was  $\sim 1 \mu M$  for  $\beta 5c$  and  $\sim 0.07 \mu M$  for  $\beta 5i$  (Figure 17).

The importance of Gln53 for the S1 pocket architecture in the subunits  $y\beta 5$  and  $\beta 5i$  was proven by mutation of Gln53 to Ser in the  $y\beta 5$  active site. The  $IC_{50}$  values of ONX 0914 and bortezomib for the created mutant CP were  $1.32 \mu M$  and  $0.15 \mu M$ , respectively (Figure 27). Remarkably, compared to the wt  $yCP$ , ONX 0914 was three-times less potent towards the  $y\beta 5$  Q53S mutant, while bortezomib displayed an increased affinity (Figure 27). These findings elucidate that Ser53 enhances binding of ligands with smaller P1 side chains such as Leu (bortezomib) over inhibitors with bulky residues like Phe (ONX 0914). Wt  $y\beta 5$  shows only slight preference for bortezomib, but the mutation Q53S significantly increases the selectivity for this compound (Figure 27). In agreement, subunit  $\beta 5c$  was reported to be far more susceptible to inhibition by bortezomib ( $IC_{50}$ :  $7 \text{ nM}$ <sup>[74]</sup>) than ONX 0914 ( $IC_{50}$ :  $236\text{-}1000 \text{ nM}$  depending on the method<sup>[32, 37]</sup>). For structural analysis of the Q53S mutant X-ray

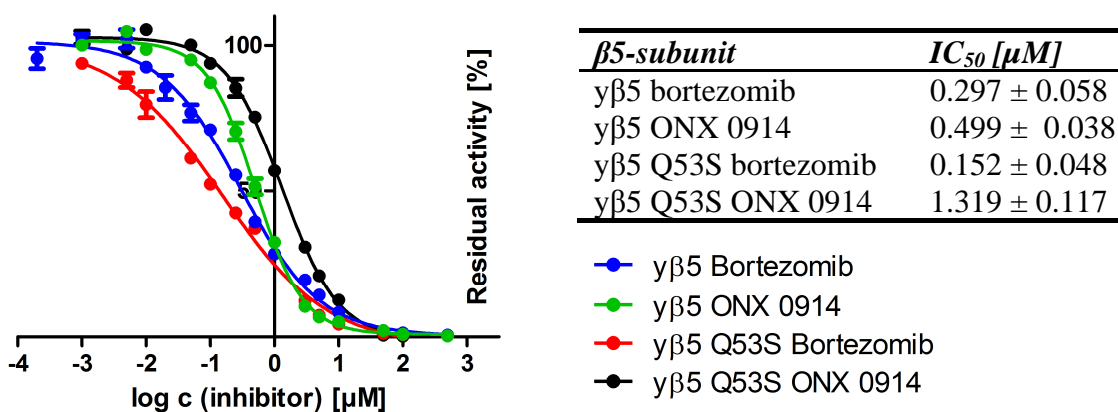


**Figure 27 Inhibition of wt and mutant  $yCP$ s by ONX 0914 and bortezomib.** Residual proteolytic activities were measured in triplicate upon exposure to different inhibitor concentrations with the fluorogenic substrate Suc-Leu-Leu-Val-Tyr-AMC and normalized to a DMSO treated control.  $IC_{50}$  values were deduced from fitted data.

data were collected in the presence and the absence of both ligands (Table 16). The mutant  $\gamma\beta 5$  subunit Q53S displays high structural identity to its wt counterpart (r.m.s.d.  $C_\alpha$   $\gamma\beta 5/\gamma\beta 5Q53S$ : 0.2 Å; Figure 28A) and binding of bortezomib and ONX 0914 induces structural changes similar to  $\gamma\beta 5$  and  $\beta 5c$  (r.m.s.d.  $C_\alpha$   $\gamma\beta 5Q53S/\gamma\beta 5Q53S$ :ONX 0914: 0.76 Å; r.m.s.d.  $C_\alpha$   $\gamma\beta 5Q53S/\gamma\beta 5Q53S$ : bortezomib: 0.62 Å; Figure 28B, C, F). However, ONX 0914 leads to a more severe displacement of the sulphur atom of Met45 than bortezomib (Figure 28D), hereby explaining the reduced affinity of ONX 0914 for subunit  $\gamma\beta 5Q53S$  compared to bortezomib (Figure 27). Removal of Gln53 leads to an insufficient stabilization of Met45 in the ligand-bound state and hence, more energy is required for bulky P1 side chains to reorient Met45 and to keep distance to it. The propensity of Met45 to adopt its normal conformation is likely to hinder particularly spacious ligands such as ONX 0914 from binding irreversibly to Thr1. In conclusion, although the substitution Q53S causes no obvious structural differences and amino acid 53 is not directly involved in ligand binding, its side chain length yet significantly affects the affinity of ligands.

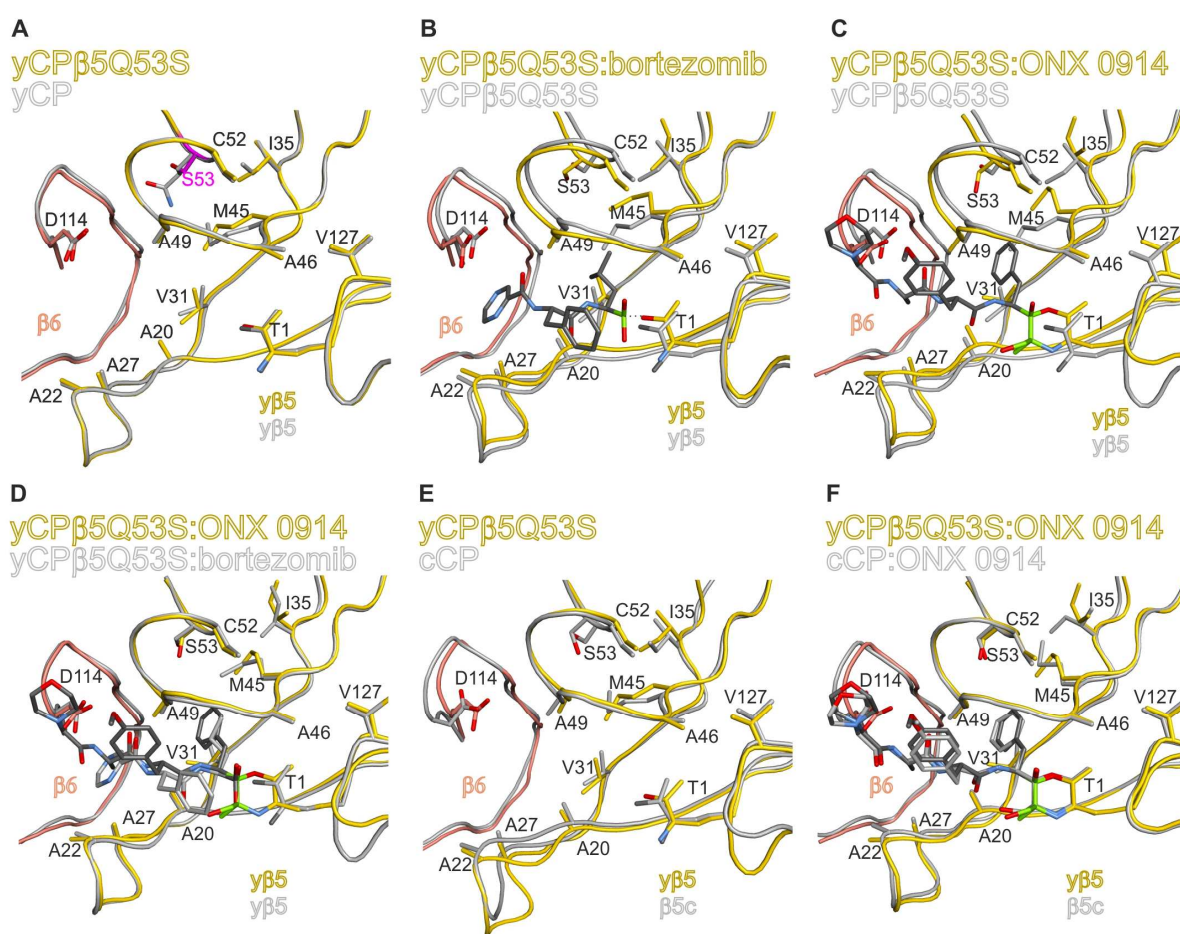


**Figure 28 Structural analysis of the yCP  $\beta 5$  mutant Q53S.** (A-D) Superposition of (un-)liganded wt and mutant yeast  $\beta 5$  active sites; (E, F) Comparison of the yCP  $\beta 5$  mutant Q53S with the murine cCP. Amino acid numbers are given for the yCP  $\beta 5$  mutant Q53S; sequence differences between superimposed structures are highlighted in magenta; the electrophilic head groups of inhibitory compounds (grey) are coloured in green.

### 6.4.2 Analysis of the $\beta 5i$ substrate binding channel

The comparison of the crystal structures of cCP and iCP suggests that van der Waals interactions of Met45 with the aliphatic side chain of Gln53 in subunit  $\beta 5i$  promote the formation of a spacious S1 pocket (Figure 16). Although subunit  $\gamma\beta 5$  harbours a Gln53, Met45 adopts a conformation similar to subunit  $\beta 5c$ . This observation provoked the question of which additional amino acids in proximity to the active site contribute to the distinct conformations of Met45.

To identify key residues that lead to the differently sized S1 pocket in the  $\beta 5i$  substrate binding channel, numerous point mutations were introduced in subunit  $\gamma\beta 5$ . The following amino acid exchanges aimed at mimicking the murine (or human)  $\beta 5i$  subunit: A27S, (V31M,) K32N, A46S, G48C, T57R, K71G and V127T (Figure 8; Table 3).

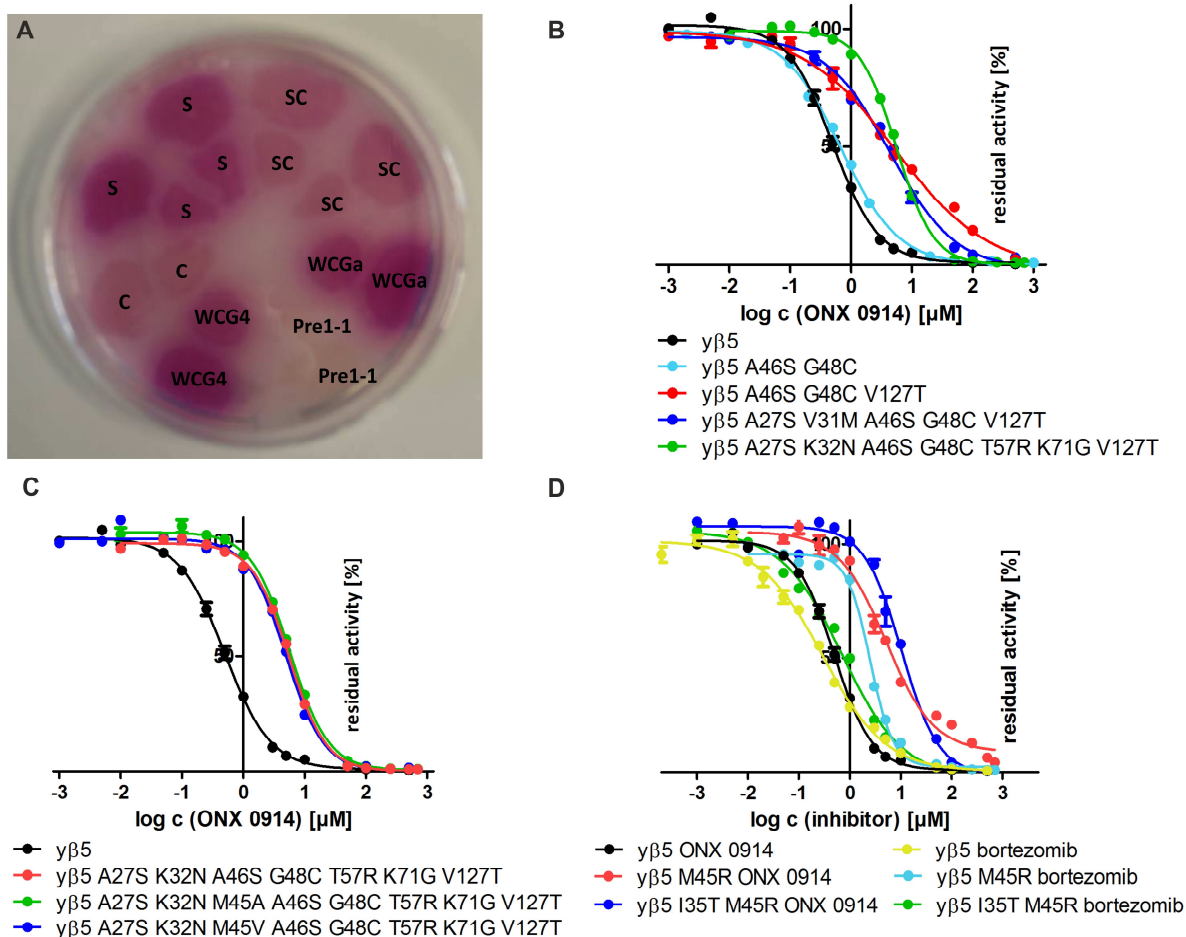


**Figure 29** Activity and inhibition assays of mutant and wt yCPs. (A) Overlay test for the ChTL activity of yCPs using the chromogenic substrate Cbz-Gly-Gly-Leu-pNA. Tested mutants are termed according to Table 3. The yeast strains WCG4a and WCG4a *pre1-1* served as positive and negative controls, respectively. (B-D) The indicated mutant CPs that aimed at imitating the iCP subunit  $\beta 5i$  were tested in triplicate for their inhibition by ONX 0914 and bortezomib with the fluorogenic substrate Suc-Leu-Leu-Val-Tyr-AMC. The deduced  $\text{IC}_{50}$  values are given in Table 14.

Remarkably, most mutant yeast strains suffer from a significant growth phenotype, which is probably caused by an impaired  $\beta 5$  activity, as observed in a proteolysis assay with the chromogenic substrate Cbz-Gly-Gly-Leu-pNA (Figure 29A). Hereby, the single point mutation G48C sufficed to markedly attenuate the ChTL activity. Cys48 might restrict the flexibility of the loop segment 46-49 and thereby hamper substrate and inhibitor binding. While the exchange A46S alone did not affect CP activity and its combination with G48C had only minor effects on the  $IC_{50}$  value of ONX 0914, additional introduction of Thr127 strongly impaired ligand binding (Table 14). The hydrogen bond between Ser46 and Thr127 that has also been observed for the iCP structure additionally enhances the rigidity of the loop region 46-49 and thereby might constrict ligand binding. Intriguingly, mutagenesis of additional residues (A27S, K32N, V31M, T57R, K71G) had neither further influence on the affinity of ONX 0914 for the  $\gamma\beta 5$  active site (Figure 29B) and nor did it lead to the reorientation of Met45 as observed in the unliganded subunit  $\beta 5i$  (Figure 30E; Table 17).

<i><math>\beta 5</math>-subunit</i>	<i>Inhibitor</i>	<i><math>IC_{50}</math> [<math>\mu M</math>]</i>
$\gamma\beta 5$	bortezomib	$0.297 \pm 0.058$
$\gamma\beta 5$	ONX 0914	$0.499 \pm 0.038$
$\gamma\beta 5$ SC	ONX 0914	$0.673 \pm 0.055$
$\gamma\beta 5$ SCT	ONX 0914	$5.379 \pm 1.839$
$\gamma\beta 5$ SMSCT	ONX 0914	$4.416 \pm 0.771$
$\gamma\beta 5$ SNSCRGT	bortezomib	$1.807 \pm 0.168$
$\gamma\beta 5$ SNSCRGT	ONX 0914	$5.580 \pm 0.307$
$\gamma\beta 5$ SNASCRGT	bortezomib	$3.078 \pm 0.402$
$\gamma\beta 5$ SNASCRGT	ONX 0914	$5.706 \pm 0.321$
$\gamma\beta 5$ SNVSCRGT	bortezomib	$2.606 \pm 0.266$
$\gamma\beta 5$ SNVSCRGT	ONX 0914	$4.911 \pm 0.409$
$\gamma\beta 5$ R	bortezomib	$2.508 \pm 0.178$
$\gamma\beta 5$ R	ONX 0914	$5.185 \pm 1.097$
$\gamma\beta 5$ TR	bortezomib	$0.706 \pm 0.115$
$\gamma\beta 5$ TR	ONX 0914	$10.37 \pm 2.134$

**Table 14**  $IC_{50}$  values for  $\gamma$ CP mutants that partially mimic either the primary sequence or the structural features of the iCP subunit  $\beta 5i$ . Mutants are termed according to Table 3.

Hence, the key features of subunit  $\beta 5i$  could so far not be reconstituted in yeast, even though all amino acids in the active site surrounding were identical to the murine/human subunit  $\beta 5i$  (Figure 30E). Consequently, rather the structural differences than the primary sequences of the  $\beta 5i$  and  $\beta 5c/\gamma\beta 5$  substrate binding channels are responsible for the selectivity of ONX 0914. In order to mimic the enlarged S1 pocket of subunit  $\beta 5i$ , Met45 was substituted by either alanine or valine, but intriguingly these mutant CPs exhibited only poor affinity for both ONX 0914 and bortezomib (Table 14). Probably in the absence of a

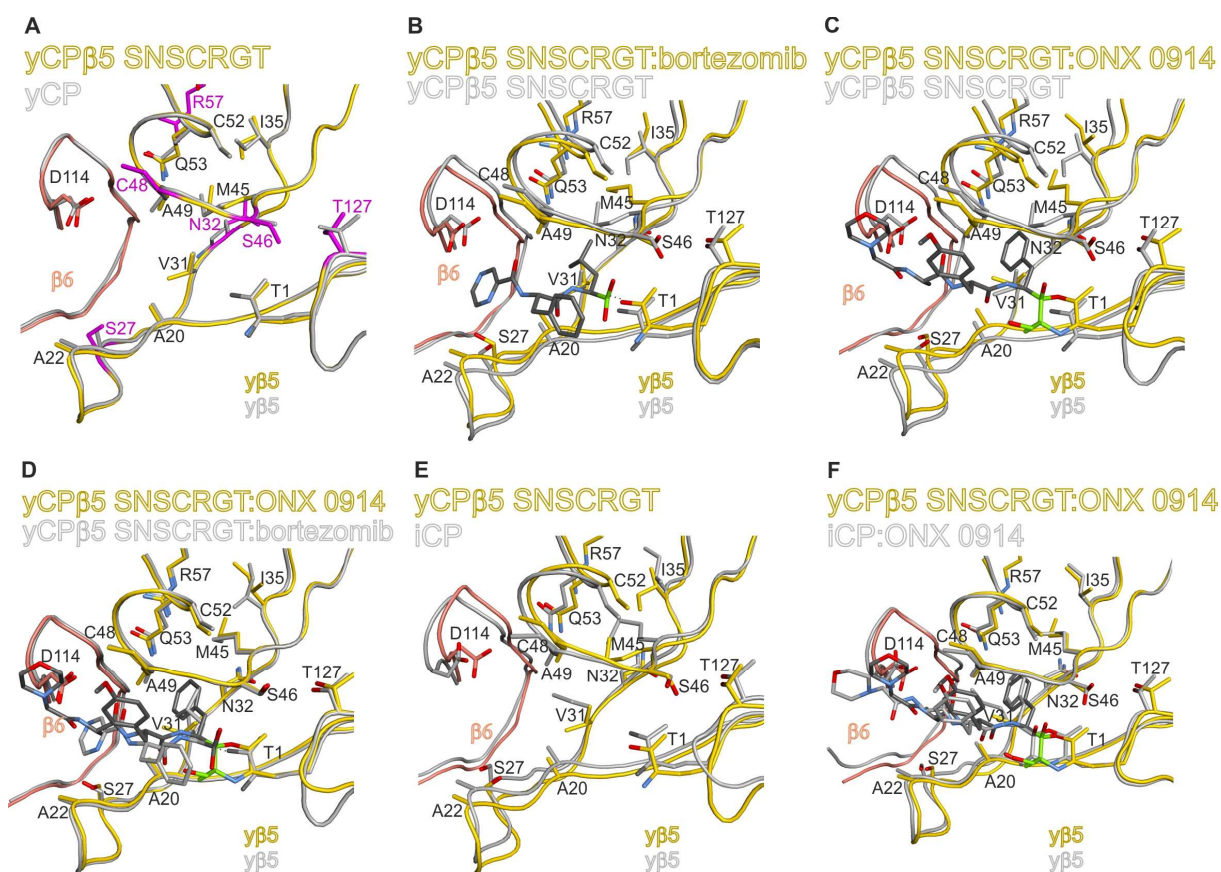


**Figure 30 Crystal structure analysis of  $\beta 5i$  mimicking yCPs.** Mutant  $y\beta 5$  substrate binding channels are superimposed onto wt  $\beta 5$  active sites of wt yCP and iCP to depict structural similarities and differences. Amino acid labellings are indicated for mutant CPs; amino acid mutations are highlighted in magenta and the electrophilic headgroups of inhibitors are shown in green.

prolonged linear aliphatic side chain such as Met45 ligands cannot be sufficiently stabilized in the S1 pocket. These results are also in line with reports on the bortezomib resistance conferring character of Val45<sup>[72c]</sup> and are indicative of the highly sophisticated architecture of the proteasome.

Concomitantly, structural characterization of the  $y\beta 5$  mutants M45R and I35T M45R that were previously analysed<sup>[84]</sup> and that are unrelated to the iCP revealed an interesting feature. The amino acid exchange M45R reduces the ChTL activity by electrostatic repulsion of apolar amino acids by Arg45, but by the additional mutation I35T the ChTL activity is regained. Ligand complex structures of the mutant M45R with bortezomib and ONX 0914 visualized that only binding of the  $\alpha',\beta'$ -epoxyketone causes major structural changes of Arg45 (r.m.s.d.  $C_{\alpha}$   $y\beta 5M45R/y\beta 5M45R:ONX$  0914: 0.82 Å; r.m.s.d.  $C_{\alpha}$   $y\beta 5M45R/y\beta 5M45R:bortezomib$ : 0.43 Å; Figure 31B, C; Table 18). Hence, the poor affinity of ONX 0914 is presumably caused by steric hindrance and the opposing polarity in the S1 pocket, while binding of bortezomib appears to be solely hampered by electrostatic repulsion.

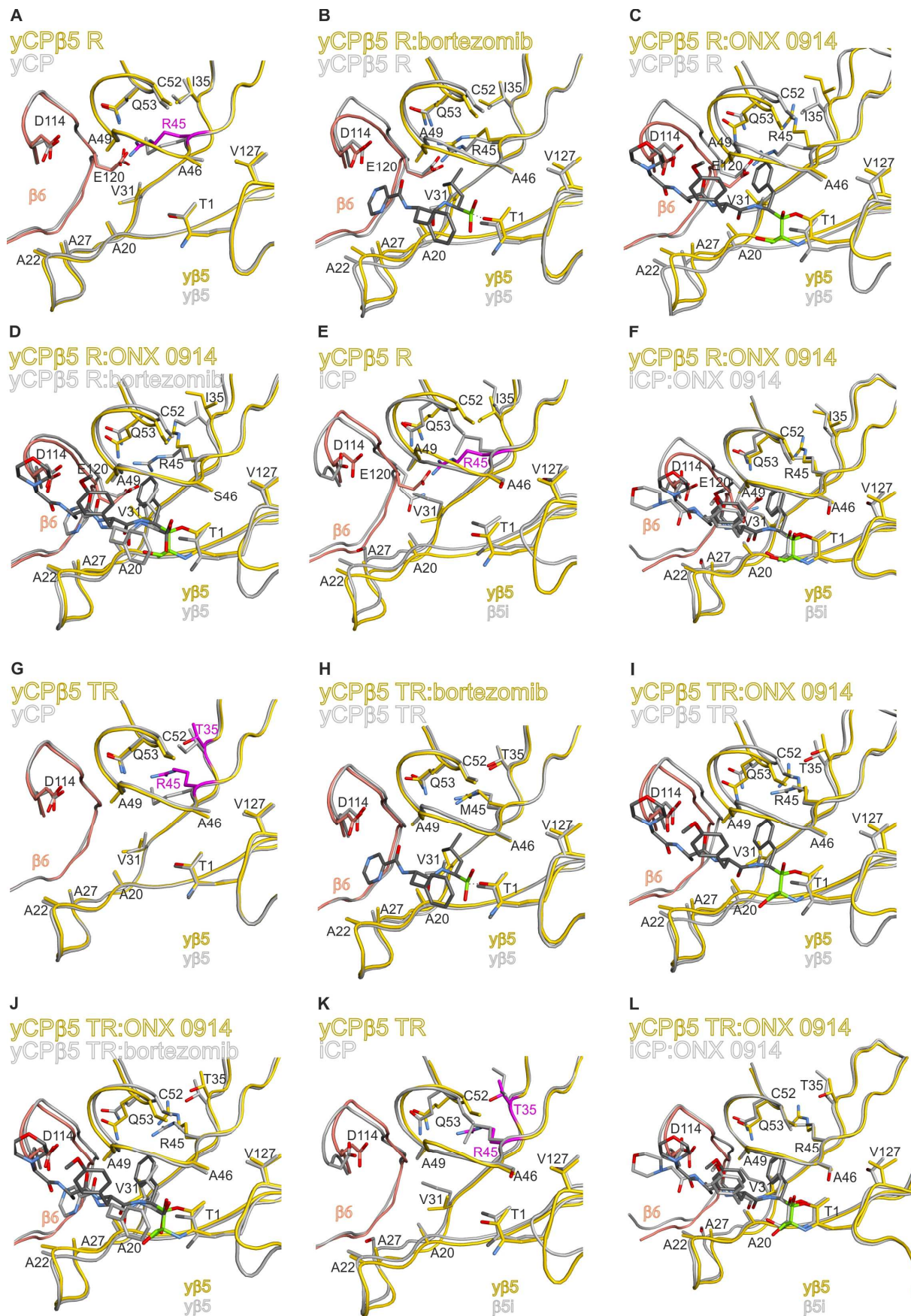


**Figure 31** Crystal structures of mutant CPs. Mutant yβ5 substrate binding channels are superimposed onto β5 active sites of wt yCP and iCP to depict structural similarities and differences in the presence and absence of inhibitor. Amino acid residues of mutant CPs are labelled; amino acid mutations are highlighted in magenta and the electrophilic headgroups of inhibitors are shown in green.

Interestingly, the restored ChTL activity of the double mutant relies on a strong hydrogen bond (2.8 Å) between Thr350<sup>γ</sup> and Arg45N<sup>ε</sup> that rearranges Arg45 and enlarges the size of the S1 pocket similar to β5i (Figure 31G, K). Due to the spacious S1 site the double mutant displayed a 3.5 times enhanced affinity for bortezomib compared to the yβ5M45R mutant (Table 14) and the ligand does not induce any structural rearrangement (r.m.s.d. C<sub>α</sub> yβ5TR/yβ5TR:bortezomib: 0.35 Å; Figure 31H; Table 19). This finding proves that indeed the size of the S1 pocket affects the inhibitory potency of compounds. Still, the mutant yCP I35T M45R is dramatically less susceptible to ONX 0914 than the wt yCP (Table 14), because accommodation of its bulky phenyl side chain is electrostatically hindered by the guanidine group of Arg45 (Figure 31I). As confirmed by crystallographic analysis ligand binding pushes Arg45 1 Å further away from the phenylgroup of ONX 0914, thereby significantly enlarging its distance to Arg45 up to 5 Å (r.m.s.d. C<sub>α</sub> yβ5TR/yβ5TR:ONX 0914: 0.69 Å; Figure 31I). A similar distance of 4.8-5.2 Å is observed for Arg45 and the P1 leucine of bortezomib bound to the yCP I35T M45R mutant (Figure 31H). In conclusion, the strongly reduced affinity of ONX 0914 for the double mutant discloses the enormous effects of electrostatic repulsion on ligand binding (see also section 6.4.3) and highlights the perfect suitability of the Met side chain for establishing a ChTL activity.

### 6.4.3 Probing subunit β5t

The thymoproteasome incorporates the tCP-specific subunit β5t that – unlike the β5c and β5i active sites – harbours a more hydrophilic substrate binding channel<sup>[21c]</sup>. In particular the amino acid residues Ser20, Ser31, Thr45, Thr48 and Ser49 (Figure 8) enhance the polarity of the unprimed S1 and S2 pockets and favour cleavage C-terminally of charged residues. In contrast, the S3 pocket is lined with the hydrophobic residues Cys22 and Ala27. Similarly to subunit β5i, Ser46 might increase the polarity around the active site Thr1 and the oxyanion hole (see also section 6.2.3). Val127, however, is not suited to form a hydrogen bond network with Ser46 like it is observed for subunit β5i.

Due to limited biological samples no structural information on the tCP is available so far. Therefore, this study aimed at mimicking the β5t active site in yeast by mutagenesis. A stepwise approach was used to introduce the mutations A20S, A22C, V31S, M45T, A46S and G48T into subunit yβ5 (Table 3). Most of the created mutants were characterized by a reduced growth rate and displayed a dramatically decreased ChTL activity of the yβ5 subunit

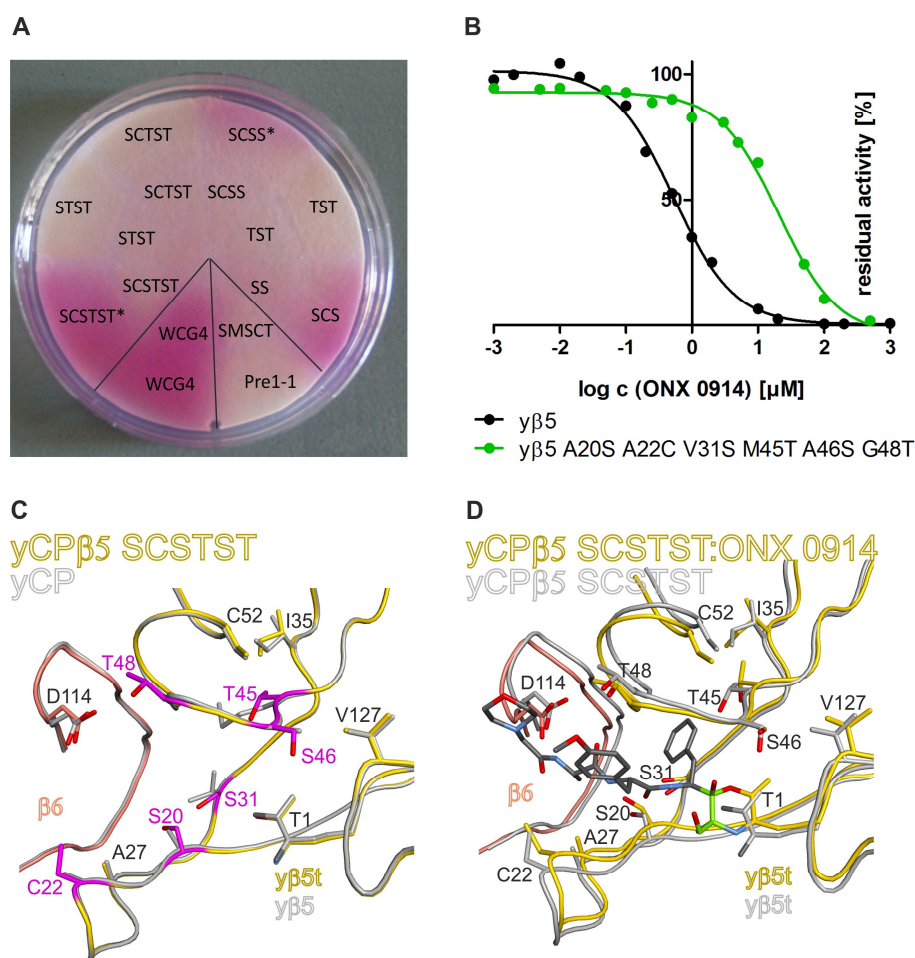


**Figure 32 Structural examination of a  $\beta 5t$  mimicking yCP.** (A) An overlay assay using the chromogenic substrate Cbz-Gly-Gly-Leu-pNA shows the marked reduction in ChTL activity upon introduction of  $\beta 5t$ -specific mutations. Wildtype yeast (WCG4a) served as a positive control, whereas the  $\beta 5i$ -mimicking  $y\beta 5$  mutant SMSCT and the CP mutant Pre1-1, which is lacking ChTL activity, were used as negative controls. Mutant clones marked with a star showed unspecific staining. For abbreviations of mutants see Table 3. (B) Suc-Leu-Leu-Val-Tyr-AMC was used as a fluorogenic substrate to assess the inhibition of the mutated subunit  $\beta 5$  by the epoxyketone ONX 0914. The affinity of ONX 0914 is strongly attenuated in the mutant CP. (C, D) Comparison of the wildtype and mutant (SCSTST)  $y\beta 5$  substrate binding channels depicts the differences in their primary sequences (magenta) and illustrates structural changes upon ligand binding. Amino acids are labelled for the mutant CP.

(Figure 32A). Moreover, the  $IC_{50}$  value of ONX 0914 for the SCSTST mutant  $y\beta 5$  active site strongly increased to  $20.57 \mu M \pm 3.78 \mu M$  compared to  $0.499 \mu M$  for wt  $y\beta 5$ . Even though the S1 pocket of the  $y\beta 5$  SCSTST mutant is enlarged, the opposing forces between the hydrophobic side chains of ONX 0914 and the charged amino acid lining of the substrate binding pockets of the  $y\beta 5$  mutant SCSTST strongly impair binding of the ligand.

Despite the reduced affinity of ONX 0914 for this mutant yCP structural data could be obtained in the absence and the presence of the compound (Table 20). Positive  $F_O-F_C$  density maps proved the incorporation of all mutations. The wt and mutant  $y\beta 5$  active sites superimpose well and show no structural changes for the mutant subunit (r.m.s.d.  $C_\alpha$   $y\beta 5/y\beta 5t$ :  $0.2 \text{ \AA}$ ). Comparison of the ligand-free and ligand-bound states of the  $\beta 5t$ -like

---

substrate binding channel depicts the turn away of Thr45 from the hydrophobic ligand ONX 0914. In addition, strong backbone distortions (r.m.s.d.  $C_{\alpha}$  y $\beta$ 5t/y $\beta$ 5t:ONX 0914: 0.72 Å) are observed upon ligand binding even though no obvious clashes with the protein occur. The reason for this tremendous backbone shift upon inhibitor binding cannot be deduced from the mutant structures and has to be further investigated by structural analysis of the tCP.

## 7 Discussion

The here presented crystallographic analysis of the murine cCP and iCP emphasizes the biological impact of subtle differences that are not predictable from sequence alignments and that can only be resolved by structural data. However, owing to the applied methodology, the results presented provide no insights into the dynamics of the 20S proteasome that might have substantial effects on substrate binding as well as enzyme inhibition.

### 7.1 Structural and functional differences between the three types of CPs

The high structural identity of the unprimed  $\beta$ 2c and  $\beta$ 2i substrate binding channels implicates similar cleavage preferences, leading to the generation of MHC I ligands with neutral or basic C-terminal amino acids<sup>[111]</sup>. Hence, the cCP and iCP structures elicit the question of why  $\beta$ 2i, which is the only i subunit that is not encoded on the MHC gene cluster, is sequestered into iCPs. For the elucidation of the distinct physiological roles of the  $\beta$ 2c and  $\beta$ 2i subunits site-specific probes or subunit-selective compounds would be required. So far, mice lacking subunit  $\beta$ 2i were demonstrated to be not affected by DSS-induced colitis<sup>[53a]</sup> and drugs targeting both TL active sites were proven to sensitize malignant cells for inhibition of the  $\beta$ 5 active sites of the proteasome<sup>[77]</sup>. Together, these preliminary results suggest a therapeutically relevant function also for the  $\beta$ 2 subunits, which both exert rather broad substrate specificities.

According to previous suggestions<sup>[13]</sup>, the unprimed substrate binding sites of subunit  $\beta$ 1i are lined with apolar protein side chains that give rise to a Braap activity<sup>[33b]</sup>. Thus, incorporation of subunit  $\beta$ 1i into the iCP stimulates the generation of high-affinity MHC I peptides. In agreement, the cytotoxic T cell responses of  $\beta$ 1i-deficient mice are altered with respect to their antigen specificity<sup>[112]</sup>.

The exchange of subunit  $\beta$ 5c by  $\beta$ 5i is suggested to generally enhance peptide bond cleavage due to the unique hydrophilicity in proximity to the active site Thr1 of subunit  $\beta$ 5i<sup>[32]</sup>. In particular, the strictly conserved amino acids Ser46 and Thr127 are suggested to stimulate protein degradation. In agreement the 26S immunoproteasome was attributed twice the activity of the constitutive 26S proteasome<sup>[38]</sup> and the rates of antigen processing were shown to influence the immunogenicity of epitopes<sup>[113]</sup>. Despite similar primary sequences for the  $\beta$ 5c and  $\beta$ 5i substrate specificity pockets both subunits still differ in their cleavage patterns<sup>[114]</sup>. Distinct conformations of Met45 cause subunit  $\beta$ 5c to preferentially bind tiny

non-polar amino acids such as alanine or valine in the S1 pocket, while subunit  $\beta 5i$  favours bulky aromatic P1 residues like phenylalanine, tyrosine<sup>[115]</sup> and tryptophan. These substrate preferences are in line with the published selective fluorogenic AMC-substrates Ac-Trp-Leu-Ala-AMC for subunit  $\beta 5c$  and Ac-Ala-Asn-Trp-AMC for subunit  $\beta 5i$ <sup>[110]</sup>. Leucine and isoleucine are supposed to target subunit  $\beta 5c$  with a slight preference over  $\beta 5i$ . Both presumably displace Met45 in subunit  $\beta 5c$ , but might also not be sufficiently stabilized in the spacious S1 pocket of subunit  $\beta 5i$  during initial ligand docking. By contrast, Tyr fits well in the S1 pocket of subunit  $\beta 5i$  and is exceptionally well-stabilized in the  $\beta 5c$  counterpart by interactions with Ser53 ( $\beta 5c$ ) and Ser129 ( $\beta 6$ ). Therefore, it is accepted by both  $\beta 5c$  and  $\beta 5i$  as a P1 residue. In conclusion, subunit  $\beta 5i$  evolved to efficiently support antigen presentation by producing epitopes with a broad range of hydrophobic C-terminal amino acids for tight binding to MHC I receptors. Its outstanding role for antigen generation is corroborated by a 50 % reduction in MHC I levels in  $\beta 5i$ -deficient mice<sup>[116]</sup> and their enhanced predisposition to infections<sup>[117]</sup>. Notably, the deletion of the subunits  $\beta 1i$  or  $\beta 2i$  does not affect MHC I expression<sup>[23, 118]</sup>.

Mutagenesis experiments aimed at mimicking the key features of subunit  $\beta 5i$  in yeast in order to investigate in more detail the subtle differences between the  $\beta 5$  active sites. The created mutants addressed all sequence differences in the substrate binding pockets and around the catalytic Thr1. However, none of the mutant CPs was as susceptible to inhibition by ONX 0914 as subunit  $\beta 5i$  and in agreement their X-ray structures depicted no change in the side chain conformation of Met45. These findings point out that indeed the structural differences between the  $\beta 5c$  and  $\beta 5i$  subunits provoke their different substrate specificities. Furthermore, the structural and functional key features of the iCP are based rather on long-range effects and amino acid networks than on single point mutations. Remarkably, substitution of the  $y\beta 5$  subunit by the mammalian  $\beta 5i$  entity is lethal to yeast even when using codon-optimized sequences and even when the  $y\beta 5$  propeptide replaces the  $\beta 5i$  counterpart (unpublished data of W. Heinemeyer). Analysis of the subunit contacts in the yCP and iCP suggest that solely Arg57 might suppress assembly of subunit  $\beta 5i$  into the yCP by clashing with the adjacent Arg82 from subunit  $y\beta 6$ , but even a  $\beta 5i$  R57T mutant could not be successfully incorporated into the yCP (unpublished results of W. Heinemeyer).

Unlike the  $\beta 5i$  subunit, the  $\beta 5c$  active site presumably has been successfully imitated in yeast. Mutation of Gln53 to Ser enhanced the selectivity for leucine residues in P1 without any obvious structural changes. Thus, amino acid 53 plays a crucial role in determining the cleavage preference of  $\beta 5c$  and  $\beta 5i$  subunits by modulating the interaction strength with

Met45. Notably, this observation does probably not apply to subunit  $\beta 5t$ , as Thr cannot adopt diverse side chain conformations like Met45 and does not interact with Ala53, which is strictly conserved among  $\beta 5t$  sequences.

Importantly, for all CP inhibition experiments the fluorogenic substrate Suc-Leu-Leu-Val-Tyr-AMC was used, irrespective of the mutations introduced in subunit  $\gamma\beta 5$ . For a more correct determination of  $IC_{50}$  values specific fluorogenic peptide substrates for the subunits  $\beta 5c$ ,  $\beta 5i$  and  $\beta 5t$  would be appropriate.

## 7.2 Guidelines for the rational design of CP-selective inhibitors

Various diseases, including autoimmune disorders and cancers, are characterized by elevated levels of inflammation signals and iCP subunits<sup>[22]</sup>. Hence, iCP-selective compounds constitute promising novel drugs for the treatment of autoimmune diseases. The iCP-selective inhibitor ONX 0914 was proven to halt disease progression in rheumatoid arthritis, experimental colitis, systemic lupus erythematosus and Hashimoto's thyroiditis by decreasing the levels of proinflammatory cytokines as well as autoantibodies and by modulating cytotoxic T cell responses<sup>[37, 53]</sup>.

Previous studies demonstrated that peptide based inhibitors of the CP including ONX 0914 mimic the binding mode of natural substrates by forming an antiparallel  $\beta$  sheet in the substrate binding channels of the active sites<sup>[13]</sup>. The herein presented crystal structures now elucidated that the binding mechanism of ONX 0914 to all active sites of the proteasome, the c and i subunits, is identical. Furthermore the selectivity of compounds solely depends on the potency of their electrophilic head group and the interactions of the ligand's P sites with the surrounding protein side chains. The exceptional importance of the interaction between the P1 site and the S1 pocket revealed by this study is corroborated by the nonpeptidic proteasome inhibitors salinosporamide A (marizomib) and omuralide that both occupy only the S1 site<sup>[13, 59]</sup>. Bearing in mind the uniform proteolytic mechanism of all active proteasome subunits, subunit-specific inhibitory compounds can only be developed by varying the side chains of peptidomimetics:  $\beta 1c$  targeting compounds require acidic amino acids in their P1 site, while the hydrophobicity of the S1 pocket in  $\beta 1i$  leads to a preference for branched hydrophobic residues, such as Val, Ile or Leu. Moreover, subunit  $\beta 1i$  favours smaller and more polar amino acids in the S3 pocket than subunit  $\beta 1c$ . Subunit  $\beta 5c$  is perfectly suited to accommodate small apolar residues in P1, while subunit  $\beta 5i$  is adapted for binding aromatic amino acids. The P3 site of subunit  $\beta 5c$  accepts bulky hydrophobic side chains, whereas the P3 site of subunit  $\beta 5i$

demands for small and preferentially polar residues. Since the S2 sites of the substrate binding channels are either shallow (subunit  $\beta 1c/i$ ,  $\beta 2c/i$  and  $\beta 5i$ ) or even lacking ( $\beta 5c$ ), the P2 positions can be occupied by spacious side chains of diverse chemical nature.

Ligand complex structures revealed that binding of the phenyl P1 side chain of ONX 0914 to subunit  $\beta 5c$  is primarily disfavoured by sterical hindrance with Met45. Consistently, non-natural derivatives of salinosporamide A and omuralide, bearing a phenyl moiety in the P1 site, demonstrate less affinity for the subunits  $y\beta 5$  and  $\beta 5c$  compared to their natural counterparts<sup>[119]</sup>. Besides ONX 0914, the epoxyketone PR-924 (Figure 7) represents another  $\beta 5i$ -selective compound with phenylalanine as P1 side chain and alanine as P3 residue. However, unlike ONX 0914 and PR-924, the epoxyketone oprozomib (ONX 0912; Figure 6) that also bears a phenyl group as P1 residue is a potent inhibitor of both  $\beta 5c$  and  $\beta 5i$  with even slight preferences for the c subunit. The iCP crystal structure provides a plausible explanation for this observation. The methoxyserine of ONX 0912 fits into the S3 pocket of the  $\beta 5c$  subunit formed by Ala27, but Ser27 in subunit  $\beta 5i$  diminishes the size of the  $\beta 5i$  S3 pocket and thus, electrostatically and sterically hinders binding of ONX 0912 to  $\beta 5i$ . In this regard, even though the P1 residue appears to be the major determinant for the affinity of a ligand, the P2 and P3 residues also significantly contribute to the  $IC_{50}$  values. PR-825 (Figure 7) a structural analogue of ONX 0912 that possesses a leucine instead of a phenyl residue in P1, targets subunit  $\beta 5c$  with 20-fold selectivity over  $\beta 5i$ , demonstrating that leucine

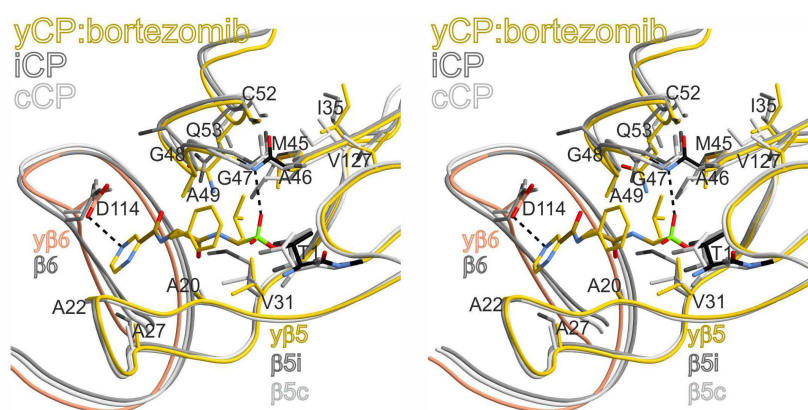


**Figure 33 Stereo illustration of the  $yCP$ :bortezomib complex structure superimposed onto the  $cCP$  and  $iCP$ .** Structural comparison of the bortezomib bound  $y\beta 5$  subunit and the unliganded murine  $\beta 5c$  and  $\beta 5i$  active sites. Amino acids are labelled for the  $y\beta 5$  subunit. Hydrogen bonds between bortezomib and the surrounding protein residues are indicated by black dashed lines.

Adapted from Huber *et al.*, 2012<sup>[32]</sup>.

and methoxyserine are suited to preferentially bind to the  $cCP$ . Carfilzomib, carrying a leucine side chain in both P1 and P3 sites is reported to be 5-times more selective for  $\beta 5c$  than  $\beta 5i$ <sup>[74]</sup>.

Hence, leucine in P1 and leucine or methoxyserine in P3 give rise to  $\beta$ 5c selectivity. Moreover, the yCP:bortezomib complex structure<sup>[67]</sup> together with the cCP and iCP coordinates elucidate that the P1 leucine and the P3 pyrazine ring of bortezomib fit into subunit  $\beta$ 5i and  $\beta$ 5c by interacting with Thr21, Ala22 and Ala27/Ser27 of  $\beta$ 5c/i and Asp144 of the neighbouring subunit  $\beta$ 6 (Figure 33). Hereby, bortezomib is capable of potently inhibiting both the cCP and iCP.

Bearing in mind a sequence identity of more than 90 % between murine and human subunits, the design of novel selective proteasome inhibitors for single CP-types and CP-subunits is now amenable. Such compounds enable the detailed examination of the biological impact of each active proteasome subunit and have huge medicinal potentials for the treatment of cancer and autoimmune diseases.

## 8 Bibliography

- [1] D. Finley (2009). Recognition and processing of ubiquitin-protein conjugates by the proteasome, *Annu. Rev. Biochem.*, *78*, 477-513.
- [2] A. L. Goldberg, K. L. Rock (1992). Proteolysis, proteasomes and antigen presentation, *Nature*, *357*, 375-379.
- [3] a) J. D. Etlinger, A. L. Goldberg (1977). A soluble ATP-dependent proteolytic system responsible for the degradation of abnormal proteins in reticulocytes, *Proc. Natl. Acad. Sci. U S A*, *74*, 54-58; b) A. Hershko, A. Ciechanover (1998). The ubiquitin system, *Annu. Rev. Biochem.*, *67*, 425-479.
- [4] a) I. A. York, S. C. Chang, T. Saric, J. A. Keys, J. M. Favreau, A. L. Goldberg, K. L. Rock (2002). The ER aminopeptidase ERAP1 enhances or limits antigen presentation by trimming epitopes to 8-9 residues, *Nat. Immunol.*, *3*, 1177-1184; b) K. L. Rock, I. A. York, A. L. Goldberg (2004). Post-proteasomal antigen processing for major histocompatibility complex class I presentation, *Nat. Immunol.*, *5*, 670-677.
- [5] A. Townsend, J. Trowsdale (1993). The transporters associated with antigen presentation, *Semin. Cell Biol.*, *4*, 53-61.
- [6] a) V. H. Engelhard (1994). Structure of peptides associated with MHC class I molecules, *Curr. Opin. Immunol.*, *6*, 13-23; b) K. Falk, O. Rotzschke, S. Stevanovic, G. Jung, H. G. Rammensee (1991). Allele-specific motifs revealed by sequencing of self-peptides eluted from MHC molecules, *Nature*, *351*, 290-296.
- [7] a) J. M. Vyas, A. G. Van der Veen, H. L. Ploegh (2008). The known unknowns of antigen processing and presentation, *Nat. Rev. Immunol.*, *8*, 607-618; b) J. Neefjes, M. L. Jongsma, P. Paul, O. Bakke (2011). Towards a systems understanding of MHC class I and MHC class II antigen presentation, *Nat. Rev. Immunol.*, *11*, 823-836.
- [8] C. M. Pickart (2001). Mechanisms underlying ubiquitination, *Annu. Rev. Biochem.*, *70*, 503-533.
- [9] J. M. T. Berg, J. L.; Stryer, L. (2002). *Biochemistry*, New York: W H Freeman.
- [10] D. Voges, P. Zwickl, W. Baumeister (1999). The 26S proteasome: a molecular machine designed for controlled proteolysis, *Annu. Rev. Biochem.*, *68*, 1015-1068.
- [11] M. Bochtler, L. Ditzel, M. Groll, R. Huber (1997). Crystal structure of heat shock locus V (HslV) from *Escherichia coli*, *Proc. Natl. Acad. Sci. U S A*, *94*, 6070-6074.
- [12] J. Löwe, D. Stock, B. Jap, P. Zwickl, W. Baumeister, R. Huber (1995). Crystal structure of the 20S proteasome from the archaeon *T. acidophilum* at 3.4 Å resolution, *Science*, *268*, 533-539.
- [13] M. Groll, L. Ditzel, J. Löwe, D. Stock, M. Bochtler, H. D. Bartunik, R. Huber (1997). Structure of 20S proteasome from yeast at 2.4 Å resolution, *Nature*, *386*, 463-471.
- [14] P. Zwickl, A. Grziwa, G. Puhler, B. Dahlmann, F. Lottspeich, W. Baumeister (1992). Primary structure of the *Thermoplasma* proteasome and its implications for the structure, function, and evolution of the multicatalytic proteinase, *Biochemistry*, *31*, 964-972.
- [15] K. Tanaka, T. Yoshimura, T. Tamura, T. Fujiwara, A. Kumatori, A. Ichihara (1990). Possible mechanism of nuclear translocation of proteasomes, *FEBS Lett.*, *271*, 41-46.
- [16] a) M. Groll, M. Bajorek, A. Köhler, L. Moroder, D. M. Rubin, R. Huber, M. H. Glickman, D. Finley (2000). A gated channel into the proteasome core particle, *Nat. Struct. Biol.*, *7*, 1062-1067; b) F. G. Whitby, E. I. Masters, L. Kramer, J. R. Knowlton, Y. Yao, C. C. Wang, C. P. Hill (2000). Structural basis for the activation of 20S proteasomes by 11S regulators, *Nature*, *408*, 115-120.
- [17] B. M. Stadtmueller, C. P. Hill (2011). Proteasome activators, *Mol. Cell*, *41*, 8-19.

- [18] P. C. Ramos, J. Hockendorff, E. S. Johnson, A. Varshavsky, R. J. Dohmen (1998). Ump1p is required for proper maturation of the 20S proteasome and becomes its substrate upon completion of the assembly, *Cell*, *92*, 489-499.
- [19] M. Groll, W. Heinemeyer, S. Jäger, T. Ullrich, M. Bochtler, D. H. Wolf, R. Huber (1999). The catalytic sites of 20S proteasomes and their role in subunit maturation: a mutational and crystallographic study, *Proc. Natl. Acad. Sci. U S A*, *96*, 10976-10983.
- [20] L. Ditzel, R. Huber, K. Mann, W. Heinemeyer, D. H. Wolf, M. Groll (1998). Conformational constraints for protein self-cleavage in the proteasome, *J. Mol. Biol.*, *279*, 1187-1191.
- [21] a) M. Unno, T. Mizushima, Y. Morimoto, Y. Tomisugi, K. Tanaka, N. Yasuoka, T. Tsukihara (2002). The structure of the mammalian 20S proteasome at 2.75 Å resolution, *Structure*, *10*, 609-618; b) M. Groettrup, R. Kraft, S. Kostka, S. Standera, R. Stohwasser, P. M. Kloetzel (1996). A third interferon-gamma-induced subunit exchange in the 20S proteasome, *Eur. J. Immunol.*, *26*, 863-869; c) S. Murata, K. Sasaki, T. Kishimoto, S. Niwa, H. Hayashi, Y. Takahama, K. Tanaka (2007). Regulation of CD8<sup>+</sup> T cell development by thymus-specific proteasomes, *Science*, *316*, 1349-1353.
- [22] E. M. Huber, M. Groll (2012). Inhibitors for the immuno- and constitutive proteasome: current and future trends in drug development, *Angew. Chem. Int. Ed. Engl.*, *51*, 8708-8720.
- [23] M. Groettrup, C. J. Kirk, M. Basler (2010). Proteasomes in immune cells: more than peptide producers?, *Nat. Rev. Immunol.*, *10*, 73-78.
- [24] M. Aki, N. Shimbara, M. Takashina, K. Akiyama, S. Kagawa, T. Tamura, N. Tanahashi, T. Yoshimura, K. Tanaka, A. Ichihara (1994). Interferon-gamma induces different subunit organizations and functional diversity of proteasomes, *J. Biochem.*, *115*, 257-269.
- [25] T. A. Griffin, D. Nandi, M. Cruz, H. J. Fehling, L. V. Kaer, J. J. Monaco, R. A. Colbert (1998). Immunoproteasome assembly: cooperative incorporation of interferon gamma (IFN-gamma)-inducible subunits, *J. Exp. Med.*, *187*, 97-104.
- [26] C. Realini, W. Dubiel, G. Pratt, K. Ferrell, M. Rechsteiner (1994). Molecular cloning and expression of a gamma-interferon-inducible activator of the multicatalytic protease, *J. Biol. Chem.*, *269*, 20727-20732.
- [27] M. Rechsteiner, C. P. Hill (2005). Mobilizing the proteolytic machine: cell biological roles of proteasome activators and inhibitors, *Trends Cell Biol.*, *15*, 27-33.
- [28] M. Rechsteiner, C. Realini, V. Ustrell (2000). The proteasome activator 11 S REG (PA28) and class I antigen presentation, *Biochem. J.*, *345 Pt 1*, 1-15.
- [29] B. Guillaume, J. Chapiro, V. Stroobant, D. Colau, B. Van Holle, G. Parvizi, M. P. Bousquet-Dubouch, I. Theate, N. Parmentier, B. J. Van den Eynde (2010). Two abundant proteasome subtypes that uniquely process some antigens presented by HLA class I molecules, *Proc. Natl. Acad. Sci. U S A*, *107*, 18599-18604.
- [30] N. Klare, M. Seeger, K. Janek, P. R. Jungblut, B. Dahlmann (2007). Intermediate-type 20 S proteasomes in HeLa cells: "asymmetric" subunit composition, diversity and adaptation, *J. Mol. Biol.*, *373*, 1-10.
- [31] M. Groll, M. Bochtler, H. Brandstetter, T. Clausen, R. Huber (2005). Molecular machines for protein degradation, *Chembiochem*, *6*, 222-256.
- [32] E. Huber, M. Basler, R. Schwab, W. Heinemeyer, C. J. Kirk, M. Groettrup, M. Groll (2012). Immuno- and constitutive proteasome crystal structures reveal differences in substrate and inhibitor specificity, *Cell*, *148*, 727-738.
- [33] a) C. Cardozo, R. A. Kohanski (1998). Altered properties of the branched chain amino acid-preferring activity contribute to increased cleavages after branched chain residues by the "immunoproteasome", *J. Biol. Chem.*, *273*, 16764-16770; b) M. Orłowski, C.

- Cardozo, C. Michaud (1993). Evidence for the presence of five distinct proteolytic components in the pituitary multicatalytic proteinase complex. Properties of two components cleaving bonds on the carboxyl side of branched chain and small neutral amino acids, *Biochemistry*, *32*, 1563-1572.
- [34] a) M. Gaczynska, K. L. Rock, A. L. Goldberg (1993). Gamma-interferon and expression of MHC genes regulate peptide hydrolysis by proteasomes, *Nature*, *365*, 264-267; b) J. Driscoll, M. G. Brown, D. Finley, J. J. Monaco (1993). MHC-linked LMP gene products specifically alter peptidase activities of the proteasome, *Nature*, *365*, 262-264.
- [35] a) B. J. Van den Eynde, S. Morel (2001). Differential processing of class-I-restricted epitopes by the standard proteasome and the immunoproteasome, *Curr. Opin. Immunol.*, *13*, 147-153; b) S. Murata, Y. Takahama, K. Tanaka (2008). Thymoproteasome: probable role in generating positively selecting peptides, *Curr. Opin. Immunol.*, *20*, 192-196.
- [36] E. Z. Kincaid, J. W. Che, I. York, H. Escobar, E. Reyes-Vargas, J. C. Delgado, R. M. Welsh, M. L. Karow, A. J. Murphy, D. M. Valenzuela, G. D. Yancopoulos, K. L. Rock (2011). Mice completely lacking immunoproteasomes show major changes in antigen presentation, *Nat. Immunol.*, *13*, 129-135.
- [37] T. Muchamuel, M. Basler, M. A. Aujay, E. Suzuki, K. W. Kalim, C. Lauer, C. Sylvain, E. R. Ring, J. Shields, J. Jiang, P. Shwonek, F. Parlati, S. D. Demo, M. K. Bennett, C. J. Kirk, M. Groettrup (2009). A selective inhibitor of the immunoproteasome subunit LMP7 blocks cytokine production and attenuates progression of experimental arthritis, *Nat. Med.*, *15*, 781-787.
- [38] U. Seifert, L. P. Bialy, F. Ebstein, D. Bech-Otschir, A. Voigt, F. Schroter, T. Prozorovski, N. Lange, J. Steffen, M. Rieger, U. Kuckelkorn, O. Aktas, P. M. Kloetzel, E. Kruger (2010). Immunoproteasomes preserve protein homeostasis upon interferon-induced oxidative stress, *Cell*, *142*, 613-624.
- [39] N. R. Gascoigne, E. Palmer (2011). Signaling in thymic selection, *Curr. Opin. Immunol.*, *23*, 207-212.
- [40] M. J. Bevan (2007). Immunology. The cutting edge of T cell selection, *Science*, *316*, 1291-1292.
- [41] a) P. M. Voorhees, E. C. Dees, B. O'Neil, R. Z. Orlowski (2003). The proteasome as a target for cancer therapy, *Clin. Cancer Res.*, *9*, 6316-6325; b) L. R. Dick, P. E. Fleming (2010). Building on bortezomib: second-generation proteasome inhibitors as anti-cancer therapy, *Drug Discov. Today*, *15*, 243-249.
- [42] a) D. J. McConkey, K. Zhu (2008). Mechanisms of proteasome inhibitor action and resistance in cancer, *Drug Resist. Updat.*, *11*, 164-179; b) S. T. Nawrocki, J. S. Carew, K. Dunner, Jr., L. H. Boise, P. J. Chiao, P. Huang, J. L. Abbuzzese, D. J. McConkey (2005). Bortezomib inhibits PKR-like endoplasmic reticulum (ER) kinase and induces apoptosis via ER stress in human pancreatic cancer cells, *Cancer Res.*, *65*, 11510-11519; c) E. A. Obeng, L. M. Carlson, D. M. Gutman, W. J. Harrington, Jr., K. P. Lee, L. H. Boise (2006). Proteasome inhibitors induce a terminal unfolded protein response in multiple myeloma cells, *Blood*, *107*, 4907-4916; d) G. Bianchi, L. Oliva, P. Cascio, N. Pengo, F. Fontana, F. Cerruti, A. Orsi, E. Pasqualetto, A. Mezghrani, V. Calbi, G. Palladini, N. Giuliani, K. C. Anderson, R. Sitia, S. Cenci (2009). The proteasome load versus capacity balance determines apoptotic sensitivity of multiple myeloma cells to proteasome inhibition, *Blood*, *113*, 3040-3049; e) T. Mujtaba, Q. P. Dou (2011). Advances in the understanding of mechanisms and therapeutic use of bortezomib, *Discov. Med.*, *12*, 471-480.
- [43] I. Nickleit, S. Zender, F. Sasse, R. Geffers, G. Brandes, I. Sorensen, H. Steinmetz, S. Kubicka, T. Carlomagno, D. Menche, I. Gutgemann, J. Buer, A. Gossler, M. P.

- Manns, M. Kalesse, R. Frank, N. P. Malek (2008). Argyrin a reveals a critical role for the tumor suppressor protein p27(kip1) in mediating antitumor activities in response to proteasome inhibition, *Cancer Cell*, *14*, 23-35.
- [44] a) W. Lee, K. B. Kim (2011). The immunoproteasome: an emerging therapeutic target, *Curr. Top. Med. Chem.*, *11*, 2923-2930; b) Y. K. Ho, P. Bargagna-Mohan, M. Wehenkel, R. Mohan, K. B. Kim (2007). LMP2-specific inhibitors: chemical genetic tools for proteasome biology, *Chem. Biol.*, *14*, 419-430.
- [45] M. Mishto, E. Bellavista, A. Santoro, A. Stolzing, C. Ligorio, B. Nacmias, L. Spazzafumo, M. Chiappelli, F. Licastro, S. Sorbi, A. Pession, T. Ohm, T. Grune, C. Franceschi (2006). Immunoproteasome and LMP2 polymorphism in aged and Alzheimer's disease brains, *Neurobiol. Aging*, *27*, 54-66.
- [46] M. Diaz-Hernandez, F. Hernandez, E. Martin-Aparicio, P. Gomez-Ramos, M. A. Moran, J. G. Castano, I. Ferrer, J. Avila, J. J. Lucas (2003). Neuronal induction of the immunoproteasome in Huntington's disease, *J. Neurosci.*, *23*, 11653-11661.
- [47] K. Puttaparthi, J. L. Elliott (2005). Non-neuronal induction of immunoproteasome subunits in an ALS model: possible mediation by cytokines, *Exp. Neurol.*, *196*, 441-451.
- [48] L. R. Fitzpatrick, J. S. Small, L. S. Poritz, K. J. McKenna, W. A. Koltun (2007). Enhanced intestinal expression of the proteasome subunit low molecular mass polypeptide 2 in patients with inflammatory bowel disease, *Dis. Colon Rectum*, *50*, 337-348; discussion 348-350.
- [49] T. Egerer, L. Martinez-Gamboa, A. Dankof, B. Stuhlmuller, T. Dorner, V. Krenn, K. Egerer, P. E. Rudolph, G. R. Burmester, E. Feist (2006). Tissue-specific up-regulation of the proteasome subunit beta5i (LMP7) in Sjogren's syndrome, *Arthritis Rheum.*, *54*, 1501-1508.
- [50] a) I. Ferrer, B. Martin, J. G. Castano, J. J. Lucas, D. Moreno, M. Olive (2004). Proteasomal expression, induction of immunoproteasome subunits, and local MHC class I presentation in myofibrillar myopathy and inclusion body myositis, *J. Neuropathol. Exp. Neurol.*, *63*, 484-498; b) Z. Yang, D. Gagarin, G. St Laurent, 3rd, N. Hammell, I. Toma, C. A. Hu, A. Iwasa, T. A. McCaffrey (2009). Cardiovascular inflammation and lesion cell apoptosis: a novel connection via the interferon-inducible immunoproteasome, *Arterioscler. Thromb. Vasc. Biol.*, *29*, 1213-1219.
- [51] A. Visekruna, N. Slavova, S. Dullat, J. Grone, A. J. Kroesen, J. P. Ritz, H. J. Buhr, U. Steinhoff (2009). Expression of catalytic proteasome subunits in the gut of patients with Crohn's disease, *Int. J. Colorectal. Dis.*, *24*, 1133-1139.
- [52] L. R. Fitzpatrick, V. Khare, J. S. Small, W. A. Koltun (2006). Dextran sulfate sodium-induced colitis is associated with enhanced low molecular mass polypeptide 2 (LMP2) expression and is attenuated in LMP2 knockout mice, *Dig. Dis. Sci.*, *51*, 1269-1276.
- [53] a) M. Basler, M. Dajee, C. Moll, M. Groettrup, C. J. Kirk (2010). Prevention of experimental colitis by a selective inhibitor of the immunoproteasome, *J. Immunol.*, *185*, 634-641; b) H. T. Ichikawa, T. Conley, T. Muchamuel, J. Jiang, S. Lee, T. Owen, J. Barnard, S. Nevarez, B. I. Goldman, C. J. Kirk, R. J. Looney, J. H. Anolik (2011). Novel proteasome inhibitors have a beneficial effect in murine lupus via the dual inhibition of type I interferon and autoantibody secreting cells, *Arthritis Rheum.*, *64*, 493-503; c) Y. Nagayama, M. Nakahara, M. Shimamura, I. Horie, K. Arima, N. Abiru (2012). Prophylactic and therapeutic efficacies of a selective inhibitor of the immunoproteasome for Hashimoto's thyroiditis, but not for Graves' hyperthyroidism, in mice, *Clin. Exp. Immunol.*, *168*, 268-273.
- [54] a) D. J. Kuhn, S. A. Hunsucker, Q. Chen, P. M. Voorhees, M. Orłowski, R. Z. Orłowski (2009). Targeted inhibition of the immunoproteasome is a potent strategy against models of multiple myeloma that overcomes resistance to conventional drugs

- and nonspecific proteasome inhibitors, *Blood*, *113*, 4667-4676; b) A. V. Singh, M. Bandi, M. A. Aujay, C. J. Kirk, D. E. Hark, N. Raje, D. Chauhan, K. C. Anderson (2011). PR-924, a selective inhibitor of the immunoproteasome subunit LMP-7, blocks multiple myeloma cell growth both in vitro and in vivo, *Br. J. Haematol.*, *152*, 155-163.
- [55] F. Parlati, S. J. Lee, M. Aujay, E. Suzuki, K. Levitsky, J. B. Lorens, D. R. Micklem, P. Ruurs, C. Sylvain, Y. Lu, K. D. Shenk, M. K. Bennett (2009). Carfilzomib can induce tumor cell death through selective inhibition of the chymotrypsin-like activity of the proteasome, *Blood*, *114*, 3439-3447.
- [56] A. Vinitsky, C. Michaud, J. C. Powers, M. Orłowski (1992). Inhibition of the chymotrypsin-like activity of the pituitary multicatalytic proteinase complex, *Biochemistry*, *31*, 9421-9428.
- [57] M. Bogyo, J. S. McMaster, M. Gaczynska, D. Tortorella, A. L. Goldberg, H. Ploegh (1997). Covalent modification of the active site threonine of proteasomal beta subunits and the *Escherichia coli* homolog HslV by a new class of inhibitors, *Proc. Natl. Acad. Sci. U S A*, *94*, 6629-6634.
- [58] M. Groll, B. Schellenberg, A. S. Bachmann, C. R. Archer, R. Huber, T. K. Powell, S. Lindow, M. Kaiser, R. Dudler (2008). A plant pathogen virulence factor inhibits the eukaryotic proteasome by a novel mechanism, *Nature*, *452*, 755-758.
- [59] M. Groll, R. Huber, B. C. Potts (2006). Crystal structures of Salinosporamide A (NPI-0052) and B (NPI-0047) in complex with the 20S proteasome reveal important consequences of beta-lactone ring opening and a mechanism for irreversible binding, *J. Am. Chem. Soc.*, *128*, 5136-5141.
- [60] M. Groll, B. C. Potts (2011). Proteasome structure, function, and lessons learned from beta-lactone inhibitors, *Curr. Top. Med. Chem.*, *11*, 2850-2878.
- [61] a) M. Groll, K. B. Kim, N. Kairies, R. Huber, C. M. Crews (2000). Crystal structure of epoxomicin: 20S proteasome reveals a molecular basis for selectivity of  $\alpha'$ ,  $\beta'$ -epoxyketone proteasome inhibitors, *J. Am. Chem. Soc.*, *122*, 1237-1238; b) K. B. Kim, J. Myung, N. Sin, C. M. Crews (1999). Proteasome inhibition by the natural products epoxomicin and dihydroeponemycin: insights into specificity and potency, *Bioorg. Med. Chem. Lett.*, *9*, 3335-3340.
- [62] M. A. Grawert, N. Gallastegui, M. Stein, B. Schmidt, P. M. Kloetzel, R. Huber, M. Groll (2011). Elucidation of the alpha-keto-aldehyde binding mechanism: a lead structure motif for proteasome inhibition, *Angew. Chem. Int. Ed. Engl.*, *50*, 542-544.
- [63] L. Borissenko, M. Groll (2007). 20S proteasome and its inhibitors: crystallographic knowledge for drug development, *Chem. Rev.*, *107*, 687-717.
- [64] R. C. Kane, P. F. Bross, A. T. Farrell, R. Pazdur (2003). Velcade: U.S. FDA approval for the treatment of multiple myeloma progressing on prior therapy, *Oncologist*, *8*, 508-513.
- [65] I. Tzvetanov, M. Spaggiari, J. Joseph, H. Jeon, J. Thielke, J. Oberholzer, E. Benedetti (2012). The use of bortezomib as a rescue treatment for acute antibody-mediated rejection: report of three cases and review of literature, *Transplant. Proc.*, *44*, 2971-2975.
- [66] M. Escobar, M. Velez, A. Belalcazar, E. S. Santos, L. E. Ruez (2011). The role of proteasome inhibition in nonsmall cell lung cancer, *J. Biomed. Biotechnol.*, *2011*, 806506.
- [67] M. Groll, C. R. Berkers, H. L. Ploegh, H. Ovaas (2006). Crystal structure of the boronic acid-based proteasome inhibitor bortezomib in complex with the yeast 20S proteasome, *Structure*, *14*, 451-456.
- [68] S. Arastu-Kapur, J. L. Anderl, M. Kraus, F. Parlati, K. D. Shenk, S. J. Lee, T. Muchamuel, M. K. Bennett, C. Driessen, A. J. Ball, C. J. Kirk (2011).

- Nonproteasomal targets of the proteasome inhibitors bortezomib and carfilzomib: a link to clinical adverse events, *Clin. Cancer Res.*, *17*, 2734-2743.
- [69] P. Moreau, P. G. Richardson, M. Cavo, R. Z. Orlowski, J. F. San Miguel, A. Palumbo, J. L. Harousseau (2012). Proteasome inhibitors in multiple myeloma: 10 years later, *Blood*, *120*, 947-959.
- [70] S. Kumar, S. V. Rajkumar (2008). Many facets of bortezomib resistance/susceptibility, *Blood*, *112*, 2177-2178.
- [71] D. Chauhan, G. Li, R. Shringarpure, K. Podar, Y. Ohtake, T. Hideshima, K. C. Anderson (2003). Blockade of Hsp27 overcomes Bortezomib/proteasome inhibitor PS-341 resistance in lymphoma cells, *Cancer Res.*, *63*, 6174-6177.
- [72] a) R. Oerlemans, N. E. Franke, Y. G. Assaraf, J. Cloos, I. van Zantwijk, C. R. Berkers, G. L. Scheffer, K. Debipersad, K. Vojtekova, C. Lemos, J. W. van der Heijden, B. Ylstra, G. J. Peters, G. L. Kaspers, B. A. Dijkmans, R. J. Scheper, G. Jansen (2008). Molecular basis of bortezomib resistance: proteasome subunit beta5 (PSMB5) gene mutation and overexpression of PSMB5 protein, *Blood*, *112*, 2489-2499; b) S. Lu, J. Yang, Z. Chen, S. Gong, H. Zhou, X. Xu, J. Wang (2009). Different mutants of PSMB5 confer varying bortezomib resistance in T lymphoblastic lymphoma/leukemia cells derived from the Jurkat cell line, *Exp. Hematol.*, *37*, 831-837; c) N. E. Franke, D. Niewerth, Y. G. Assaraf, J. van Meerloo, K. Vojtekova, C. H. van Zantwijk, S. Zweegman, E. T. Chan, C. J. Kirk, D. P. Geerke, A. D. Schimmer, G. J. Kaspers, G. Jansen, J. Cloos (2011). Impaired bortezomib binding to mutant beta5 subunit of the proteasome is the underlying basis for bortezomib resistance in leukemia cells, *Leukemia*, *26*, 757-768; d) E. Suzuki, S. Demo, E. Deu, J. Keats, S. Arastu-Kapur, P. L. Bergsagel, M. K. Bennett, C. J. Kirk (2011). Molecular mechanisms of bortezomib resistant adenocarcinoma cells, *PLoS One*, *6*, e27996.
- [73] K. Fostier, A. De Becker, R. Schots (2012). Carfilzomib: a novel treatment in relapsed and refractory multiple myeloma, *OncoTargets Ther.*, *5*, 237-244.
- [74] S. D. Demo, C. J. Kirk, M. A. Aujay, T. J. Buchholz, M. Dajee, M. N. Ho, J. Jiang, G. J. Laidig, E. R. Lewis, F. Parlati, K. D. Shenk, M. S. Smyth, C. M. Sun, M. K. Vallone, T. M. Woo, C. J. Molineaux, M. K. Bennett (2007). Antitumor activity of PR-171, a novel irreversible inhibitor of the proteasome, *Cancer Res.*, *67*, 6383-6391.
- [75] A. M. Ruschak, M. Slassi, L. E. Kay, A. D. Schimmer (2011). Novel proteasome inhibitors to overcome bortezomib resistance, *J. Natl. Cancer Inst.*, *103*, 1007-1017.
- [76] H. J. Zhou, M. A. Aujay, M. K. Bennett, M. Dajee, S. D. Demo, Y. Fang, M. N. Ho, J. Jiang, C. J. Kirk, G. J. Laidig, E. R. Lewis, Y. Lu, T. Muchamuel, F. Parlati, E. Ring, K. D. Shenk, J. Shields, P. J. Shwonek, T. Stanton, C. M. Sun, C. Sylvain, T. M. Woo, J. Yang (2009). Design and synthesis of an orally bioavailable and selective peptide epoxyketone proteasome inhibitor (PR-047), *J. Med. Chem.*, *52*, 3028-3038.
- [77] A. C. Mirabella, A. A. Pletnev, S. L. Downey, B. I. Florea, T. B. Shabaneh, M. Britton, M. Verdoes, D. V. Filippov, H. S. Overkleft, A. F. Kisselev (2011). Specific cell-permeable inhibitor of proteasome trypsin-like sites selectively sensitizes myeloma cells to bortezomib and carfilzomib, *Chem. Biol.*, *18*, 608-618.
- [78] K. W. Kalim, M. Basler, C. J. Kirk, M. Groettrup (2012). Immunoproteasome Subunit LMP7 Deficiency and Inhibition Suppresses Th1 and Th17 but Enhances Regulatory T Cell Differentiation, *J. Immunol.*, *189*, 4182-4193.
- [79] W. O. Bullock, Fernandez, J. M., Short, J. M. (1987). XL1-Blue: A high efficiency plasmid transforming recA *Escherichia coli* strain with beta-galactosidase selection, *BioTechniques*, *5*, 376-379.
- [80] D. Hanahan (1983). Studies on transformation of *Escherichia coli* with plasmids, *J. Mol. Biol.*, *166*, 557-580.

- [81] W. Heinemeyer, A. Gruhler, V. Mohrle, Y. Mahe, D. H. Wolf (1993). PRE2, highly homologous to the human major histocompatibility complex-linked RING10 gene, codes for a yeast proteasome subunit necessary for chrymotryptic activity and degradation of ubiquitinated proteins, *J. Biol. Chem.*, *268*, 5115-5120.
- [82] W. Heinemeyer, J. A. Kleinschmidt, J. Saidowsky, C. Escher, D. H. Wolf (1991). Proteinase yscE, the yeast proteasome/multicatalytic-multifunctional proteinase: mutants unravel its function in stress induced proteolysis and uncover its necessity for cell survival, *EMBO J.*, *10*, 555-562.
- [83] W. Heinemeyer, M. Fischer, T. Krimmer, U. Stachon, D. H. Wolf (1997). The active sites of the eukaryotic 20 S proteasome and their involvement in subunit precursor processing, *J. Biol. Chem.*, *272*, 25200-25209.
- [84] R. J. C. Estiveira (2008). The active subunits of the 20S Proteasome in *Saccharomyces cerevisiae* - Mutational analysis of their specificities and a C-terminal extension, PhD thesis, Universität Stuttgart.
- [85] R. M. Esnouf (1997). An extensively modified version of MolScript that includes greatly enhanced coloring capabilities, *J. Mol. Graph. Model.*, *15*, 132-134, 112-133.
- [86] Collaborative Computational Project (1994). The CCP4 suite: programs for protein crystallography, *Acta Crystallogr. Sect. D - Biol. Crystallogr.*, *50*, 760-763.
- [87] P. Emsley, B. Lohkamp, W. G. Scott, K. Cowtan (2010). Features and development of Coot, *Acta Crystallogr. Sect. D - Biol. Crystallogr.*, *66*, 486-501.
- [88] D. Turk (1992). Improvement of a Programme for Molecular Graphics and Manipulation of Electron Densities and Its Application for Protein Structure Determination, PhD thesis, *Technische Universität München*.
- [89] P. J. Kraulis (1991). *MOLSCRIPT*: a program to produce both detailed and schematic plots of protein structures, *J. Appl. Cryst.*, *24*, 946-950.
- [90] W. L. DeLano (2002). The PyMOL Molecular Graphics System, DeLano Scientific, San Carlos, CA, USA.
- [91] SYBYL 8.0 Tripos International, 1699 South Hanley Rd., St. Louis, Missouri, 63144, USA
- [92] W. Kabsch (2010). Xds, *Acta Crystallogr. Sect. D - Biol. Crystallogr.*, *66*, 125-132.
- [93] E. Krissinel, Henrick, K. (2005). Detection of Protein Assemblies in Crystals, *CompLife 2005*, *3695*, 163-174.
- [94] K. Mullis, F. Faloona, S. Scharf, R. Saiki, G. Horn, H. Erlich (1986). Specific enzymatic amplification of DNA in vitro: the polymerase chain reaction, *Cold Spring Harbor Symp. Quant. Biol.*, *51 Pt 1*, 263-273.
- [95] C. Papworth, Bauer, J. C., Braman, J. Wright, D. A. (1996). Site-directed mutagenesis in one day with >80% efficiency, *Strategies*, *9*, 3-4.
- [96] W. J. Dower, J. F. Miller, C. W. Ragsdale (1988). High efficiency transformation of *E. coli* by high voltage electroporation, *Nucleic Acids Res.*, *16*, 6127-6145.
- [97] R. D. Gietz, R. A. Woods (2002). Transformation of yeast by lithium acetate/single-stranded carrier DNA/polyethylene glycol method, *Methods Enzymol.*, *350*, 87-96.
- [98] R. S. B. Sikorski, J. D. (1991). In vitro mutagenesis and plasmid shuffling from cloned gene to mutant yeast, *Academic Press Inc.*, San Diego, *194*, 302-318.
- [99] F. Sanger, S. Nicklen, A. R. Coulson (1977). DNA sequencing with chain-terminating inhibitors, *Proc. Natl. Acad. Sci. U S A*, *74*, 5463-5467.
- [100] N. Gallastegui, M. Groll (2012). Analysing properties of proteasome inhibitors using kinetic and X-ray crystallographic studies, *Methods Mol. Biol.*, *832*, 373-390.
- [101] G. Schmidtke, S. Emch, M. Groettrup, H. G. Holzhutter (2000). Evidence for the existence of a non-catalytic modifier site of peptide hydrolysis by the 20 S proteasome, *J. Biol. Chem.*, *275*, 22056-22063.

- [102] U. K. Laemmli (1970). Cleavage of structural proteins during the assembly of the head of bacteriophage T4, *Nature*, *227*, 680-685.
- [103] W. Kabsch (1993). Automatic processing of rotation diffraction data from crystals of initially unknown symmetry and cell constants, *J. Appl. Cryst.*, *26*, 795-800.
- [104] A. J. McCoy, R. W. Grosse-Kunstleve, P. D. Adams, M. D. Winn, L. C. Storoni, R. J. Read (2007). Phaser crystallographic software, *J. Appl. Cryst.*, *40*, 658-674.
- [105] M. Groll, R. Huber (2005). Purification, crystallization, and X-ray analysis of the yeast 20S proteasome, *Methods Enzymol.*, *398*, 329-336.
- [106] A. A. Vagin, R. A. Steiner, A. A. Lebedev, L. Potterton, S. McNicholas, F. Long, G. N. Murshudov (2004). REFMAC5 dictionary: organization of prior chemical knowledge and guidelines for its use, *Acta Crystallogr. Sect. D - Biol. Crystallogr.*, *60*, 2184-2195.
- [107] A. Nicholls, K. A. Sharp, B. Honig (1991). Protein folding and association: insights from the interfacial and thermodynamic properties of hydrocarbons, *Proteins*, *11*, 281-296.
- [108] P. C. Ramos, A. J. Marques, M. K. London, R. J. Dohmen (2004). Role of C-terminal extensions of subunits beta2 and beta7 in assembly and activity of eukaryotic proteasomes, *J. Biol. Chem.*, *279*, 14323-14330.
- [109] a) M. A. Grawert, M. Groll (2012). Exploiting nature's rich source of proteasome inhibitors as starting points in drug development, *Chem. Comm.*, *48*, 1364-1378; b) P. Beck, C. Dubiella, M. Groll (2012). Covalent and non-covalent reversible proteasome inhibition, *Biol. Chem.*, *393*, 1101-1120.
- [110] C. Blackburn, K. M. Gigstad, P. Hales, K. Garcia, M. Jones, F. J. Bruzzese, C. Barrett, J. X. Liu, T. A. Soucy, D. S. Sappal, N. Bump, E. J. Olhava, P. Fleming, L. R. Dick, C. Tsu, M. D. Sintchak, J. L. Blank (2010). Characterization of a new series of non-covalent proteasome inhibitors with exquisite potency and selectivity for the 20S beta5-subunit, *Biochem. J.*, *430*, 461-476.
- [111] H. G. Rammensee, T. Friede, S. Stevanovi (1995). MHC ligands and peptide motifs: first listing, *Immunogenetics*, *41*, 178-228.
- [112] W. Chen, C. C. Norbury, Y. Cho, J. W. Yewdell, J. R. Bennink (2001). Immunoproteasomes shape immunodominance hierarchies of antiviral CD8(+) T cells at the levels of T cell repertoire and presentation of viral antigens, *J. Exp. Med.*, *193*, 1319-1326.
- [113] P. Deol, D. M. Zaiss, J. J. Monaco, A. J. Sijts (2007). Rates of processing determine the immunogenicity of immunoproteasome-generated epitopes, *J. Immunol.*, *178*, 7557-7562.
- [114] R. E. Toes, A. K. Nussbaum, S. Degermann, M. Schirle, N. P. Emmerich, M. Kraft, C. Laplace, A. Zwinderman, T. P. Dick, J. Muller, B. Schonfisch, C. Schmid, H. J. Fehling, S. Stevanovic, H. G. Rammensee, H. Schild (2001). Discrete cleavage motifs of constitutive and immunoproteasomes revealed by quantitative analysis of cleavage products, *J. Exp. Med.*, *194*, 1-12.
- [115] M. Gaczynska, K. L. Rock, T. Spies, A. L. Goldberg (1994). Peptidase activities of proteasomes are differentially regulated by the major histocompatibility complex-encoded genes for LMP2 and LMP7, *Proc. Natl. Acad. Sci. U S A*, *91*, 9213-9217.
- [116] H. J. Fehling, W. Swat, C. Laplace, R. Kuhn, K. Rajewsky, U. Muller, H. von Boehmer (1994). MHC class I expression in mice lacking the proteasome subunit LMP-7, *Science*, *265*, 1234-1237.
- [117] L. Tu, C. Moriya, T. Imai, H. Ishida, K. Tetsutani, X. Duan, S. Murata, K. Tanaka, C. Shimokawa, H. Hisaeda, K. Himeno (2009). Critical role for the immunoproteasome subunit LMP7 in the resistance of mice to *Toxoplasma gondii* infection, *Eur. J. Immunol.*, *39*, 3385-3394.

- [118] a) L. Van Kaer, P. G. Ashton-Rickardt, M. Eichelberger, M. Gaczynska, K. Nagashima, K. L. Rock, A. L. Goldberg, P. C. Doherty, S. Tonegawa (1994). Altered peptidase and viral-specific T cell response in LMP2 mutant mice, *Immunity*, *1*, 533-541; b) M. Basler, J. Moebius, L. Elenich, M. Groettrup, J. J. Monaco (2006). An altered T cell repertoire in MECL-1-deficient mice, *J. Immunol.*, *176*, 6665-6672.
- [119] a) E. J. Corey, W. D. Li (1999). Total synthesis and biological activity of lactacystin, omuralide and analogs, *Chem. Pharm. Bull.*, *47*, 1-10; b) M. Nett, T. A. Gulder, A. J. Kale, C. C. Hughes, B. S. Moore (2009). Function-oriented biosynthesis of beta-lactone proteasome inhibitors in *Salinispora tropica*, *J. Med. Chem.*, *52*, 6163-6167.

## 9 Appendix

<i>Subunit</i>		<i>iCP</i>			<i>cCP</i>			<i>iCP compared to cCP</i>		
<i>1</i>	<i>2</i>	<i>Interface</i> [Å <sup>2</sup> ]	<i>hb</i>	<i>sb</i>	<i>Interface</i> [Å <sup>2</sup> ]	<i>hb</i>	<i>sb</i>	<i>Interface</i> [%]	<i>Δhb</i>	<i>Δsb</i>
α1	α2	1399.9	18	3	1403.3	17	3	99.8	+1	0
α1	α7	1323.6	19	4	1341.2	16	3	98.7	+3	+1
α2	α3	1459.1	16	5	1462.1	18	5	99.8	-2	0
α3	α4	1430.3	20	5	1500.0	18	6	95.4	+2	-1
α4	α5	1395.6	21	4	1423.8	25	9	98.0	-4	-5
α5	α6	1327.8	19	4	1336.7	18	4	99.3	+1	0
α6	α7	1367.0	19	1	1365.4	20	2	100.1	-1	-1
β1(i)	β1(i)′	750.8	8	6	945.7	8	8	79.4	0	-2
β1(i)	β2(i)	471.6	5	7	552.8	8	5	85.3	-3	+2
β1(i)	β7	717.4	11	8	715.7	13	8	100.2	-2	0
β1(i)′	β7	1110.7	16	3	1142.4	19	2	97.2	-3	+1
β2(i)	β3	1531.0	25	12	1601.7	25	11	95.6	0	+1
β2(i)	β7′	694.4	8	11	744.0	7	7	93.3	+1	+4
β3	β4	752.1	12	4	737.6	13	5	102.0	-1	-1
β3	β5(i)′	855.7	19	8	841.6	19	8	101.7	0	0
β4	β4′	734.0	14	0	761.7	11	0	96.4	+3	0
β4	β5(i)	589.4	3	5	590.0	4	4	99.9	-1	+1
β4′	β5(i)	597.0	8	7	654.3	7	10	91.2	+1	-3
β5(i)	β6	688.7	12	4	547.2	10	4	125.9	+2	0
β6	β7	970.8	13	1	974.3	13	3	99.6	0	-2
β6′	β2(i)	1130.6	15	4	1215.8	16	5	93.0	-1	-1
β6′	β3	657.6	8	5	673.8	10	6	97.6	-2	-1
β1(i)	α1	457.4	5	3	417.0	3	0	109.7	+2	+3
β1(i)	α7	457.8	7	3	440.7	2	1	103.9	+5	+2
β2(i)	α1	566.2	8	6	583.5	7	5	97.0	+1	+1
β2(i)	α2	441.8	3	0	463.3	5	0	95.4	-2	0
β3	α2	412.6	8	6	427.7	10	6	96.5	-2	0

**Table 15 PISA analysis<sup>[93]</sup> of interface areas and interactions of adjacent proteasome subunits in the murine cCP and iCP.** The number of hydrogen bonds (hb) and salt bridges (sb) as well as their differences between cCP and iCP ( $\Delta$ ) are provided. Interface areas of iCP subunits are given as percentage of the corresponding values in the cCP.

	<b>yCP</b> <i>yβ5Q53S</i>	<b>yCP</b> <i>yβ5Q53S:bortezomib</i>	<b>yCP</b> <i>yβ5Q53S:ONX 0914</i>
<b>Crystal parameters</b>			
Space group	P2 <sub>1</sub>	P2 <sub>1</sub>	P2 <sub>1</sub>
Cell constants	a=134.7 Å b=301.9 Å c=144.7 Å β=112.9 °	a=136.3 Å b=301.4 Å c=145.2 Å β=113.1 °	a=136.7 Å b=301.5 Å c=145.2 Å β=112.8 °
CPs / AU <sup>a</sup>	1	1	1
<b>Data collection</b>			
Beam line	X06SA, SLS	X06SA, SLS	X06SA, SLS
Wavelength (Å)	1.0	1.0	1.0
Resolution range (Å) <sup>b</sup>	49-2.9 (3.0-2.9)	49-3.0 (3.1-3.0)	49-3.4 (3.5-3.4)
No. observations	717696	653661	521471
No. unique reflections <sup>c</sup>	230488	209442	146379
Completeness (%) <sup>b</sup>	98.2 (98.6)	97.5 (99.1)	98.6 (99.0)
R <sub>merge</sub> (%) <sup>b, d</sup>	7.9 (55.3)	8.4 (62.0)	13.6 (58.7)
I/σ (I) <sup>b</sup>	11.8 (2.6)	13.0 (3.2)	7.6 (2.3)
<b>Refinement (REFMAC5)</b>			
Resolution range (Å)	15-2.9	15-3.0	15-3.4
No. refl. working set	218963	308271	176276
No. refl. test set	10948	15413	8813
No. non hydrogen	50864	51032	51116
No. of ligand atoms	-	168	294
Water molecules	1322	1322	1322
R <sub>work</sub> /R <sub>free</sub> (%) <sup>e</sup>	15.1 / 21.1	14.7 / 20.6	14.2 / 21.7
r.m.s.d. bond (Å) / (°) <sup>f</sup>	0.011 / 1.599	0.012 / 1.637	0.011 / 1.591
Average B-factor (Å <sup>2</sup> )	61.7	64.5	70.7
Ramachandran Plot (%) <sup>g</sup>	94.3 / 4.7 / 1.0	94.4 / 4.9 / 0.7	92.3 / 6.6 / 1.1

**Table 16 X-ray data collection and refinement statistics of structures of the yCP mutant yβ5Q53S.**<sup>a</sup> Asymmetric unit.<sup>b</sup> The values in parentheses of resolution range, completeness, R<sub>merge</sub> and I/σ (I) correspond to the last resolution shell.<sup>c</sup> Friedel pairs were treated as identical reflections.<sup>d</sup>  $R_{\text{merge}}(I) = \frac{\sum_{\text{hkl}} \sum_j |I(\text{hkl})_j - I(\text{hkl})|}{\sum_{\text{hkl}} I_{\text{hkl}}}$ , where  $I(\text{hkl})_j$  is the  $j^{\text{th}}$  measurement of the intensity of reflection hkl and  $\langle I(\text{hkl}) \rangle$  is the average intensity.<sup>e</sup>  $R = \frac{\sum_{\text{hkl}} | |F_{\text{obs}}| - |F_{\text{calc}}| |}{\sum_{\text{hkl}} |F_{\text{obs}}|}$ , where R<sub>free</sub> is calculated for a randomly chosen 5 % of reflections, which were not used for structure refinement, and R<sub>work</sub> is calculated for the remaining reflections.<sup>f</sup> Deviations from ideal bond lengths/angles.<sup>g</sup> Number of residues in favoured, allowed or outlier region.

	<b>yCP</b> yβ5 A27S K32N A46S T57R G48C K71G V127T	<b>yCP</b> yβ5 A27S K32N A46S T57R G48C K71G V127T:bortezomib	<b>yCP</b> yβ5 A27S K32N A46S T57R G48C K71G V127T:ONX 0914
<b>Crystal parameters</b>			
Space group	P2 <sub>1</sub>	P2 <sub>1</sub>	P2 <sub>1</sub>
Cell constants	a=134.5 Å b=301.0 Å c=144.4 Å β=113.0 °	a=136.5 Å b=300.4 Å c=145.6 Å β=113.1 °	a=136.6 Å b=300.3 Å c=145.8 Å β=113.2 °
CPs / AU <sup>a</sup>	1	1	1
<b>Data collection</b>			
Beam line	X06SA, SLS	X06SA, SLS	X06SA, SLS
Wavelength (Å)	1.0	1.0	1.0
Resolution range (Å) <sup>b</sup>	49-2.5 (2.6-2.5)	49-2.8 (2.9-2.8)	49-2.6 (2.7-2.6)
No. observations	1048068	813713	1001216
No. unique reflections <sup>c</sup>	353449	260234	324245
Completeness (%) <sup>b</sup>	97.3 (98.4)	98.5 (99.0)	98.3 (99.4)
R <sub>merge</sub> (%) <sup>b, d</sup>	7.5 (59.7)	7.5 (46.2)	7.6 (56.0)
I/σ (I) <sup>b</sup>	9.2 (2.0)	11.9 (3.4)	10.8 (2.7)
<b>Refinement (REFMAC5)</b>			
Resolution range (Å)	15-2.5	15-2.8	15-2.6
No. refl. working set	335776	247222	308031
No. refl. test set	16788	12361	15401
No. non hydrogen	50888	51047	51135
No. of ligand atoms	-	168	294
Water molecules	1340	1340	1340
R <sub>work</sub> /R <sub>free</sub> (%) <sup>e</sup>	19.0 / 23.6	15.5 / 21.0	16.9 / 21.5
r.m.s.d. bond (Å) / (°) <sup>f</sup>	0.012 / 1.652	0.011 / 1.551	0.012 / 1.649
Average B-factor (Å <sup>2</sup> )	58.1	62.7	62.1
Ramachandran Plot (%) <sup>g</sup>	94.4 / 4.8 / 0.8	95.5 / 3.7 / 0.7	95.6 / 3.8 / 0.6

**Table 17 X-ray data collection and refinement statistics of structures of the yCP mutant yβ5 A27S K32N A46S T57R G48C K71G V127T.**

<sup>a</sup> Asymmetric unit.

<sup>b</sup> The values in parentheses of resolution range, completeness, R<sub>merge</sub> and I/σ (I) correspond to the last resolution shell.

<sup>c</sup> Friedel pairs were treated as identical reflections.

<sup>d</sup>  $R_{\text{merge}}(I) = \frac{\sum_{\text{hkl}} \sum_j |I(\text{hkl})_j - \langle I(\text{hkl}) \rangle|}{\sum_{\text{hkl}} I_{\text{hkl}}}$ , where  $I(\text{hkl})_j$  is the  $j^{\text{th}}$  measurement of the intensity of reflection hkl and  $\langle I(\text{hkl}) \rangle$  is the average intensity.

<sup>e</sup>  $R = \frac{\sum_{\text{hkl}} (|F_{\text{obs}}| - |F_{\text{calc}}|)}{\sum_{\text{hkl}} |F_{\text{obs}}|}$ , where R<sub>free</sub> is calculated for a randomly chosen 5 % of reflections, which were not used for structure refinement, and R<sub>work</sub> is calculated for the remaining reflections.

<sup>f</sup> Deviations from ideal bond lengths/angles.

<sup>g</sup> Number of residues in favoured, allowed or outlier region.

	<i>yCP</i> <i>yβ5 M45R</i>	<i>yCP</i> <i>yβ5 M45R:bortezomib</i>	<i>yCP</i> <i>yβ5 M45R:ONX 0914</i>
<b>Crystal parameters</b>			
Space group	P2 <sub>1</sub>	P2 <sub>1</sub>	P2 <sub>1</sub>
Cell constants	a=134.6 Å b=302.8 Å c=145.2 Å β=112.7 °	a=136.0 Å b=300.3 Å c=145.1 Å β=112.8 °	a=135.9 Å b=298.1 Å c=144.4 Å β=112.7 °
CPs / AU <sup>a</sup>	1	1	1
<b>Data collection</b>			
Beam line	X06SA, SLS	X06SA, SLS	X06SA, SLS
Wavelength (Å)	1.0	1.0	1.0
Resolution range (Å) <sup>b</sup>	49-3.0 (3.1-3.0)	49-2.9 (3.0-2.9)	48-2.8 (2.9-2.8)
No. observations	640110	700484	747601
No. unique reflections <sup>c</sup>	208693	230999	248239
Completeness (%) <sup>b</sup>	97.7 (98.9)	97.7 (98.6)	95.6 (96.1)
R <sub>merge</sub> (%) <sup>b, d</sup>	10.6 (49.4)	8.7 (55.5)	7.4 (50.6)
I/σ (I) <sup>b</sup>	8.7 (2.7)	10.1 (1.7)	11.1 (1.8)
<b>Refinement (REFMAC5)</b>			
Resolution range (Å)	15-3.0	15-2.9	15-2.8
No. refl. working set	198258	219448	235827
No. refl. test set	9912	10972	11791
No. non hydrogen	50894	51053	51137
No. of ligand atoms (ligand; MES)	-	168	318
Water molecules	1340	1340	1340
R <sub>work</sub> /R <sub>free</sub> (%) <sup>e</sup>	14.8 / 20.7	15.9 / 21.7	17.5 / 23.9
r.m.s.d. bond (Å) / (°) <sup>f</sup>	0.014 / 1.802	0.012 / 1.658	0.014 / 1.830
Average B-factor (Å <sup>2</sup> )	59.2	61.0	64.1
Ramachandran Plot (%) <sup>g</sup>	94.2 / 5.1 / 0.8	95.1 / 4.2 / 0.8	93.7 / 5.4 / 0.8

**Table 18 X-ray data collection and refinement statistics of structures of the *yCP* mutant *yβ5 M45R*.**<sup>a</sup> Asymmetric unit.<sup>b</sup> The values in parentheses of resolution range, completeness, R<sub>merge</sub> and I/σ (I) correspond to the last resolution shell.<sup>c</sup> Friedel pairs were treated as identical reflections.<sup>d</sup>  $R_{\text{merge}}(I) = \frac{\sum_{\text{hkl}} \sum_j |I(\text{hkl})_j - I(\text{hkl})|}{\sum_{\text{hkl}} I_{\text{hkl}}}$ , where  $I(\text{hkl})_j$  is the  $j^{\text{th}}$  measurement of the intensity of reflection hkl and  $\langle I(\text{hkl}) \rangle$  is the average intensity.<sup>e</sup>  $R = \frac{\sum_{\text{hkl}} (|F_{\text{obs}}| - |F_{\text{calc}}|)}{\sum_{\text{hkl}} |F_{\text{obs}}|}$ , where R<sub>free</sub> is calculated for a randomly chosen 5 % of reflections, which were not used for structure refinement, and R<sub>work</sub> is calculated for the remaining reflections.<sup>f</sup> Deviations from ideal bond lengths/angles.<sup>g</sup> Number of residues in favoured, allowed or outlier region.

	<b>yCP</b> <i>yβ5 I35T M45R</i>	<b>yCP</b> <i>yβ5 I35T M45R:bortezomib</i>	<b>yCP</b> <i>yβ5 I35T M45R:ONX 0914</i>
<b>Crystal parameters</b>			
Space group	P2 <sub>1</sub>	P2 <sub>1</sub>	P2 <sub>1</sub>
Cell constants	a=133.9 Å b=300.6 Å c=144.2 Å β=112.8 °	a=135.1 Å b=301.0 Å c=146.1 Å β=112.8 °	a=135.5 Å b=299.1 Å c=145.7 Å β=112.9 °
CPs / AU <sup>a</sup>	1	1	1
<b>Data collection</b>			
Beam line	X06SA, SLS	X06SA, SLS	X06SA, SLS
Wavelength (Å)	1.0	1.0	1.0
Resolution range (Å) <sup>b</sup>	49-3.0 (3.1-3.0)	50-2.9 (3.0-2.9)	50-3.1 (3.2-3.1)
No. observations	621044	698969	578722
No. unique reflections <sup>c</sup>	205091	231926	186814
Completeness (%) <sup>b</sup>	97.9 (98.3)	97.7 (99.1)	96.8 (98.7)
R <sub>merge</sub> (%) <sup>b, d</sup>	11.9 (52.2)	9.6 (50.3)	9.8 (46.8)
I/σ (I) <sup>b</sup>	8.6 (2.9)	8.6 (2.6)	9.8 (2.5)
<b>Refinement (REFMAC5)</b>			
Resolution range (Å)	15-3.0	15-2.9	15-3.1
No. refl. working set	194836	220329	177472
No. refl. test set	9741	11016	8873
No. non hydrogen	50891	51051	51161
No. of ligand atoms (ligand; MES)	-	168	318
Water molecules	1340	1340	1340
R <sub>work</sub> /R <sub>free</sub> (%) <sup>e</sup>	15.6 / 22.4	15.6 / 21.8	14.3 / 21.1
r.m.s.d. bond (Å) / (°) <sup>f</sup>	0.011 / 1.592	0.012 / 1.664	0.012 / 1.754
Average B-factor (Å <sup>2</sup> )	55.7	62.8	61.3
Ramachandran Plot (%) <sup>g</sup>	94.7 / 4.4 / 0.9	94.5 / 4.6 / 0.9	93.7 / 5.3 / 1.0

**Table 19 X-ray data collection and refinement statistics of structures of the yCP mutant yβ5 I35T M45R.**<sup>a</sup> Asymmetric unit.<sup>b</sup> The values in parentheses of resolution range, completeness, R<sub>merge</sub> and I/σ (I) correspond to the last resolution shell.<sup>c</sup> Friedel pairs were treated as identical reflections.<sup>d</sup>  $R_{\text{merge}}(I) = \frac{\sum_{\text{hkl}} \sum_j | [I(\text{hkl})_j - I(\text{hkl})] |}{\sum_{\text{hkl}} I_{\text{hkl}}}$ , where  $I(\text{hkl})_j$  is the  $j^{\text{th}}$  measurement of the intensity of reflection hkl and  $\langle I(\text{hkl}) \rangle$  is the average intensity.<sup>e</sup>  $R = \frac{\sum_{\text{hkl}} | |F_{\text{obs}}| - |F_{\text{calc}}| |}{\sum_{\text{hkl}} |F_{\text{obs}}|}$ , where R<sub>free</sub> is calculated for a randomly chosen 5 % of reflections, which were not used for structure refinement, and R<sub>work</sub> is calculated for the remaining reflections.<sup>f</sup> Deviations from ideal bond lengths/angles.<sup>g</sup> Number of residues in favoured, allowed or outlier region.

	<b>yCP</b> <i>yβ5 A20S, A22C, V31S, M45T, A46S, G48T</i>	<b>yCP</b> <i>yβ5 A20S, A22C, V31S, M45T, A46S, G48T:ONX 0914</i>
<b>Crystal parameters</b>		
Space group	P2 <sub>1</sub>	P2 <sub>1</sub>
Cell constants	a=135.0 Å b=302.5 Å c=144.2 Å β=112.8 °	a=136.6 Å b=299.9 Å c=146.1 Å β=113.2 °
CPs / AU <sup>a</sup>	1	1
<b>Data collection</b>		
Beam line	X06SA, SLS	X06SA, SLS
Wavelength (Å)	1.0	1.0
Resolution range (Å) <sup>b</sup>	25-2.9 (3.0-2.9)	25-3.1 (3.2-3.1)
No. observations	724106	558889
No. unique reflections <sup>c</sup>	230082	185554
Completeness (%) <sup>b</sup>	99.4 (97.9)	95.0 (97.4)
R <sub>merge</sub> (%) <sup>b, d</sup>	11.9 (53.3)	14.3 (54.0)
I/σ (I) <sup>b</sup>	7.5 (2.1)	6.3 (2.2)
<b>Refinement (REFMAC5)</b>		
Resolution range (Å)	15-2.9	15-3.1
No. refl. working set	218577	176276
No. refl. test set	10928	8813
No. non hydrogen	50876	51129
No. of ligand atoms	0	294
Water molecules	1322	1322
R <sub>work</sub> /R <sub>free</sub> (%) <sup>e</sup>	15.4 / 21.2	14.7 / 21.7
r.m.s.d. bond (Å) / (°) <sup>f</sup>	0.011 / 1.589	0.012 / 1.681
Average B-factor (Å <sup>2</sup> )	54.9	66.5
Ramachandran Plot (%) <sup>g</sup>	95.7 / 3.7 / 0.6	92.9 / 6.0 / 1.1

**Table 20 X-ray data collection and refinement statistics of structures of the β5t-mimicking yCP mutant.**<sup>a</sup> Asymmetric unit.<sup>b</sup> The values in parentheses of resolution range, completeness, R<sub>merge</sub> and I/σ (I) correspond to the last resolution shell.<sup>c</sup> Friedel pairs were treated as identical reflections.<sup>d</sup>  $R_{\text{merge}}(I) = \frac{\sum_{\text{hkl}} \sum_j |I(\text{hkl})_j - \langle I(\text{hkl}) \rangle|}{\sum_{\text{hkl}} I_{\text{hkl}}}$ , where  $I(\text{hkl})_j$  is the  $j^{\text{th}}$  measurement of the intensity of reflection hkl and  $\langle I(\text{hkl}) \rangle$  is the average intensity.<sup>e</sup>  $R = \frac{\sum_{\text{hkl}} | |F_{\text{obs}}| - |F_{\text{calc}}| |}{\sum_{\text{hkl}} |F_{\text{obs}}|}$ , where R<sub>free</sub> is calculated for a randomly chosen 5 % of reflections, which were not used for structure refinement, and R<sub>work</sub> is calculated for the remaining reflections.<sup>f</sup> Deviations from ideal bond lengths/angles.<sup>g</sup> Number of residues in favoured, allowed or outlier region.

## 10 Abbreviations

Å	Ångström
aa	amino acid
Ac	acetate/acetyl
AMC	7-Amino-4-methylcoumarin
AMP	adenosine monophosphate
Amp	ampicillin
APS	ammonium persulfate
ATP	adenosine triphosphate
<i>B. taurus</i>	<i>Bos taurus</i>
bp	base pairs
Braap	branched chain amino acid preferring
BSA	bovine serum albumin
°C	degree Celsius
Cbz	Carboxybenzyl
cCP	20S constitutive proteasome
CD8	cluster of differentiation 8
ChTL	Chymotrypsin-like
CL	Caspase-like
CM	complete medium
CP	core particle, 20S proteasome
cTEC	cortical thymic epithelial cells
CTL	cytotoxic T lymphocyte
2D	two-dimensional
3D	three-dimensional
Da	dalton
ddH <sub>2</sub> O	double distilled water
DMSO	dimethylsulfoxid
DNA	deoxyribonucleic acid
dNTP	deoxyribonucleotide triphosphate
DTT	dithiothreitol
<i>E. coli</i>	<i>Escherichia coli</i>

---

EDTA	ethylenediaminetetraacetic acid
ER	endoplasmic reticulum
EtOH	ethanol
FDA	U. S. food and drug administration
5-FOA	5-fluoroorotic acid
HCl	hydrochloric acid
Hsp	heat shock protein
IC <sub>50</sub>	half maximal inhibitory concentration
iCP	20S immunoproteasome
IFN	interferon
IL	interleukin
K	Kelvin
kbp	kilo base pairs
kDa	kilo Dalton
LB	Luria Bertani
LCMV-WE	lymphocytic choriomeningitis virus strain WE
LiAc	lithium acetate
mA	milliampere
MDa	mega Dalton
MES	2-( <i>N</i> -morpholino) ethanesulfonic acid
MHC	major histocompatibility complex class
MPD	2-Methyl-2,4-Pentenediol
NCS	non-crystallographic symmetry
NEPHGE	non-equilibrium pH gradient gel electrophoresis
NF-κB	nuclear factor-κB
Ntn	N-terminal nucleophile
OD	optical density
PAGE	polyacrylamide gel electrophoresis
PCR	polymerase chain reaction
PDB	Protein Data Bank
PEG	polyethylene glycol
pNA	para-nitroaniline
R <sub>free</sub>	free R-factor
r.m.s.d.	root-mean-square deviation

## Abbreviations

---

rpm	rounds per minute
R <sub>work</sub>	crystallographic R-factor
S	Svedberg
<i>S. cerevisiae</i>	<i>Saccharomyces cerevisiae</i>
SDS	sodiumdodecylsulfate
SLS	Swiss Light Source
Snaap	small neutral amino acid preferring
SOC	super optimal broth with catabolite repression
Suc	Succinyl
<i>T. acidophilum</i>	<i>Thermoplasma acidophilum</i>
TAE	Tris-Acetate-EDTA
TAP	transporter associated with antigen processing
tCP	20S thymoproteasome
TCR	T cell receptor
TE	Tris-EDTA
TEMED	<i>N,N,N',N'</i> -tetramethylethylenediamine
TL	trypsin-like
TLS	Translation, Libration, Screw
T <sub>m</sub>	melting temperature
TNF	tumour necrosis factor
Tris	Tris (hydroxymethyl-) aminomethane
Tris-HCl	Tris (hydroxymethyl-) aminomethane hydrochloride
U	unit
UV	ultraviolet
V	volt
VIS	visible
v/v	volume per volume
wt	wildtype
w/v	weight per volume
yCP	yeast 20S proteasome
YPD	yeast extract peptone dextrose

## 11 Publications

The present thesis has been conducted from September 2009 till January 2013 under the supervision of Prof. Dr. Michael Groll, Chair of Biochemistry, TUM.

Parts of this thesis have been published:

Immuno- and constitutive proteasome crystal structures reveal differences in substrate and inhibitor specificity

Huber, E. M.\*, Basler, M.\*, Schwab, R.\*, Heinemeyer, W., Kirk, C. J., Groettrup, M., Groll, M. (2012), *Cell*, *148*, 727-738.

The 19S cap puzzle: A new jigsaw piece

Huber, E. M. and Groll, M. (2012). *Structure*, *20*, 387-388.

Kristallstruktur eines molekularen Schredders

Huber, E. M. and Groll, M. (2012). *GIT Labor-Fachzeitschrift*, *5*, 363-365.

Inhibitors for the immuno- and constitutive proteasome: current and future trends in drug development.

Huber, E. M. and Groll, M. (2012). *Angew. Chem. Int. Ed. Engl.*, *51*, 8708-8720.

\*These authors contributed equally

## 12 Acknowledgement

First of all I would like to thank my supervisor Prof. Dr. Michael Groll for providing me the possibility to work in his excellent team and for entrusting me the immunoproteasome project. I am very grateful for his daily interest in my work, his deep confidence in me, his continuous support and substantial promotion. His enormous enthusiasm and encouragement as well as his advices and ideas were of great help not only for my scientific results but, even more important, also for my personality.

Special thanks go to my collaborators from the University of Constance Prof. Dr. Marcus Groettrup, Dr. Michael Basler and Ricarda Schwab. Without their contribution - the purification of the murine proteasomes - this work would not have been possible.

I strongly thank PD Dr. Wolfgang Heinemeyer for sharing his outstanding knowledge and experience in yeast genetics with me, for helping me creating the numerous mutants and for all the new techniques he taught me.

I am very grateful to Dr. Melissa Gräwert who patiently introduced me to the theory and the praxis of crystallography during the first year of my PhD.

Moreover, I want to acknowledge Richard Feicht for all the yeast proteasome purifications and the amazing crystals he produced.

I am also indebted to all the students that joined me in the lab. In particular I thank Silvia Domcke for her excellent work.

Last but not least, I want to thank all members of the Groll group, especially my PhD colleagues for the nice and relaxed working atmosphere, one of the things I appreciated and enjoyed most during the last three years. I am grateful for all the funny moments inside and outside the lab, especially during the synchrotron trips and for all the group activities, we did together. Especially, I thank Ute and Astrid for managing many of my problems with forms and orders.

Finally, I thank my family for having enabled my studies, for their support, their confidence in me and their interest in my work.

I, Eva Maria Huber, hereby declare that I independently prepared the present thesis, using only the references and resources stated. This work has not been submitted to any examination board yet. Parts of this work have been or will be published in scientific journals.

Garching, February 2013